

**Small Cell Carcinoma of the Ovary, Hypercalcemic Type:  
Model Development and Preclinical Drug Testing**

by

Yuting (Shary) Chen

Honors B.Sc., The University of British Columbia, 2016

A THESIS SUBMITTED IN PARTIAL FULFILLMENT OF  
THE REQUIREMENTS FOR THE DEGREE OF

MASTER OF SCIENCE

in

The Faculty of Graduate and Postdoctoral Studies  
(Pathology and Laboratory Medicine)

THE UNIVERSITY OF BRITISH COLUMBIA  
(Vancouver)

October 2018

© Yuting (Shary) Chen, 2018

The following individuals certify that they have read, and recommend to the Faculty of Graduate and Postdoctoral Studies for acceptance, a thesis/dissertation entitled:

Small Cell Carcinoma of the Ovary, Hypercalcemic Type: Model Development and Preclinical Drug Testing

submitted by Yuting (Shary) Chen in partial fulfillment of the requirements for the degree of Master of Science in Pathology and Laboratory Medicine

**Examining Committee:**

David Huntsman, Pathology and Laboratory Medicine

Supervisor

Christian Steidl, Pathology and Laboratory Medicine

Supervisory Committee Member

Yu Zhuo Wang, Pathology and Laboratory Medicine

Supervisory Committee Member

David Schaeffer, Pathology and Laboratory Medicine

Additional Examiner

Amina Zoubeidi, Urologic Sciences

Additional Examiner

**Additional Supervisory Committee Members:**

Marcel Bally, Pathology and Laboratory Medicine

Supervisory Committee Member

Yemin Wang, Pathology and Laboratory Medicine

Supervisory Committee Member

## **Abstract**

Small cell carcinoma of the ovary, hypercalcemic type (SCCOHT) is a rare and aggressive ovarian cancer that usually occurs in women in their 20s. As SCCOHT has a very low survival rate, an effective therapeutic solution is urgently needed. Genomic studies have demonstrated that concurrent dual loss of SMARCA4/A2, the two only ATPase of the SWI/SNF chromatin-remodeling complex, occurs in more than 90% SCCOHT cases, which opens the opportunity for developing targeted therapeutics for treating SCCOHT.

One major challenge for preclinical studies is the discrepancy between preclinical and clinical outcomes. Although preclinical anti-cancer drugs are mostly tested in subcutaneous xenograft models, they do not provide a relevant environmental support for most cancer types. In contrast, orthotopical models potentially provides similar microenvironment for tumor development. However, the tumor growth monitoring is challenging for orthotopical tumours. To overcome these challenges, I developed SCCOHT cell lines stably expressing mKate2, a far-red fluorescent protein. The application of these SCCOHT cell lines in both subcutaneous and intrabursal models indicated that the fluorescent signals directly correlated to the tumor progression. Pathological analysis revealed intrabursal tumor contained histological features typical of SCCOHT, such as follicle-like structures. Metastasis and ascites were also observed in the intrabursal model. Thus, intrabursal model of SCCOHT mimics the microenvironment of SCCOHT tumors

developed in patients; introducing a fluorescent signal provides a convenient monitoring method of the tumor development.

Previous studies have shown an antagonism between the SWI/SNF complex components and the polycomb repressive complex 2 (PRC2) in regulating various gene expression. As dual loss of SMARCA4 and SMARCA2 is a definitive feature of SCCOHT, we hypothesize that pharmaceutical inhibition of the activity of PRC2 in SCCOHT may be a potential therapeutic approach. Accordingly, depletion of EZH2, the catalytic subunit of PRC2, or pharmacological inhibition of PRC2 by either GSK126 or EED226 suppressed the proliferation of SCCOHT cell lines. Furthermore, administration of 200 mg/kg EED226 twice daily significantly decreased tumor progression in mice bearing the fluorescent SCCOHT1 subcutaneous xenograft. Therefore, targeting PRC2 is a potential therapeutic strategy for treating SCCOHT and fluorescent imaging can be used to monitor tumor growth in preclinical studies.

## Lay Summary

SCCOHT is a very deadly ovarian cancer subtype that affects women in their 20s. A better treatment for this disease is urgently needed. To anticipate the outcome in clinical trials, scientists use animal studies to test potential treatments. I established cancer cells with fluorescent signals that could glow inside ovary. To validate this model system, I implanted these cells in the mice to test the effectiveness of a new potential drug, EED226, for SCCOHT. After two weeks of treatment, EED226 slowed down the tumor growth, and the fluorescence signals from these cells localized the outline of tumors. These findings suggest EED226 could be a potential treatment for SCCOHT, and these fluorescent cells can be a useful tool to track tumor cells inside mice during preclinical studies.

## **Preface**

The aims and experimental of this study were developed with guidance and mentorship from Dr. Yemin Wang and Dr. David Huntsman. All *in vitro* experiments in this study were primarily conducted by me, with the help of Chae Young Shin. I performed all the *in vivo* experiments with supervision from Nicole Wretham. Subsequent experiments, including tissue processing, sectioning and staining was completed by Sylvia Lee from CTAG and Angela Cheng from GPEC. All pathology analysis was completed with assistance from Dr. Basile Tessier-Cloutier.

Part of Chapter 4 is based on a research paper published in the Journal of Pathology. Wang Y, Chen Y, Karnezis A, Colborne S, Santos N, Lang J, Hendricks W, Orlando K, Yap D, Kommos F, Bally M, Morin G, Trent J, Weissman B, Huntsman D. (2017) The histone methyltransferase EZH2 is a therapeutic target in small cell carcinoma of the ovary, hypercalcaemic type. *J. Pathol.* 242 (3): 371-383. I performed experiments and analyzed data.

The animal studies were approved by the University of British Columbia Animal Care Committee (A14-0290).

# Table of Contents

<b>Abstract</b> .....	<b>iii</b>
<b>Lay Summary</b> .....	<b>v</b>
<b>Preface</b> .....	<b>vi</b>
<b>Table of Contents</b> .....	<b>vii</b>
<b>List of Tables</b> .....	<b>xi</b>
<b>List of Figures</b> .....	<b>xii</b>
<b>List of Abbreviations</b> .....	<b>xiv</b>
<b>Acknowledgements</b> .....	<b>xvi</b>
<b>Chapter 1: Introduction</b> .....	<b>1</b>
1.1 Ovarian Cancer .....	1
1.1.1 Etiology and Epidemiology of Ovarian Cancer .....	1
1.1.2 Diagnosis and Treatment of Ovarian Cancer .....	4
1.2 Small Cell Carcinoma of the Ovary, Hypercalcemic Type .....	5
1.2.1 Histology and Pathology.....	7
1.2.2 Genetics .....	7
1.2.3 Cell of Origin and Pathogenesis.....	8
1.2.4 Treatment and Prognosis .....	9
1.3 SWI/SNF complex .....	11
1.3.1 Structure and function of SWI/SNF complex .....	11
1.3.2 SWI/SNF in cancer .....	12
1.4 Polycomb Repressive Complex .....	14

1.4.1	Structure and Role of PRC.....	14
1.4.2	SWI/SNF - PRC2 antagonism.....	18
1.5	Animal models for studying ovarian cancer and efficacy of anti-tumor therapeutics .....	20
1.5.1	Mouse models.....	20
1.5.2	Available xenograft models (subcutaneous, intra bursal, peritoneal) ....	23
1.5.3	Bioimaging System .....	24
1.5.4	mKate2 for imaging <i>in vitro/ in vivo</i> .....	25
<b>Chapter 2: Methods .....</b>		<b>28</b>
2.1	Cell culture, resistant cell lines.....	28
2.2	Construction of mKate2-Expressing SCC $\delta$ OHT cell lines.....	29
2.3	Drug Preparation .....	29
2.4	Drug survival assay .....	30
2.5	Western Blot Analysis .....	30
2.6	<i>In vivo</i> xenograft tumor model.....	31
2.7	Fluorescence Imaging and data processing.....	32
2.8	<i>In vivo</i> toxicity test and efficacy studies .....	33
2.9	Statistical analysis .....	34
<b>Chapter 3: Development of fluorescence-labelled SCCOHT xenograft models</b> .....		<b>35</b>
3.1	Background.....	35
3.2	Results .....	37

3.2.1	Isolation of SCCOHT cell lines stably expressing the mKate2 fluorescent protein.....	37
3.2.2	mKate2-labelled SCCOHT cells mimic their parental cells biologically <i>in vitro</i> .....	41
3.2.3	Subcutaneous xenograft models of mKate2-labelled SCCOHT cells in NRG mice .....	43
3.2.4	SCCOHT intrabursal xenograft model in NRG mice .....	47
3.2.5	Tissue attenuation in intrabursal model .....	53
3.2.6	Histological analysis between subcutaneous and intrabursal COV434-mKate2 xenograft model .....	55
3.3	Discussion .....	61
<b>Chapter 4: Pharmaceutical inhibition of PRC2 complex in SCCOHT .....</b>		<b>66</b>
4.1	Rationale and Specific Aims .....	66
4.2	Result.....	68
4.2.1	SCCOHT cells are sensitive to depletion of EZH2 .....	68
4.2.2	SCCOHT cells are sensitive to inhibition of PRC2 catalytic activity .....	70
4.2.2.1	SCCOHT cells are sensitive to pharmaceutical inhibition of EZH2. ....	70
4.2.2.2	SCCOHT cells are sensitive to pharmaceutical inhibition of EED subunit .....	72
4.2.2.3	Sensitivity of GSK126-resistant cells to EED226 .....	77
4.2.3	<i>In vivo</i> efficacy of EED226 on SCCOHT xenograft tumors .....	79
4.2.3.1	40mg/kg EED226 (PO BID) had minimal toxicity effect in tumor-free NRG mice	79

4.2.3.2	80 mg/kg EED226 (PO BID) had minimal toxicity effect and very mild anti-tumor effect in COV434-mKate2 subcutaneous xenograft model.....	80
4.2.3.3	200 mg/kg EED226 inhibited SCCOHT1-mKate2 xenograft tumor growth .....	82
4.3	Discussion .....	84
<b>Chapter 5: Conclusion and Future Directions .....</b>		<b>89</b>
5.1	Summary of Research.....	89
5.2	Limitation and Future Directions .....	90
<b>Bibliography .....</b>		<b>94</b>

## List of Tables

Table 1.1 Frequent mutations and possible cell of origin in different ovarian cancer subtypes. ....	3
Table 1.2 Summary of frequent mutations in SWI/SNF subunits. ....	13
Table 1.3 The list of PRC2 inhibitors and their clinical development status. ....	17
Table 1.4 Comparison of mouse strain. ....	22
Table 3.1 Summary of clinical and histological observation among different models. ....	65

## List of Figures

Figure 1.1 Incidence of death in Canada. ....	1
Figure 1.2 Antagonism between SWI/SNF and PRC complex. ....	19
Figure 3.1 Transfection of mKate2 into SCCOHT cells. ....	39
Figure 3.2 Isolation of SCCOHT clones with stable mKate2 expression. ....	40
Figure 3.3 Characterization of isolated clones. ....	42
Figure 3.4 SCCOHT subcutaneous model development. ....	46
Figure 3.5 COV434-mKate2 intrabursal xenograft model development. ....	48
Figure 3.6 SCCOHT1-mKate2 intrabursal xenograft model development. ....	50
Figure 3.7 BIN67-mKate2 intrabursal xenograft model development. ....	52
Figure 3.8 Tissue attenuation in the fluorescence model. ....	54
Figure 3.9 Histological analysis in the COV434-mKate2 xenograft model. ....	56
Figure 3.10 Histological analysis in the SCCOHT1-mKate2 xenograft model. ....	58
Figure 3.11 Histological analysis in the BIN67-mKate2 xenograft model. ....	60
Figure 4.1 SCCOHT cells are sensitive to EZH2 depletion. ....	69
Figure 4.2 SCCOHT cells are sensitive to pharmaceutical inhibition of EZH2. ....	71
Figure 4.3 SCCOHT cells are sensitive to EED inhibition. ....	76
Figure 4.4 Sensitivity of GSK126- resistant cells to EED226. ....	78
Figure 4.5 EED226 had mild effect in tumor-free NRG mice. ....	79
Figure 4.6 EED226 had mild effect in the COV434-mKate2 subcutaneous xenograft model. ....	81

Figure 4.7 EED226 had some effect in SCCOHT1-mKate2 subcutaneous xenograft model..... 83

## List of Abbreviations

BAF: BRG1-associated factor

BLI: bioluminescence imaging

CCC: clear cell carcinoma

CE: cisplatin/carboplatin in combination with etoposide

EC: endometrioid carcinoma

EED: embryonic ectoderm development

EZH2: zeste homologue 2

FIGO: International Federation of Gynecology and Obstetrics

FLI: fluorescence imaging

FPS: fluorescent proteins

FRFP: far-red fluorescent protein

GFP: green fluorescent protein

H2AK119ub1: monoubiquitylation of histone H2A on Lys 119

H3K27me3: histone trimethylation at lysine 27

HGSC: high-grade serous carcinoma

IB: intrabursal

IHC: immunohistochemistry

IP: intraperitoneal

LGSC: low-grade serous carcinoma

MC: mucinous carcinoma

mESCs: mouse embryonic stem cells

MRI: magnetic resonance imaging

MRT: malignant rhabdoid tumor

NHL: non-Hodgkin's lymphomas

OC: ovarian cancer

PAVEP: cisplatin, adriamycin, vepeside, cyclophosphamide

PBAF: polybromo BRG1-associated factor

PcGs: polycomb group proteins

PET: positron emission tomography

PRC1: Polycomb repressive complex 1 PRC1

PRC2: polycomb repressive complex 2

RFPs: far-red fluorescent proteins

SAM: S-adenosylmethionine

SC: subcutaneous

SCCOHT: small cell carcinoma of the ovary, hypercalcemic type

SUZ12: suppressor of zeste

SWI/SNF: mating-type switching and sucrose fermentation

VPCBAE: vinblastine cisplatin, cyclophosphamide, bleomycin, doxorubicin,

etoposide

## **Acknowledgements**

First and foremost, I would like to express my sincerest gratitude to my supervisor, Dr. David Huntsman for his patience, guidance, and giving me opportunity to work as a co-op and master student in the lab. I am very grateful to embrace my interest in ovarian cancer research, especially with a very enthusiastic, and vibrant supervisor. Dr. Huntsman is always very supportive for my future career decision and grant me opportunities to learn many different skills during my studies to prepare me better for my future career.

Secondly, I would also like to thank my supervisory committee (Dr. Christian Steidl, Dr. Marcel Bally, and Dr. Yuzhuo Wang) for their constructive and insightful feedbacks.

I owe particular thanks to Dr. Yemin Wang, whom I have worked with very closely during my studies. His day-to-day supervision, coherent answers to my endless questions and forgivingness shape my works as it stands today.

To members of the Huntsman lab, thank you for all the supports and making memories in the lab some of the most enjoyable ones. In particular I would like to thank Chae Young Shin for the assistance in various experiments.

I'd like to thank the Department of Pathology and Laboratory Medicine, including the Program Director Dr. Haydn Pritchard and Heather Cheadle, for their care and assistance.

Lastly, I would like to thank my family and friends for their continued love and support, with particular mention to Ivan Qin and Dotsie Qin who have always been there for me day and night.

# Chapter 1: Introduction

## 1.1 Ovarian Cancer

### 1.1.1 Etiology and Epidemiology of Ovarian Cancer

Malignant neoplasms, commonly known as cancer, have been the leading cause of death in Canada for the past decade, responsible for 38% of all Canadian death in 2015 (Figure 1.1) (1). Almost one in two Canadians will develop cancer in their lifetime, and one-quarter of them will die from the disease (1). Ovarian cancer (OC) is listed as the 8th frequent cancer type in female in 2017, but represents the most lethal gynecologic malignancy. Even though the mortality rate of ovarian cancer has been dropped by 2% each year from 2004 to 2012, the prognosis is still poor, with five-year survival rate of 45.0%, comparing with 64.2% of the survival from all cancers in women, and 87.5% in breast cancer, which is the leading cancer in female. (1)

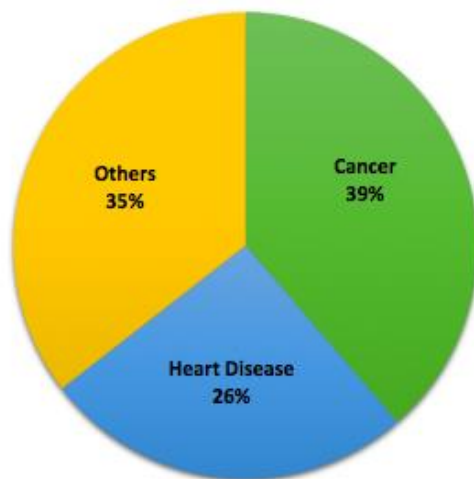


Figure 1.1 Incidence of death in Canada.

Ovarian cancer can be subdivided into different subtypes based on its distinct histology presentation, including high-grade serous carcinoma (HGSC), low-grade serous carcinoma (LGSC), mucinous carcinoma (MC), endometrioid carcinoma (EC), clear cell carcinoma (CCC), and others. These histotypes are often associated with unique spectrum of mutations (Table 1.1) (2). Of note, the most common subtypes are believed to have a non-ovarian origin, even though they are categorized as ovarian cancer. For example, HGSCs are believed to arise from fallopian tube secretory epithelial cells or progenitor cells, whereas EC and CCC are associated with endometriosis and are believed to arise from endometrial epithelial cells (Table 1.1) (3). Development of primary ovarian carcinomas from non-ovarian cell of origin implies that ovary can provide a fertile and enriched environment for cancer precursors and cancer cells to grow.

**Table 1.1 Frequent mutations and possible cell of origin in different ovarian cancer subtypes.**

<b>Subtype</b>	<b>Portion of ovarian cancer</b>	<b>Frequent mutations (2)</b>	<b>Possible cell of origins (3)</b>
<b>HGSC</b>	70%	TP53, BRCA1and BRCA2	Fallopian tube secretory epithelial cell or progenitor cell
<b>LGSC</b>	<5%	KRAS, NRAS, or BRAF	Fallopian tube secretory epithelial cell or progenitor cell
<b>MC</b>	3%	KRAS, TP53 and ERBB2	Unknown
<b>EC</b>	10%	CTNNB1, PIK3CA, KRAS, ARID1A, PTEN, and PPP2R1A	Endometrial epithelial cell
<b>CCC</b>	10%	ARID1A and PIK3CA	Endometrial epithelial cell

### 1.1.2 Diagnosis and Treatment of Ovarian Cancer

Some of the common symptoms of OC include abnormal bloating and nausea, changes in appetite, feeling pressure in the pelvis or lower back, and swelling and pain in the abdomen (4). As most of these symptoms are not specific to OC and are quite common in women these are not particularly useful, and diagnosis of OC usually occurs after its progression to an advanced stage.

During diagnosis, pathologists use FIGO (International Federation of Gynecology and Obstetrics) system to define the stage of disease and provide guidance for treatment. Stage I OC has tumor limited to the ovaries without spread to other sites, such as the abdomen or pelvis. Stage II suggests OC is spread to the pelvic regions, such as fallopian tubes or uterus. If OC spread beyond the pelvis to abdomen or lymph nodes, it is considered as Stage III. When metastasis of OC to other organs such as colon, liver and spleen, it is considered as Stage IV. (5)

Treatment options are based on the stage of the disease and subtype of cancers. The current standard therapy is debulking surgery, following by adjuvant chemotherapy. During surgery, visible tumors are removed, and these tumor samples are used for histologic assessment of histotype and stage. The current chemotherapy regimen includes a taxane (eg. paclitaxel, docetaxel) in combination with a platinum compound (eg. cisplatin, carboplatin).

The discovery of paclitaxel, a compound extracted from Pacific yew tree, changed the regimen of chemotherapy greatly. Paclitaxel binds to tubulin to form stable microtubules, which blocks the completion of mitosis and cell division, and induces cell

death. In combination with cisplatin, paclitaxel significantly increased the complete response rate and overall survival rate in 1990s (6). Cisplatin became part of the standard therapy in the early 1980s. Cisplatin cross-links with purine bases on DNA, interfere with DNA repair and induces apoptosis. Despite the side effects of cisplatin, it was clinically proven to combat various cancer types, including lung cancer, bladder cancer, and ovarian cancer (7-9). Modification of cisplatin, carboplatin, alleviates some of the side effects caused by cisplatin, particularly the nephrotoxic effect. In addition, carboplatin is found to be more stable in the body, with a half-life of 30 hours comparing with 1.5-3.6 hours for cisplatin (10).

Nowadays, the current standard chemotherapy in ovarian cancer is intravenous administration of paclitaxel and carboplatin (TC). However, most of the patients enrolled in the clinical trial for TC were high-grade serous carcinoma, and the number for other types of ovarian cancers were very limited. HGSC is one of the solid tumors that is highly sensitive to chemotherapy. Other ovarian subtypes often do not respond as well as the high-grade serous patients. Thereby, other strategies for choosing treatment regimen, such as by histological subtypes, have been raised (11, 12). Patients with different histological subtypes or mutation can now enroll in clinical trials for targeted molecular therapy and immunotherapy (13-15).

## **1.2 Small Cell Carcinoma of the Ovary, Hypercalcemic Type**

SCCOHT (Small Cell Carcinoma of the Ovary, Hypercalcemic Type) was first described by Dr. Scully (16) in 1979, and was categorized as a distinctive

undifferentiated tumor by Dickerisin *et al* (17) after seeing eleven cases with unilateral large tumor with small tumor cells.

SCCOHT is a very rare and aggressive ovarian cancer, and mostly affects young women with an average age of 23.9 years old, ranging from 14 month- to 71 year-old (18, 19). Clinical symptoms for patients are very similar to other ovarian cancer subtypes, includes vomiting, nausea, discomfort or pain in the abdomen, and irregular menstrual cycle (20). Abdominal pain is the most frequent symptom followed by palpable mass and enlarged waist circumference (18). Serum calcium level is elevated in over 60% of the preoperative-measured cases (21), but very few patients (approximately 5%) develop symptoms, such as polydipsia, lethargy and fatigue, associated with it (21). The mechanism of hypercalcemia is unknown, but it is believed to be associated with tumoral secretion of parathyroid hormone (PTH)-related proteins (22). When hypercalcemia present prior to treatment, researchers uses it as one of the indicators to assess treatment efficacy. Calcium level are normalized upon favorable treatment. In some cases where calcium level was within normal range at diagnosis, hypercalcemia was observed after several cycles of chemotherapy (21, 23) or during recurrence after surgical debulking and chemotherapy (24). Other OC biomarkers such as cancer antigen 125 (CA125) or carbohydrate antigen 19-9 (CA19-9) are elevated in some cases but not all. No correlation is observed between tumor volume or tumor progression and the biomarkers or tumor progression with hypercalcemia (18). Common metastatic sites include liver, lymph nodes, peritoneum and pelvic (25).

### 1.2.1 Histology and Pathology

Despite the aggressive nature of disease, upon laparotomy, tumors are unilateral, usually present in the right ovary, regardless of the stages of disease (21). SCCOHT tumor mass are usually range from 7 to 30 cm in the largest diameter (17, 21, 25) in comparison to 3 cm in diameter of the normal ovary (26). Most tumors are encapsulated, and it appears as solid gray-tan with several cysts (25). The cross-section of the tumor is gray or yellow tan, with multiple hemorrhage and necrosis.

Pathologically, SCCOHT is identified by sheets of diffuse small rounded cells with variable numbers of large cells (21). Some of the tumors present loose growth pattern and most tumor cells have scanty eosinophilic cytoplasm with hyperchromatic nuclei. The mitotic index in SCCOHT is very high. In general, SCCOHT is a densely cellular and poorly differentiated malignant neoplasm. Follicle-like structures are also presented in 80% of the clinical cases (23).

### 1.2.2 Genetics

In 2013, a research team from Poland reported SMARCA4 loss in 2 cases of SCCOHT (27). Shortly after, three groups, including Huntsman lab showed the monogenic nature of SCCOHT, mutations in *SMARCA4* gene (28-30). They independently performed whole-genome or whole-exome sequencing on their SCCOHT cohort and found 91% (83/91) of the total cases studied harbored germline or somatic mutation in *SMARCA4* (28-30). Our group has showed expression of BRG1 (*SMARCA4*) was lost in 82% of our SCCOHT cohort (30). As *SMARCA4* and *SMARCA2* (*BRG1* and *BRM*) are the two mutually exclusive ATPase of SWI/SNF

chromatin remodelling complex, our lab further determined the status of BRM (SMARCA2) through immunohistochemistry (IHC) and found all (43/43) SCCOHT cases lacking BRG1 also did not express BRM (31). Interestingly, there are no mutations found in SMARCA2, implying a silencing event of SMARCA2 during tumorigenesis of SCCOHT or that SCCOHT might originate from cells lacking SMARCA2 expression. The dual loss of BRG1 and BRM is specific to SCCOHT, as the other ovarian tumors were either BRG1- or BRM-defective, but not both (32). BRG1 and BRM can be a promising marker for diagnosis of SCCOHT.

### **1.2.3 Cell of Origin and Pathogenesis**

SCCOHT is still listed within the category of miscellaneous ovarian neoplasms in 2014 World Health Organization classification (33), as the cell of origin for SCCOHT still remains debatable. IHC stains for SCCOHT are negative for inhibin, the differential marker for sex cord-stromal tumor (34, 35) and negative for HCG, PLAP and HPL which are the biomarkers for a germ cell origin (36, 37), implying SCCOHT does not share similar origin as the other rare type of ovarian cancer.

It has been suggested that SCCOHT is 'malignant rhabdoid tumor of the ovary', based on a similar genetic profiling. Malignant rhabdoid tumor (MRT) is an aggressive childhood tumor that usually occurs in the kidney. 26% of the cases are present with serum hypercalcemia (38), which is also observed in some cases of SCCOHT. MRTs have been reported to have loss of chromosome arm 22q, which leads to the identification of mutations in *SMARCB1*, a core subunit of SWI/SNF chromatin remodelling complex (39, 40). Later, researchers found out 2% of MRTs are driven by

deleterious mutation of *SMARCA4* instead of *SMARCB1*, and this is usually associated with a worse prognosis (41). As mentioned in the previous section, SCCOHT is now been characterized by mutations in *SMARCA4*. As both *SMARCA4* and *SMARCB1* are major components of SWI/SNF complex, their downstream product, DNA methylation patterns, are more strongly correlated between SCCOHT and MRT than between SCCOHT and HGSC (42). Besides the genetics and epigenetics similarities, Witkowski *et al* and Foulkes *et al* have also shown the similarities on the histological and clinical level. MRTs are also present with sheets of small cells with abundant eosinophilic cytoplasm, and presence of signet ring cells (also known as rhabdoid appearance). Similar to SCCOHT, for MRTs driven by loss of *SMARAC4*, it appears to be the only important DNA mutation in these MRT tumors (43). Given the morphological and genetic similarity between SCCOHT and MRTs, it suggests a common cell of origin or they are driven by *SMARAC4* or *SMARCB1* loss (29, 31, 42).

#### **1.2.4 Treatment and Prognosis**

SCCOHT represents less than 1% of the ovarian cancer, thus there is no standard or optimal treatment guidelines specific for SCCOHT. Surgical debulking followed by adjuvant chemotherapy is the primary treatment for small cell carcinoma. The most common chemotherapy regimen includes cisplatin/carboplatin in combination with etoposide (CE), or multi-agent regimen, VPCBAE (vinblastine cisplatin, cyclophosphamide, bleomycin, doxorubicin, etoposide) (18, 23). Although CE and VPCBAE are effective (44-47), recurrence is still rapid, within an average of 11.5 months (18, 23), and it occurs in over 60% of the cases. Treatment with VPCBAE is

associated with lower rate of recurrence (18, 23), but the survival rate is still low, 15.7 months on average.

The overall median survival rate is only 14.9 months, but several factors can favor the prognosis. Earlier stage disease is associated with improved survival. In Callegaro-Filho *et al* review, patients with stage I disease survive on an average of 35.3 months in comparison to stage IV disease of 3.3 months (23). Similar results were reported in Young *et al* review of 150 cases and Estel *et al* review of 135 cases (18, 21). Other factors such as normal serum calcium and absence of large cells also associated with longer survival rate (21). Interestingly, Estel *et al* also find tumors with larger diameters (>10cm) to be one of the favorable prognostic factors (18). However, due to the limited sample size, these prognostic factors should be interpreted with cautions.

Other treatment options, such as high-dose chemotherapy with autologous stem cell rescue has also been utilized in SCCOHT patient. After debulking surgery, patients underwent PAVEP (cisplatin, adriamycin, vepeside, cyclophosphamide) every 3 weeks for four to six cycle and followed by stem cell transplantation and high-dose consolidation chemotherapy with carboplatin, vepeside and cyclophosphamide. In Pautier *et al*'s study, the 5-year survival rate for 9 patients who were diagnosed as stage I disease is 100%, and 33% (confidence interval: 16% to 56%) for stage II-IV (n=21) (48). Other treatments like photodynamic therapy or other new chemo-agents, such as HDAC inhibitors have only been demonstrated to be effective in mouse xenograft models (49, 50).

## 1.3 SWI/SNF complex

### 1.3.1 Structure and function of SWI/SNF complex

The SWI/SNF complex was originally discovered in yeast for its critical role of mating-type switching (SWI) and sucrose fermentation (SNF) (51, 52). It utilizes energy generated by ATP hydrolysis to mobilize nucleosomes, modulate the chromosome accessibility and activate gene expression (53). SWI/SNF complexes are composed of 10 to 15 subunits, including one ATPase, core subunits and various combination of accessory subunits, and can be divided into two subtypes depending on the composition of accessory subunits. Two mutually exclusive ATPases, BRG1 (SMARCA4) and BRM (SMARCA2) are usually co-expressed in most tissue types and function when the SWI/SNF complex is intact (54). Core subunits, including SMARCB1 (SNF5), SMARCC1 (BAF155) and SMARCC2 (BAF170) are present in all variants of mSWI/SNF complexes. The BAF (BRG1-associated factor) complex exclusively contains accessory subunits such as ARID1A and ARID1B, whereas PBAF (polybromo BRG1-associated factor) complex exclusively contains PBRM1 and ARID2 (55, 56).

The function of the SWI/SNF complex was studied in *Drosophila* and mammals (57). Nucleosome mobilization involves disruption of histone-DNA interaction upon binding and DNA loop formation for downstream gene transcription (58). Unlike SWI/SNF complex in yeast, mSWI/SNF involves in both repression and activation of transcription. BRG1, for example, acts as an activator for CD4 expression and a repressor for CD8 expression activation during T lymphocyte development (59). It also inhibits for programmes associated with differentiation in embryonic stem cells (60).

### 1.3.2 SWI/SNF in cancer

As SWI/SNF complex plays critical roles in regulation of gene expression, it is linked with tumor suppression. In fact, over 20% of human cancers harbors mutation in genes encoding subunits in mSWI/SNF, and mutations in these subunits appear to be oncogenic (61, 62).

Malignant rhabdoid tumors (MRTs) was the first cancer type with mutations in SWI/SNF complex, of which 98% of the cases present SMARCB1 (SNF5) mutations (39, 40). Besides SMARCB1, ARID1A and SMARCA4 are the two other well-studied subunits. Ovarian cancer subtypes such as clear cell carcinoma and endometrioid carcinoma often have mutation in ARID1A subunits. Lung cancer often is associated with BRM or BRG1 mutations (Table 1.2). In most cases, these mutations lead to loss of protein expression and altered composition of SWI/SNF complex. As a result, with a deficient-SWI/SNF complex, regulation of target gene sets is altered and driven to a modified or new cellular dependency.

**Table 1.2 Summary of frequent mutations in SWI/SNF subunits.**

<b>SWI/SNF subunit</b>	<b>Example of Cancer Associated</b>
<b>SNF5 (SMARCB1)</b>	Malignant rhabdoid tumor (98%); Atypical teratoid/rhabdoid tumor (>95%)
<b>BRG1 (SMARCA4)</b>	SCCOHT (>90%); Non-small cell lung cancer; Malignant rhabdoid tumors (2%)
<b>ARID1A</b>	Ovarian clear cell carcinoma (46-57%); Endometrioid carcinoma of the ovary and uterus (30%)

Besides rewiring cellular dependency, these genetic perturbations can also lead to synthetic lethal opportunity, through which the deficiency in one of the subunits leads to the complex rely on the other subunits for proliferation. Several synthetic lethal relationships have been reported in mSWI/SNF, including SMARCA4 and SMARCA2 (63); ARID1A and ARID1B (64). For example, depletion of BRM (SMARCA2) in BRG1 (SMARCA4)-mutant lung cancer cell lines caused growth arrest, suggesting these BRG1-mutant cells were dependent on BRM for proliferation (63). Similar impaired proliferation was observed when depleting ARID1B in ARID1A-deficient cells (65). Following the identification of the synthetic lethal interaction, potential therapeutics are currently under development. Dasatinib, a receptor tyrosine kinase inhibitor, can selectively target ARID1A-mutant ovarian clear cell carcinoma (OCCC), leading to a significant reduction of peritoneal disease and ascites formation in mice xenografted with OCCC cells TOV21G (66). Given many cancers are driven by defective SWI/SNF and some of these mutations lead to specific dependency on residual complex, this could provide therapeutic targets with broad cancer relevance.

## **1.4 Polycomb Repressive Complex**

### **1.4.1 Structure and Role of PRC**

Polycomb repressive complex 1 (PRC1) and polycomb repressive complex 2 (PRC2), the two major complexes of polycomb group proteins (PcGs), are important epigenetic regulators in mammals. PRC1 and PRC2 act sequentially to regulate gene silencing through histone post-translational modification. PRC2 induces histone trimethylation at lysine 27 (H3K27me3) (67), which is then recognized by PRC1 to

further catalyze the monoubiquitylation of histone H2A on Lys 119 (H2AK119ub1) (68). Together PRC1 and PRC2 silence critical genes in cell differentiation, cell cycle regulation and many more (69, 70). Abnormal activity of PRC2 is involved in many different types of cancer, which makes PRC2 a potential therapeutic target for treating cancer.

The mammalian PRC2 consists at least five subunits, including enhancer of zeste homologue 2 (EZH2), embryonic ectoderm development (EED), suppressor of zeste 12 (SUZ12), RBBP4/7, and AEBP2 (71). EED and SUZ12 are the two most crucial components supporting catalytic function of EZH2, based on the *ex vivo* experiments (72). EZH2, the catalytic subunit of PRC2, adds methyl groups onto the lysine residue of proteins. The other subunits provide non-catalytic functions. EED subunit binds to repressive markers, including trimethylation of lysine 27 of histone H3 (H3K27me3), to recruit PRC2 to the site required further repression and provides positive feedback mechanism to EZH2 to further enhance methylation marker (73). SUZ12, on the other hand, senses the histone H3K27me3 on the chromatin, and thereby tightly regulates the EZH2 activity (74).

Based on whole exome sequencing of other cancer types, both gain and loss of function mutations are observed in EZH2. Deregulation of EZH2 is observed in a wide range of cancer types and there is much evidence suggests it has a critical role in tumorigenesis (75-77). Gain of function is observed in various cancers such as breast cancer, ovarian cancer and prostate cancer (78, 79). Overexpression of EZH2 is proven to be associated with poor prognosis, advance stage of disease and aggressiveness

(79). Kleer *et al* found that EZH2 expression were significantly higher in breast cancer cases with metastasis than the ones did not (78).

Many inhibitors targeting PRC2 have been evaluated in preclinical and clinical studies. As shown in Table 1.3, many of the available compounds target EZH2 catalytic activity through competing with S-adenosylmethionine (SAM) for binding in the SET domain, the methyltransferase site of EZH2. Among these compounds, GSK126 was tested in phase I clinical trials for non-Hodgkin's lymphomas (NHL), which reported very minimal clinical activity at the maximal dose used (80). EPZ-6438 is currently in phase II clinical trials for various tumor types including those with rhabdoid features, such as MRT or SCCOHT (81). CPI1205, another EZH2 inhibitor, is also in Phase I clinical trials for B-cell lymphomas. To avoid potential drug resistance, another approach of targeting EZH2 activity has been considered. In early 2017, two groups have independently synthesized compounds, A395 (82) and EED226 (83), both of which target the binding of EED to the H3K27me3 pocket, and prevents the further activation of EZH2 catalytic activity allosterically. MAK683, an improved version of EED226, is now in phase I/II for B-cell lymphomas and other solid tumors (84).

**Table 1.3 The list of PRC2 inhibitors and their clinical development status.**

<b>Compound</b>	<b>Mechanism</b>	<b>Disease</b>	<b>Status</b>
<b>GSK126</b>	SAM-competitive inhibitor	Non-hodgkin's lymphomas, SCCOHT	Phase I for non-hodgkin's lymphomas – discontinued (80)
<b>GSK343</b>	SAM-competitive inhibitor	Ovarian cancer (85), breast cancer and prostate cancer (86)	Preclinical
<b>EPZ-6438</b>	SAM-competitive inhibitor	B-cell lymphoma and other advanced solid tumor such as MRT, ovarian cancer	Phase II for MRT, SCCOHT, etc – ongoing (81)
<b>CPI1205</b>	SAM-competitive inhibitor	B-cell lymphomas (86)	Phase I for B-cell lymphomas (87)
<b>A395</b>	Target binding of EED to H3K27me3 pocket	B-cell lymphomas (82)	Preclinical
<b>EED226</b>	Target binding of EED to H3K27me3 pocket	B-cell lymphomas (83)	Preclinical
<b>MAK683</b>	EED inhibitor	B-cell lymphomas (84)	Phase I/II for B-cell lymphomas and other solid tumors (84)

#### 1.4.2 SWI/SNF - PRC2 antagonism

Several groups have shown the synthetic lethality of BRG1 and BRM in cancer cells of various types (63, 88, 89), implying the potential effective therapies for patients with defective BRG1 or BRM. However, dual loss of BRG1 and BRM in SCCOHT implies a different biologically approach is needed for treating SCCOHT. Accumulating evidence suggests the antagonism between SWI/SNF complex and Polycomb Repressive Complex 2 (PRC2) with respect to regulations of target genes (Figure 1.3) (61, 62, 90). In mouse embryonic stem cells (mESCs), PRC (PRC1 and PRC2) binds to the chromatin to keep the suppression of gene transcription. With the presence of functional SWI/SNF complex, PRC1 interacts with SWI/SNF, leading to eviction of both PRC1 and PRC2 along with the suppression markers, H3K27me3, leading to activated transcription of genes required for differentiation. With defective SWI/SNF, PRC remains on the chromatin and differentiation is blocked while expansion of progenitor cells remains active and ultimately supports tumorigenesis. Deletion of SMARCA4 gene leads to increased localization of PRC2 complex as well as its catalytic activity of trimethylation of lysine 27 of histone H3 in mESCs (91). Knockdown of EZH2, the catalytic subunits of PRC2, leads to reduction of cell proliferation in SNF-5 (SMARCB1) deficient malignant rhabdoid tumor cells *in vitro*, and completely blocks tumor formation *in vivo* (92). Therefore, targeting PRC2 might be a potential therapeutic approach for treating SCCOHT.

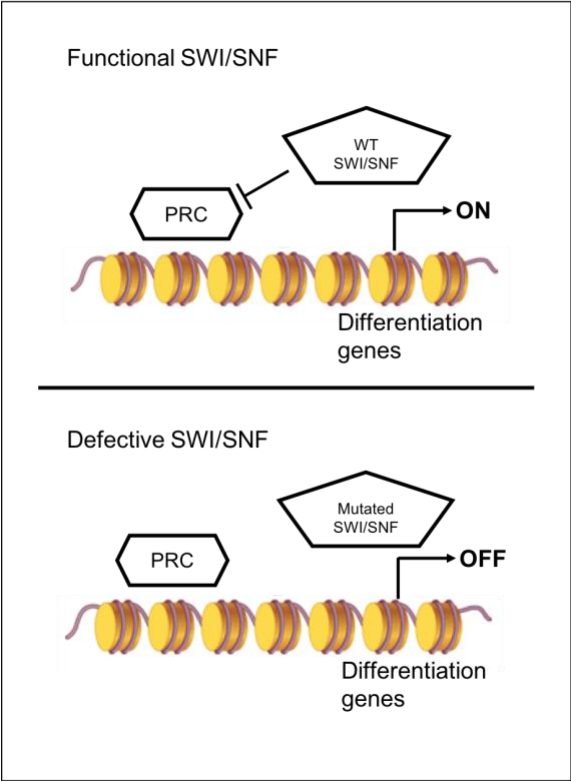


Figure 1.2 Antagonism between SWI/SNF and PRC complex.

## **1.5 Animal models for studying ovarian cancer and efficacy of anti-tumor therapeutics**

Unlike other cancer types, ovarian cancer is poorly understood, and the cell of origin remains unknown or disputed for many subtypes. Despite much effort to elucidate the biology for such a high-mortality disease, progress has been slow. One reason for this is that researchers have had difficulties of finding clinically representative models that can mimic ovarian cancer subtypes. Ovarian tumors are not made up of homogenous cells, but rather, it contains a very complex microenvironment, including primary tumor cells along with the other supporting cells, such as fibroblast and mesothelial cells, and inflammatory cells (93). There are different models for studying ovarian cancer, from the simple cell culture system to complex animal models.

### **1.5.1 Mouse models**

Animal studies, or preclinical drug studies, are often utilized to test potential toxicity, determine the possible dosage, and the outcome of novel treatments. Mice are often used in the cancer research because they are small, easy to handle and reproduce very fast (94). They share 99% of the genes with human and researchers can easily manipulate their genetics. Different immunodeficient mouse types are available for research, including three major mouse types: BALB, C57BL/6J, and NOD/LtSzJ, with a decreasing strength in their immune system (95). To successfully study human cancer in mice, innate immunity of host should be impaired, in which B-cell, T-cells and natural killer cells are absent, and other immune cells, such as dendritic cells and macrophages should also be defective. Mice with NOD/LtSzJ background

allow implantation of humanized tumor cells. The common immunodeficient strains used for ovarian cancer studies include NSG (NOD.*Cg-Prkdc<sup>scid</sup>Il2rg<sup>tm1Wjl</sup>/SzJ*), NRG (NOD.*Cg-Rag1<sup>tm1Mom</sup>Il2rg<sup>tm1Wjl</sup>/SzJ*) and SCID (NOD.CB17-*Prkdc<sup>scid</sup>/J*).

**Table 1.4 Comparison of mouse strain.**

<b>Strain</b>	<b>BALB</b>	<b>C57BL/6J</b>	<b>NOD/LtSzJ</b>
<b>Mature B cells/ T cells</b>	Absent	Absent	Absent
<b>Dendritic cells</b>	Present	Present	Defectives
<b>Macrophages</b>	Present	Present	Defective
<b>Natural killer cells</b>	Present	Present	Absent
<b>Leakiness</b>	Low	Absent	Absent
<b>Dendritic cells</b>	Present	Present	Defectives

### **1.5.2 Available xenograft models (subcutaneous, intra bursal, peritoneal)**

Xenograft models, where human cells are transplanted into mice, have been widely used for more than three decades due to its advantage in monitoring tumor growth and testing drug efficacy *in vivo* (96, 97). There are three main routes for ovarian tumor implantation, including subcutaneous (SC), intraperitoneal (IP) and intrabursal (IB) injection.

In SC xenograft, tumor cells are implanted into the back or flank of the mouse. This is most widely used approach among the three to test drug efficacy since it is easier to generate, and it is more convenient to monitor tumor growth when comparing to other two routes. However, its limitations are obvious since it does not mimic the proper microenvironment and recapitulate the tumor progression. In contrast, orthotopic models of ovarian cancer, such as IB and IP, develop tumors at the sites where corresponding human tumors forms. IP xenografts are derived by injections of tumor cells into the peritoneal cavity, and IB xenograft involves injection of tumor cells into the bursal membrane which encapsulates the ovary in mouse. Both models reproduce the clinical environment for ovarian cancer to develop (98, 99). IB xenograft recapitulates the early stage of the disease whereas IP xenograft represents the advanced stage where metastasis occurs. Shaw *et al* characterized different xenograft models for using 11 ovarian cancer cell lines, and they noticed not all of the cell lines developed tumor IB and IP (100). OVCA433, for example, did not development any visible IP disease after 90 days post inoculation, but others have reported its tumor-forming capabilities in SC, implying a change in microenvironment has effects on the tumor formation (100). Also,

ascites was observed in both IP and IB models and the overall survival rate was shorter than SC model (100).

Measurement of tumor growth in SC models are commonly conducted manually which introduce subjective and lacks accuracy. In contrast, tumors developed from orthotopic models are not measurable by calipers and often require the assistance of bioimaging.

### **1.5.3 Bioimaging System**

Non-invasive techniques are essential for monitoring the tumor progression in IB and IP models. There are four major techniques commonly applied to tumor detection and tumor burden measurement: positron emission tomography (PET), magnetic resonance imaging (MRI), and optical imaging including encompassing bioluminescence imaging (BLI) and fluorescence imaging (FLI) (101). As PET and MRI require expensive equipment and they both require expertise during operation and data analysis, optical imaging techniques are most commonly used for preclinical cancer research. BLI and FLI are suitable for animal studies with a large amount and high throughput imaging (101), considering that they are cost-effective and easy to operate. Two main aspects should be taken into consideration when choosing the right technique for tumor monitoring: small tumor detection and tumor burden measurement. BLI techniques rely on the expression of enzyme luciferase with the presence of ATP and oxygen. This creates minimal background signal noise as no external light source are present. Studies have reported that BLI is able to detect nonpalpable tumors (<1mm) and is capable of detecting tumor cells after 1 day of injecting tumor cells (101, 102). In

comparison, FLI requires external light for excitation and therefore is more sensitive to autofluorescence as a result of light absorbance and light reflection (103). Therefore, FLI has its limitations when detecting low signals due to the high background imaging. Studies have shown that signal intensity captured by either BLI or FLI strongly correlates with tumor volume (measured by caliper) (103, 104), which indicates that both techniques are applicable to tumor burden measurement.

Despite the fact that FLI is less sensitive than BLI when it comes to low signals and tumor detection, studies (104, 105) have demonstrated that FLI is a validated technique for detecting transplanted ovarian tumor cells and monitoring therapeutic effects in mouse studies. Moreover, BLI requires substrate injection and needs incubation time before imaging which is more time consuming and may cause extra stress to the animals. This becomes a particular important issue if the animals are already in studies involving frequent injection treatment, with daily or every other day schedule (106).

#### **1.5.4 mKate2 for imaging *in vitro* / *in vivo***

After the cloning of *gfp* gene in 1994 (107), green fluorescent protein (GFP) became widely used and researchers started to develop many other variants of fluorescent proteins (FPs) to cover almost the whole visible spectrum. Color, brightness and photostability are the major criteria to think before picking the most suitable FP for any experiments. In animal studies, far-red fluorescent proteins (RFPs) are usually used instead of others as it has a favorable spectral window for tissue light-penetration (~650-1100nm). Also, as wavelength increases (ie. far-red shifted), light-scatter intensity

decreases (108). Many of the far-red FPs are either dimeric or tetrameric, which make them unsuitable for *in vivo* use as their photophysics will be altered after oligomerization. To overcome this, many monomeric far-red FPs have been developed, such as mCherry, mKate2, TagRFP-T and mKO (109). Among them, mKate2 has the superior photobleaching dynamics *in vivo* (110) compared to other far-red FPs including mCherry, mRuby2 and TagRFP-T. Besides, it has also been reported that mKate2 has uniform and excellent brightness and photostability as well as low toxicity (111).

## 1.6 Rationale

As many of the preclinical anti-cancer drug testing are conducted in the subcutaneous xenograft model (ref.....), of which could contribute to the low concordance with the clinical data, a more comparable xenograft model is necessary. Intrabursal xenograft models, which tumors or tumor cells are implanted into the ovary of mouse, can provide an enriched microenvironment for tumor growth than subcutaneous models. However, the tumor monitoring for intrabursal models can be challenging as tumors are burdened inside the body. Florescence proteins can be a convenience tool to tag tumor cells for non-invasive tumor detection. Taken together, I hypothesize that the fluorescent intrabursal xenograft model can better resemble SCCOHT than fluorescent subcutaneous xenograft model.

With such low survival for SCCOHT, targeted therapy for patients is urgently needed. With the discovery of dual deficiency in the ATPase (SMARCA4 and SMARCA2) of SWI/SNF complex, the epigenetic synthetic lethality becomes a plausible approach. The efficacy of targeting components of PRC2, the antagonistic complex with

SWI/SNF, has been demonstrated in various SWI/SNF-deficient cancers. Thereby, I hypothesize that targeting subunits of PRC2 can be a potential therapeutic approach.

## Chapter 2: Methods

### 2.1 Cell culture, resistant cell lines

All of the cell lines were cultured in Roswell Park Memorial Institute (RPMI) 1640 medium (Thermo Cat. #11875093) supplemented with 5-15% FBS, except HEK-293T (ATCC #1573), which were cultured in Dulbecco's Modified Eagle Medium (DMEM) supplemented with 10% FBS.

BIN67 was derived from metastatic foci (pelvis) of SCCOHT (obtained from Dr. Barbara Vanderhyden, Ottawa Hospital Research Institute and Centre for Cancer Therapeutics, University of Ottawa) (112). SCCOHT1 were derived from recurrent SCCOHT (obtained from Dr. Ralf Hass, Medical University in Hannover, Germany) (113), and COV434 cells, derived from a cancer diagnosed as an ovarian granulosa tumor (114) that has lately been re-categorized as SCCOHT (Karnezis et al. manuscript in preparation). GSK126 resistance cell line derived from COV434, known as COV434<sup>EGR</sup>, was continuously cultured under 5 $\mu$ M of GSK126.

Human ovarian surface epithelium cell line, iOSE090 was provided by lab members. ES2, JHOC5, RMG1, OVISE and OVTOKO were derived from CCOC patients. NOY1 was derived from an ovarian yolk sac tumor (115). These ovarian cancer cell lines were provided by the lab members. Rhabdoid tumor cell lines, including A204 and G401, were kindly provided by Dr. Bernard Weissman (University of North Carolina). Lung cancer cell lines, including A549, H23, H522 and H1703 were a gift from Dr. Wan Lam (BCCRC). The sarcoma cell line VA-ES-BJ was a gift from Dr.

Neilson Torstein (UBC). The lymphoma cell lines, including DB and SU-DHL-10, were kind gift from Dr. Christian Steidl (BCCRC).

All the cells were maintained in a humidified 5% CO<sub>2</sub>-containing atmosphere at 37 °C and tested regularly for *Mycoplasma*.

## **2.2 Construction of mKate2-Expressing SCC $\alpha$ OHT cell lines**

Transfection of plasmids was performed according to manufacturer's instructions using PolyJet ( SignaGen, SL100688). Briefly, mKate2 plasmid (AddGene, 68441) transfection was performed on three SCCOHT cells at a confluence of ~80% for 24 hours, and cells were under G418 selection for 72 hours. Cells were sorted based on fluorescent signals and reseeded in 96-well plates to generate single clones. Clones were picked based on their proliferation rate, drug response towards known inhibitors (GSK126 and Qusinostat), and cell morphology. The clone sharing the most similarity was selected for *in vivo* models.

## **2.3 Drug Preparation**

GSK126 (Selleckchem, S7061), Qusinostat (Selleckchem, S1096), EED226 (Selleckchem, S8496) were used in *in vitro* drug testing. All drugs were dissolved in DMSO (Dimethyl Sulfoxide) (Sigma, 472301) to desired concentration and aliquoted into small volume. All the drugs were only allowed freeze and thawed cycle three times at most to prevent degradation.

## 2.4 Drug survival assay

Cells were seeded in 96-well plate in various density ranging from 500 cells/well to 2000 cells/ well, based on the proliferation growth curve. Cells were exposed to control (DMSO) or drugs (at desired concentration) 24 hours after seeding. Serial dilution was made to get the desired concentration. The amount of DMSO was equivalent to the highest drug volume used.

**For adherent cell lines**, crystal violet staining was used to determine the viability of cells after drug treatment. The method has been previously described (116). In brief, at the end of drug survival assay, cells were fixed in 96-well plate using 50 $\mu$ L of fixation buffer (10% methanol; 0.1% acetic acid) for 10 minutes, and then stained with 50 $\mu$ L of 0.5% crystal violet solution (in methanol) for 10 minutes. Plates were gently washed with tap water and air-dried overnight at room temperature. 40 $\mu$ L of 0.1% acetic acid were added to the wells to dissolve the stain, 120 $\mu$ L of water were added to each well before measuring the optical density (595 nm) with a plate reader. **For suspension cell lines**, CellTiter-Glo Luminescent Assay (Promega, G7570) was used to determine the viability, according to manufacture protocol. In brief, 100 $\mu$ L celltiter-glo compounds were added to each well at the end of the survival assay, and luminescent signals were obtained with integration time of 0.25 sec per well.

## 2.5 Western Blot Analysis

Cell lysis buffer [50mM Tris-HCl (pH 6.8), 2% SDS, 6%  $\beta$ -mercaptoethanol] was used for protein extraction from in vitro cultured cancer cells. RIPA buffer [150mM sodium chloride, 1.0% NP-40, 0.5% sodium deoxycholate, 0.1% SDS, 50mM Tris (pH

8.0)], supplemented with protease inhibitors (Roche Diagnostics, Basel, Switzerland), was used for protein extraction from mice tumor samples. Equal amounts of protein were separated by SDS-PAGE and were transferred to nitrocellulose membrane (ThermoFisher, LC2009). The membranes were blocked with 5% skim milk (in TBST) for 45 minutes, and then incubated with primary antibody for 2 hours, followed by secondary antibody for 1 hour. Membranes were developed using chemiluminescent detection system (Perkin–Elmer Life Sciences).

Primary antibodies used in this study were: 1) anti-H3K27me3 antibody (Millipore, 07-449); anti-EZH2 antibody (BD Bioscience, 612667), anti-GAPDH antibody (Abcam, ab9485), and anti-histone H3 antibody (Abcam, ab1791). Secondary antibodies used in this study were horseradish peroxidase-conjugated anti-mouse and anti-rabbit IgG (Amersham).

## **2.6 *In vivo* xenograft tumor model**

All procedures were carried out under the institutional guidelines of the Animal Care Committee of 185 the University of British Columbia (A14-0290).

For subcutaneous xenograft experiments,  $1 \times 10^6$  cells (SCCOHT1-mKate2 and COV434-mKate2) or  $5 \times 10^6$  cells (BIN67-mKate2) in 50% Matrigel / 50% RPM1 (Corning) in a final volume of 100  $\mu$ L were inoculated into the backs of female NRG (NOD.Rag1KO.IL2R $\gamma$ KO) mice. For intrabursal experiments,  $1 \times 10^5$  cells (SCCOHT1-mKate2 and COV434-mKate2) or  $5 \times 10^5$  cells (BIN67-mKate2) in PBS in a final volume of 10  $\mu$ L were inoculated into the left ovary of NRG mice. For intraperitoneal experiments,  $1 \times 10^6$  cells (SCCOHT1-mKate2 and COV434-mKate2) or  $5 \times 10^6$  cells

(BIN67-mKate2) in PBS in a final volume of 100  $\mu$ L were inoculated into the peritoneal of female NRG mice. Tumor length (L) and width (W) measurements was obtained at three times a week. Tumor volumes were calculated according to the equation  $\text{Length} \times \text{Width}^2 \times 0.52$  with the length (mm) being the longer axis of the tumor. Tumor signals were measured once a week using fluorescence imaging system. Mice were euthanized where the tumor volume reached 1000  $\text{mm}^3$ . Tumor were harvested upon necropsy and formalin-fixed.

## **2.7 Fluorescence Imaging and data processing**

The area of tumor cells inoculation sites was shaved prior to the imaging. Mice were anesthetized and placed in the imaging chamber (on warmed stage) of the Maestro (fluorescence) imaging equipment with noses positioned in nose cones for continuous isoflurane flow. Exposure time ranging from 5-100ms were used to acquire fluorescent signals. Images were taken weekly, and mice were monitored closely for any signs of morbidity associated with repeated anesthesia.

Images were processed according to manufacturer's manual. Briefly, inoculation site with mKate2 signal was defined as region of known spectrum (ie. red), and naive NRG mouse was defined as black. Region of interest was automatically generated by Maestro software based on the given spectrum (red and black). Total signal was calculated within the region of interest and used as the output of mKate2 fluorescent signals. Total signals, with same exposure time, over the time course of tumor progression of the same mouse were plotted. Total signal counts with the same exposure time were compared among different mice.

## 2.8 *In vivo* toxicity test and efficacy studies

For *in vivo* toxicity experiment, EED226 (MedChem, 2083627-02-3) was formulated in 0.5% HPMC and 0.5% Tween-80 as solid suspension by sonication. Tumor-free NRG mice were treated with either Vehicle, 10 mg/kg or 40 mg/kg EED226 orally twice daily (BID PO) (0800/1600 hr), for 3 consecutive weeks (n=3). Mice body weight were measured three times a week, and mice were monitored closely for any signs of morbidity associated with EED226.

For efficacy study, COV434-mKate2 cells were injected subcutaneously to the back of the female NRG. Mice were randomized to treatment arms (n=8) once the average of tumor reached 100 mm<sup>3</sup>. Vehicle, 10 mg/kg or 40 mg/kg EED226 was administered orally by gavage for 3 consecutive weeks, with one day break between each week (M-Sat). At the end of first week of dosing, 10 mg/kg arm was increased to 80 mg/kg EED226 to serve as another toxicity test in tumor-bearing (COV434-mKate2) mice. Mice were euthanized once the humane endpoints reached or at the end of 3-week dosing. Tumors were harvested as both frozen for protein extraction and formalin-fixed for histological examination by IHC staining.

For combined toxicity and efficacy pilot study, SCCOHT1-mKate cells were inoculated subcutaneously to the back of female NRG. Mice were randomized to treatment arms (n=4) upon tumor size reaching 100 mm<sup>3</sup>. Vehicle or 200 mg/kg EED226 was administered through oral gavage for 2 consecutive weeks without break. Tumors were excised and weighed upon necropsy, and snap freeze for further analysis.

## 2.9 Statistical analysis

Statistical significance between two was determined by student's *t*-test in all experiments. Survival curves and IC<sub>50</sub> of drug treatment were determined by Prism. A *p*-value < 0.05 was considered as significance.

# Chapter 3: Development of fluorescence-labelled SCCOHT xenograft models

## 3.1 Background

Mouse models have been widely used for drug efficacy testing under various conditions. The subcutaneous xenograft model is the most widely used model for preclinical drug evaluation, mainly due to easy-accessible tumor monitoring and measurement (117). Subcutaneous tumor implantation is usually established on the back or in the flank of the mice, as it is believed that transplantation at these locations causes the least distress and will not interfere with normal body functions such as eating and drinking. However, subcutaneous models do not provide comparable microenvironment for tumor progression, as compared to primary cancer sites, which may result in altered drug response (117). Another drawback of such models is that they rarely metastasize as the tumors are usually encapsulated in the subcutaneous tissue (118). Therefore, the outcome of the preclinical therapeutic efficacy studies performed in subcutaneous xenograft models may not represent the clinical outcome.

Orthotopic xenograft tumor models, on the other hand, which are created by implanting the tumor cells at its site of origin, mimic the tumor microenvironment better, and relevant metastasis have been reported in many orthotopic models (100, 119). For example, human prostate cancer cell, PC-3, injected into the prostate of nude mice produces tumor and metastasizes to paraaortic lymph nodes (120). Orthotopic xenograft models of various cancer have been used in antitumor therapeutic

experiments in preclinical studies, including colon, pancreatic, liver, lung and brain tumors (121). Injection of tumor cells into the intrabursal layer of the ovary in mice is the common orthotopic approach for studying ovarian cancer cells *in vivo*. But due to the labor-intensiveness of intrabursal injections, an intraperitoneal model is also used to study ovarian cancer. This is appropriate for the most common subtype of ovarian cancer, high grade serous carcinomas, as this cancer type metastasizes to the peritoneal cavity. Several studies have investigated the difference between intrabursal and intraperitoneal model, by comparing metastasis sites and histological staining of the tumor, and found intraperitoneal models can mimic the metastasis ability of disease better, as it spreads in the peritoneal better, whereas intrabursal mimics the local tumor progression (100).

Despite both orthotopic xenograft and intraperitoneal xenograft models being an improvement over subcutaneous xenograft models, there are some major drawbacks. The most obvious limitation is the lack of reliable ways to monitor the tumor growth and to track metastasis. In addition, the identification of the humane endpoint by tumor volume can be challenging. For orthotopic models, the endpoint more relies on the clinical observation of the mice, which is subjective and therefore not optimally reproducible. As an alternative, the development of cancer cell lines stably expressing fluorescent proteins allows real-time detection and visualization of tumor growth as well as metastasis in live animals.

During the past decades, many fluorescent proteins (FP) with a variety of emission wavelengths, isolated from marine organisms, have been tested in bioimaging

both *in vitro* and *in vivo*. FPs with emission greater than 600nm (far-red and near infra-red) are more suitable for tumor bioimaging than the rest of the FPs for its better tissue penetration property as well as lower light scatter intensity (122). The mKate2, a recently discovered far-red fluorescent protein (FRFP), has demonstrated high brightness and stability, along with lower background signals and low cytotoxicity to cells (111). These suggest that FP imaging, specifically mKate2, can be used as a convenient tool for early detection of tumor progression in orthotopic xenograft models.

The objective of this chapter is to develop mKate2-labelled SCCOHT cell xenograft models that can provide non-invasive tumor imaging. The specific aims include:

Aim1. Establishment of SCCOHT-mKate2 cell lines

Aim2. *In vivo* tumor model development of SCCOHT-mKate2 cells lines.

## **3.2 Results**

### **3.2.1 Isolation of SCCOHT cell lines stably expressing the mKate2 fluorescent protein**

The mKate2 plasmid was purchased from Evrogen (cat. # FP181). The vector contains SV40 origin for replication in mammalian cells, and SV40 promoter which contains neomycin (G418) resistance gene for stable transfection selection.

All three SCCOHT cells (BIN67, COV434 and SCCOHT1) were cultured in medium containing G418 at 48 hours post transfection. After G418 selection for a week, cells were imaged with a fluorescent microscope, which demonstrated that only ~10% of

cells expressed mKate2 fluorescent signal (Figure 3.1A). Cells were then sorted based on the intensity of the fluorescent signal (Figure 3.1 B). However, not all of the sorted population were expressing stable signals. Some of the cells lost their mKate2 expression after several passages, even though they were under G418 selection (Figure 3.1 C). This was observed in all three transfected cell lines. In parallel to collect bulk sorted cells, single cells with high fluorescence were seeded into 96-well plates to isolate single clones that can express fluorescent signals ubiquitously. One clone from BIN67 cells and one clone from COV434 cells were successfully isolated (Figure 3.2 A, B), which were designated as BIN67-mKate2 and COV434-mKate2, respectively. In these clones, expression of mkate2 was seen in all cells and persisted in later passages (Figure 3.2 A, B). As SCCOHT1 cells do not proliferate as single cells, only one well with three clones grew up, which were collected and designated as SCCOHT1-mkate2. These cells expressed mKate2 expression in more than 95% of the population with variable intensity (Figure 3.2 C). Despite that they contained mixed populations, the pattern of mKate2 expression in SCCOHT1-mkate2 cells did not alter in later passages (Figure 3.2 C.).

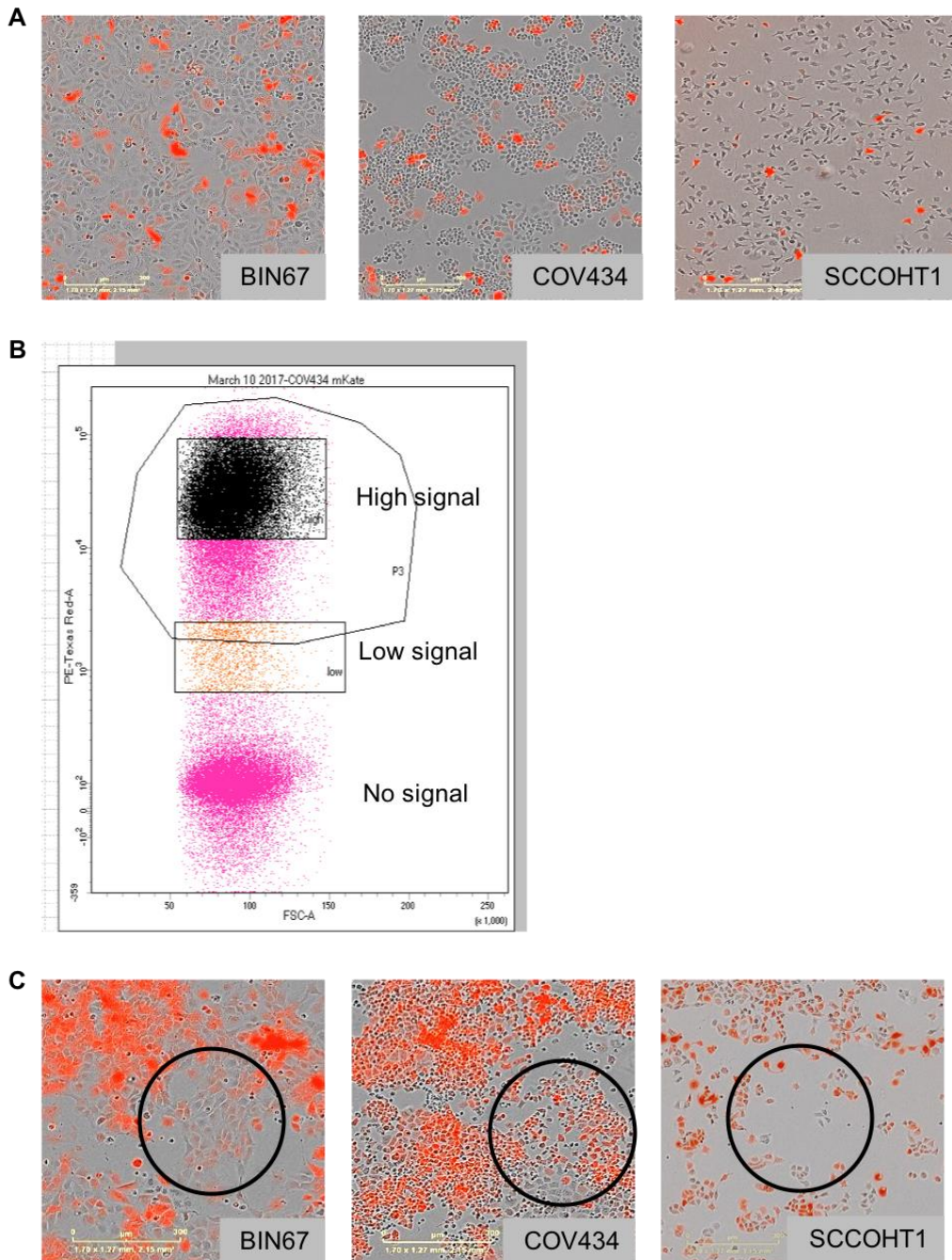


**Figure 3.1 Transfection of mKate2 into SCCOHT cells.**

(A) SCCOHT cells were transfected with mKate2 using PolyJet and under G418 selection for a week, and (B) sorted based on the intensity of fluorescence. (C) Sorted population were not fully expressing stable mKate2 signal, as circled out.

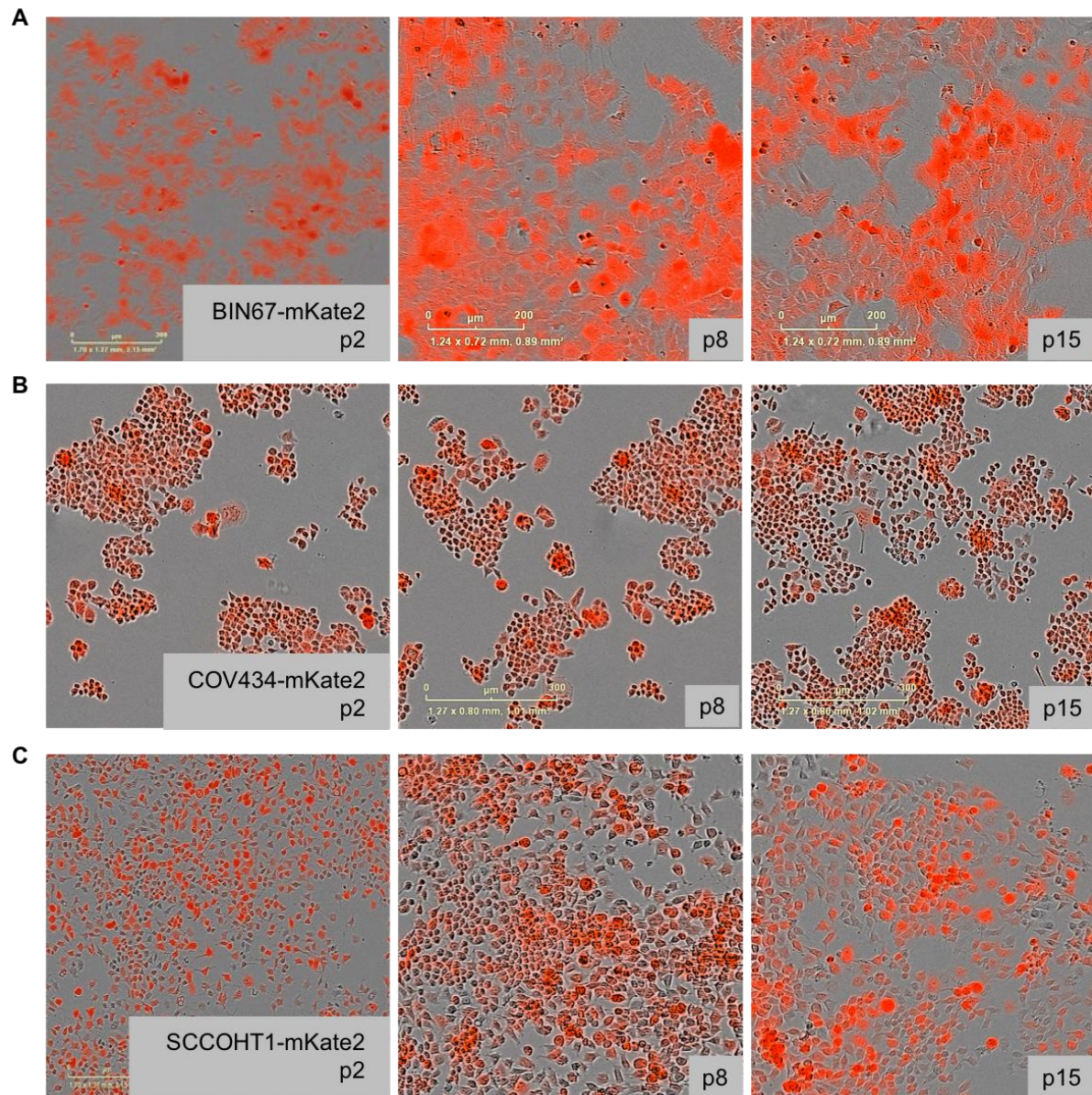


**Figure 3.2 Isolation of SCCOHT clones with stable mKate2 expression.**

Isolation of single clone from sorted population with stable mKate2 fluorescent signal in (A) BIN67 and (B) COV434. Pooled clones with stable mKate2 fluorescent signal in (C) SCCOHT1.

### **3.2.2 mKate2-labelled SCCOHT cells mimic their parental cells biologically *in vitro***

To ensure mKate2-labelled SCCOHT cells function similarly as the parental cells, their cell morphology, proliferation rate and drug response towards several pharmaceutical inhibitors were analyzed in comparison to their parental counterparts. All cells were seeded in 96-well plates at the same seeding density. Growth curves were generated by Incucyte, a real-time live cell imaging system. As shown in Figure 3.3 a, all three SCCOHT-mKate2 cell lines proliferated at a comparable rate as the parental cells, and they shared very similar cell morphology (Figure 3.2 A, B, C). Our lab has previously reported that SCCOHT cells are sensitive towards pharmaceutical compounds, such as EZH2 inhibitors (123) and HDAC inhibitors (124). To ensure introducing mKate2 does not affect the intrinsic biological mechanism, these mKate2 expressing SCCOHT cells were also exposed to these pharmaceutical compounds, along with EED inhibitor, EED226, which will be discussed further in the next chapter. All three mKate2 expressing cells had very comparable IC<sub>50</sub> towards all compounds tested when compared against their non-expressing source lines (Figure 3.3 B, C, D).

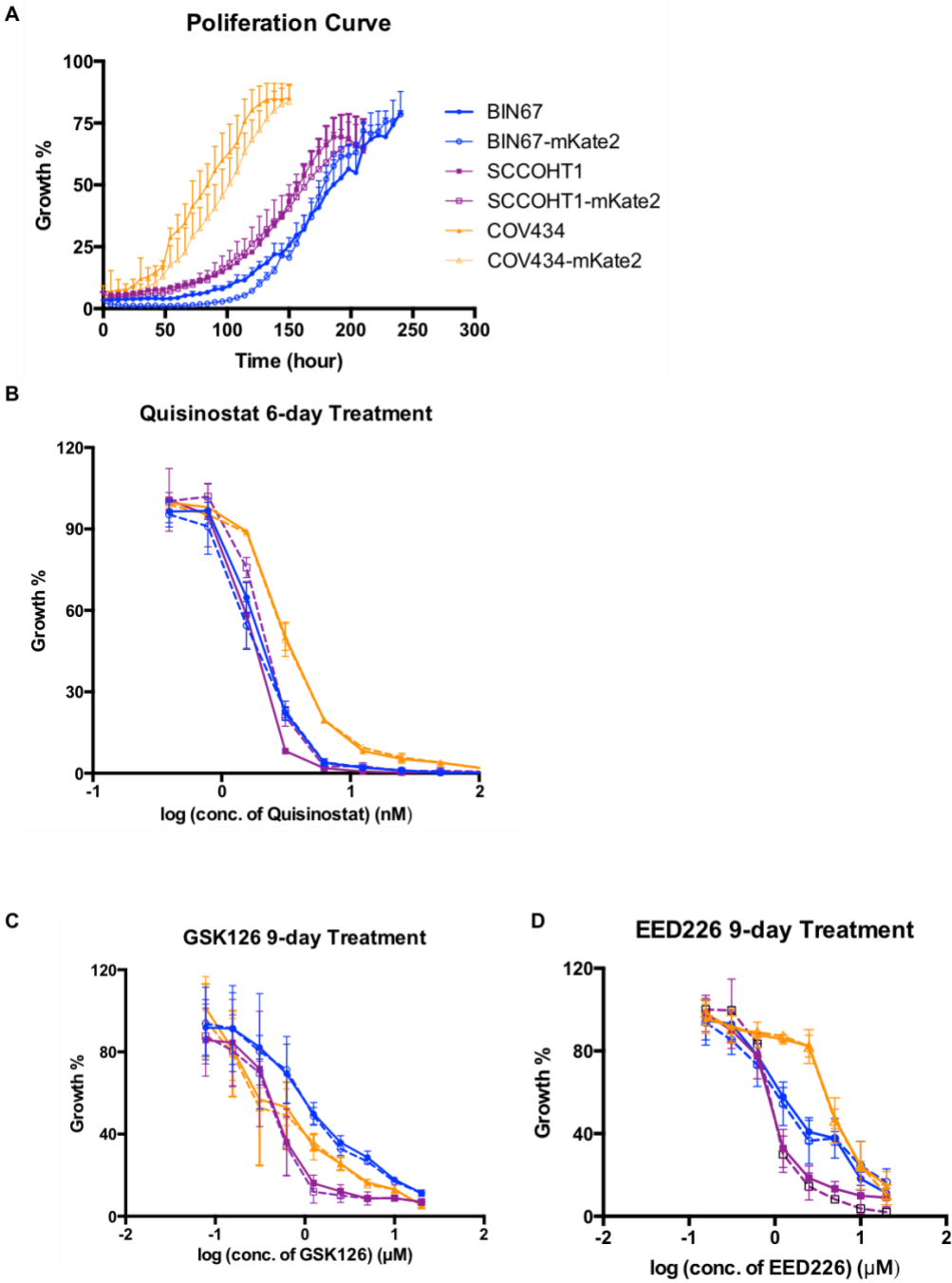


**Figure 3.3 Characterization of isolated clones.**

Isolated cells along with the parental cells were seeded in 96-well plates for (A) proliferation monitoring and 6-day drug survival assay for (B) HDAC inhibitor and (C) EZH2 inhibitor, and 9-day assays for (D) EED inhibitor.

### 3.2.3 Subcutaneous xenograft models of mKate2-labelled SCCOHT cells in NRG mice

To test their ability to form tumor *in vivo*, BIN67-mKate2 ( $4 \times 10^6$  cells/mice), COV434-mKate2 ( $2 \times 10^6$  cells/mice) and SCCOHT1-mKate2 ( $2 \times 10^6$  cells/mice) were inoculated to the back of the female NRG mice subcutaneously. The number of cells for injection was chosen based on previous studies with corresponding parental SCCOHT cell lines in our lab and other labs (125). NRG mice were selected for *in vivo* studies as they are one of the most immuno-deficient strains that support the growth of human primary tumors. Fluorescence was captured in all three SCCOHT xenograft models three days post tumor inoculation, whereas tumor mass became palpable after one to two-week post inoculation, depending on the cell line used (Figure 3.4 A). Signal with various exposure time (5 ms to 100 ms) was captured to find the optimal exposure time (Figure 3.4 B). At the early stage of tumor growth, when tumor was still small with weak fluorescent signals, short exposure time cannot capture the fluorescence signal effectively, especially around the edge area. Whereas, during late progression stage, when tumor became larger with strong signals, longer exposure time saturated the signal. In Figure 3.4 B, a representative example of the fluorescence signal of a COV434-mKate2 subcutaneous tumor at day 39 with various exposure time is depicted. Arrow depicted the presence of oversaturation. When tumor was lower than  $100 \text{ mm}^3$ , shorter exposure time, such as 5 ms cannot captured the signal completely, as the background was too strong. The total signal between 50 ms and 100 ms various very little when tumor reached over  $600 \text{ mm}^3$ , but the total signal at 50 ms and 100 ms still increased as tumor grew larger, implying the saturation of the signal at 100 ms. This

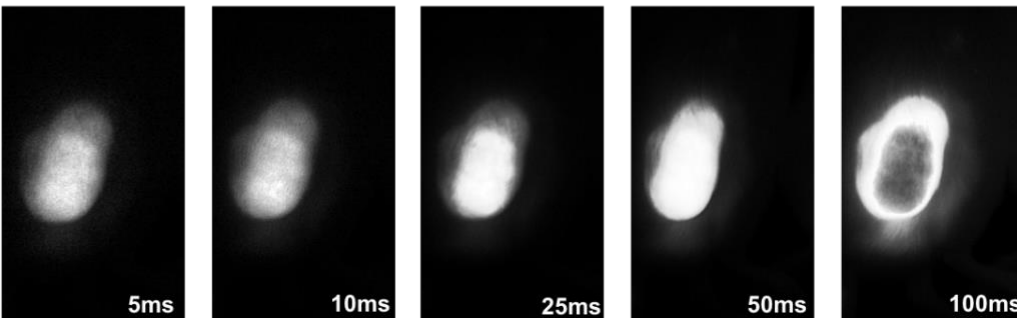
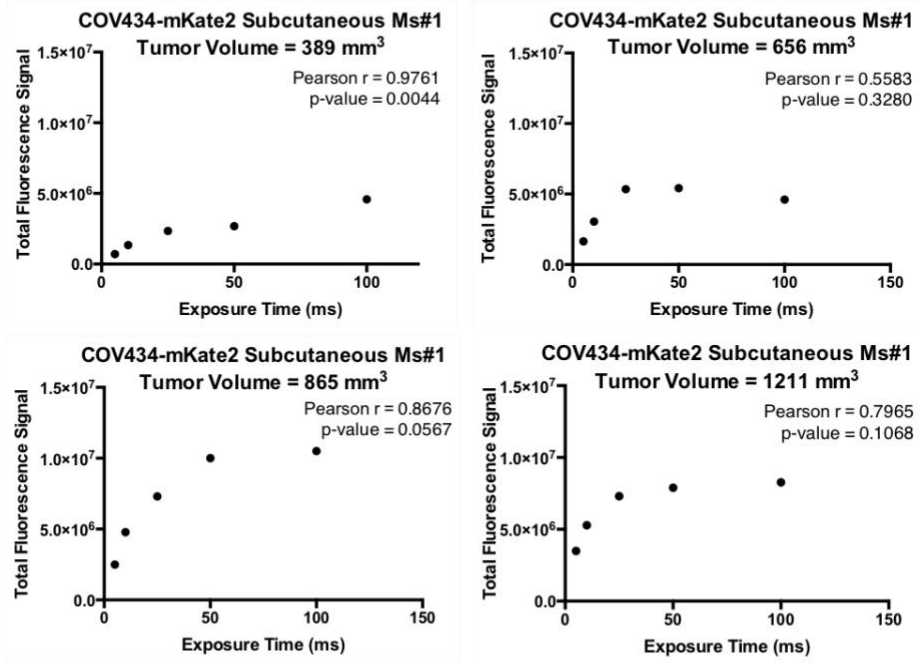
was further confirmed by the images captured, where highly saturated signal was shown in the 100 ms exposure time, in comparison with 10 ms (Figure 3.4 B). Based on all of the fluorescence signal from tumor progression in each cell line model, exposure time from 10 ms to 25 ms is optimal range. 25 ms was picked for the subsequent data analysis, as it provided reliable signal for tumor 2 days post inoculation and still showed different strength of signal when mice reached humane endpoint (tumor greater than 1000 mm<sup>3</sup>).

To determine whether the *in vivo* fluorescent signal correlates with the size of tumor, standard caliper-based measurement was used to determine the tumor volume. Mice injected with COV434-mKate2 and SCCOHT1-mKate2 cells developed measurable tumors around 15±2 days post inoculation and reached humane endpoints at day 34±4 and 32±2, respectively (Figure 3.4 C). BIN67-mKate2 model took much longer to grow *in vivo*. Average tumor size was still under 500 mm<sup>3</sup> 50 days post inoculation. Fluorescence signal was also plotted over the tumor progression time course (Figure 3.4 D). Fluorescent signals increased over time till tumor size reached humane endpoint (COV434 and SCCOHT1) or 500 mm<sup>3</sup> (for BIN67), which shared very similar progression trend as tumor volume measured by caliper. To determine whether the fluorescence signal can be utilized as a means to indicate tumor volume, all the signal data points were plotted against the corresponding tumor volume (Figure 3.4 E). Pearson correlation coefficient was calculated in each model, and all three models had strong correlation ( $p < 0.0001$ ) between the total fluorescent signal captured and tumor volume captured by caliper, indicating a linear relationship between fluorescence signal and tumor volume. In general, fluorescent signal reflects the volume of the tumor.

A



B



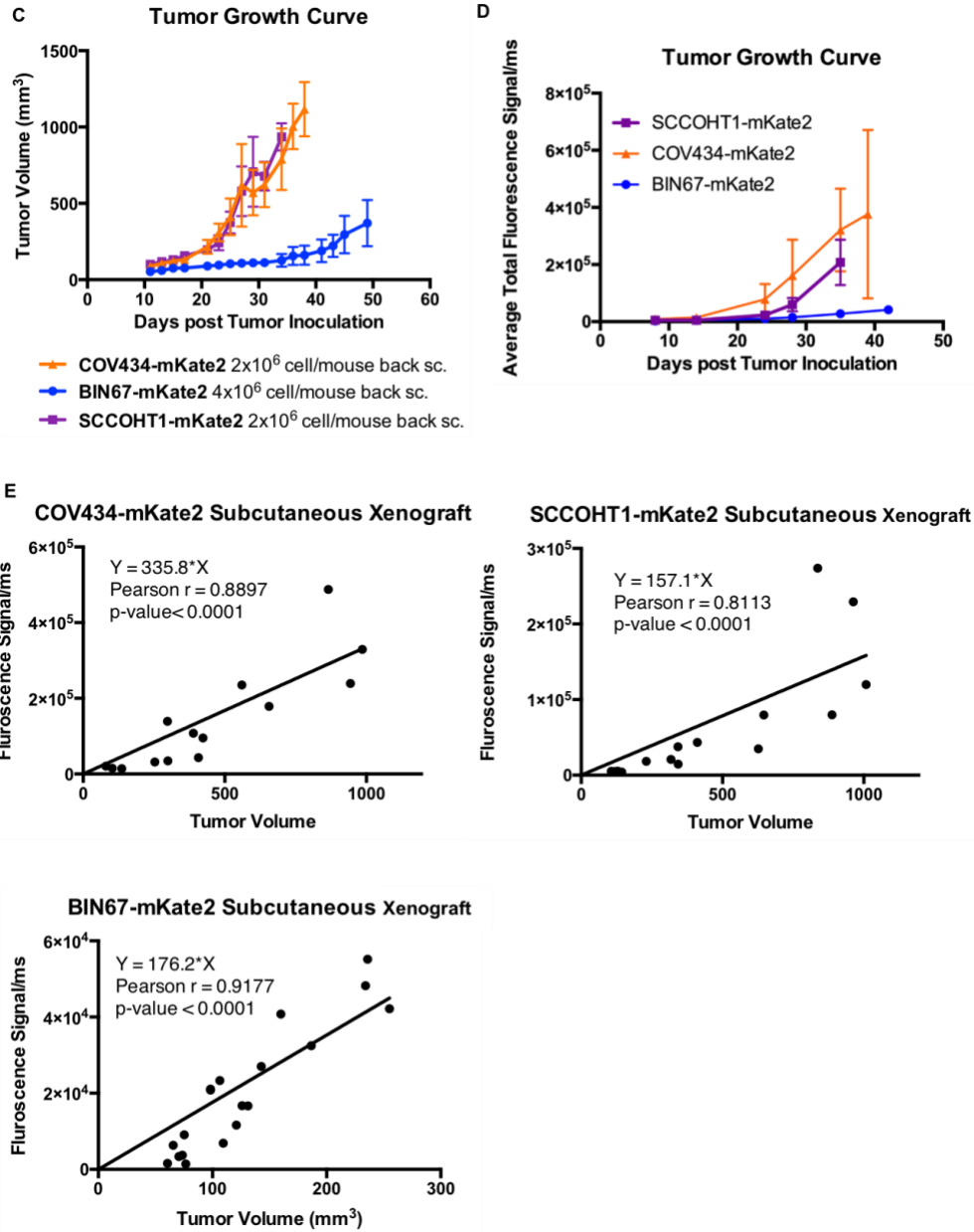


**Figure 3.4 SCCOHT subcutaneous model development.**

All three mKate2 expressing cells were injected to the back of female NRG mice at the indicated cell density. (A) Fluorescent signals were captured once a week with various exposure time. (B) Signals are converted to black and white for quantification using Maestro software. White indicates the presence of fluorescence and black represents non-fluorescence. Arrow indicates oversaturation of the signal. Tumor progression based on tumor volume using (C) caliper and (D) fluorescence signal. (E) Correlation between fluorescent signal and tumor volume were generated with best-fit line, Pearson correlation,  $r$ .

### 3.2.4 SCCOHT intrabursal xenograft model in NRG mice

To mimic the microenvironment of SCCOHT, BIN67-mKate2 ( $5 \times 10^5$  cells/mice), COV434-mKate2 ( $1 \times 10^5$  cells/mice) and SCCOHT1-mKate2 ( $1 \times 10^5$  cells/mice) cells were inoculated into the right ovary of female NRG mice. In mice ( $n=6$ ) injected with COV434-mKate2 cells, fluorescent signals were detected three weeks post surgery, but tumor mass only became palpable  $5 \pm 2$  days after the appearance of fluorescent signal (Figure 3.5 A). Fluorescent signal was increased as tumor progressed, and some mice had a drop in the signal at humane endpoint, implying necrosis inside the tumor (Figure 3.5 B). Tumors grew  $35 \pm 5$  days post-surgery, or  $20 \pm 5$  days after first sign of fluorescent signal, till animals reached their humane endpoint based on the clinical observation assessment, such as body weight change, sign of dehydration or pains. Among these health observations, body weight change was the most noticeable variable. When the tumor became palpable, the body weight increased by around 10%, implying the change in body weight can be another mean to monitor the tumor growth (Figure 3.5 C). All mice developed intrabursal tumors along with presence of ascites, but none metastasized (Figure 3.5 D). There was a trend that tumor weights correlated with fluorescence signals, but as the sample size ( $n=3$ ) was too small, it did not reach significance ( $p=0.10$ , Pearson test).

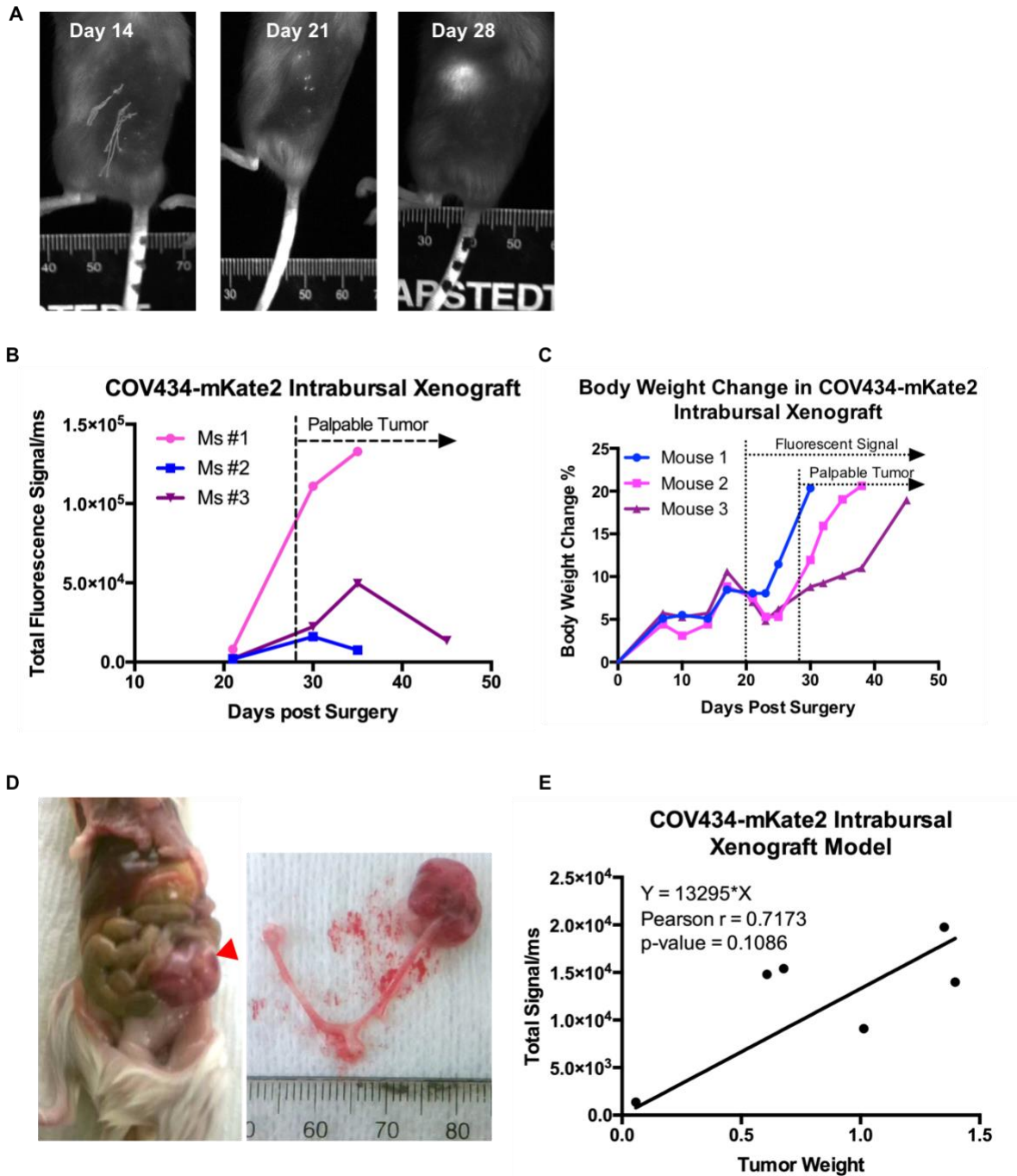


**Figure 3.5 COV434-mKate2 intrabursal xenograft model development.**

$1 \times 10^5$  cells of COV434-mKate2 were injected into the right ovary of female NRG. (A, B) Fluorescent signal was monitored once a week. (C) Animals were weighted two times a week (D) No metastasis was observed in the intrabursal model. Tumor indicated by red asterisk. (E) Tumor weight was recorded at the end of the study.

In mice (n=3) injected with SCCOHT1-mKate2 cells, only one of the animals had strong mKate2 expression, and the remaining two had very neglectable fluorescence signal (Figure 3.6 A, B). For the one (Mouse #1) with strong mKate2 signal, signal increased as tumor progressed (Figure 3.6 C). SCCOHT1-mKate2 intrabursal model took longer time to progress than COV434-mKate2 model. SCCOHT1-mKate2 model can grow up to 43±5 days post tumor cell inoculation, and fluorescence signal showed up on day 21, indicating this model can provide longer window for efficacy studies. No metastasis was found in any of the SCCOHT-mKate2 mice, but ascites was observed in two of the mice (Figure 3.6 D).

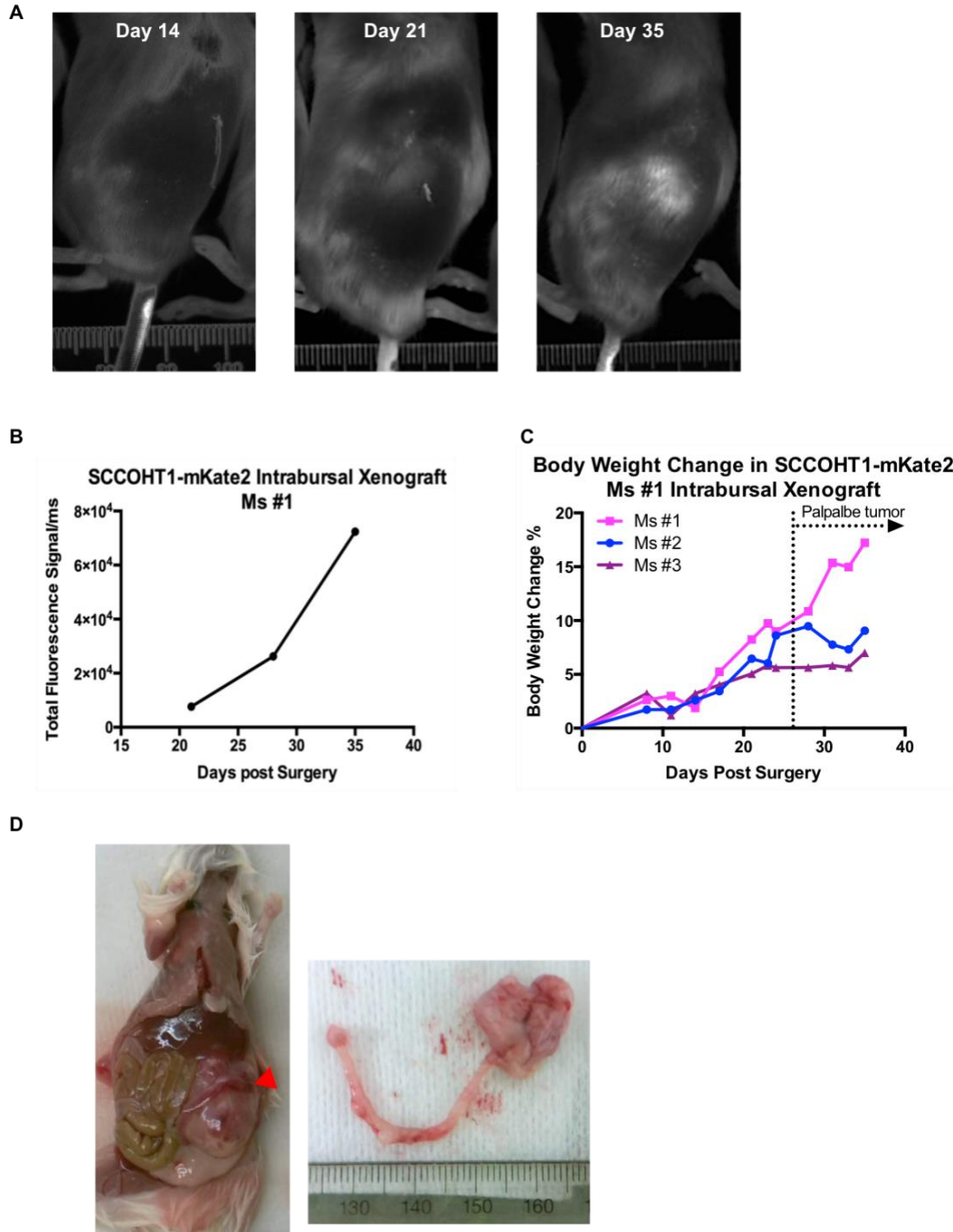


**Figure 3.6 SCCOHT1-mKate2 intrabursal xenograft model development.**

$1 \times 10^5$  cells of SCCOHT1-mKate2 were injected into the right ovary of female NRG. (A, B) Fluorescent signal for Ms #1. (C) Animals were monitored three times a week. (D) No metastasis was observed in the intrabursal model. Tumor indicated by red asterisk.

In mice (n=3) injected with BIN67-mKate2 cells, all three mice developed intrabursal tumor successfully (Figure 3.7 A). Tumor signals, however, vary from mouse to mouse and the angle the signal was captured (Figure 3.7 A). Before termination, signal for mouse #3 was captured twice, both dorsal and ventral on day 84. As shown in Figure 3.7 A, different position gave off different signal intensity (exposure time = 50 ms), implying position is critical in bioimaging.

Mouse #1 (also shown as Ms #1) was terminated earlier in the study to check the growth of intrabursal tumor. For Mouse #2 and #3, as tumor grew larger, fluorescence signals increases (Figure 3.7 B), but Ms #3 had a drop in signal at the last time of measurement. Similar to the other two cell line models, the tumor became palpable when body weight change reached 10% (Figure 3.7 C). BIN67-mKate2 intrabursal model took much longer time to progress than the other two SCCOHT cell line model. It can grow up to  $75\pm 5$  days post tumor cell inoculation. Unlike the other two cell lines, BIN67 was derived from metastatic foci of SCCOHT. Thus, metastasis was observed in all three mice, sites including spleen and peritoneal wall, despite the size of the primary tumor. The metastasis was further confirmed by bioimaging (Figure 3.7 D), and asities were present in two mice.

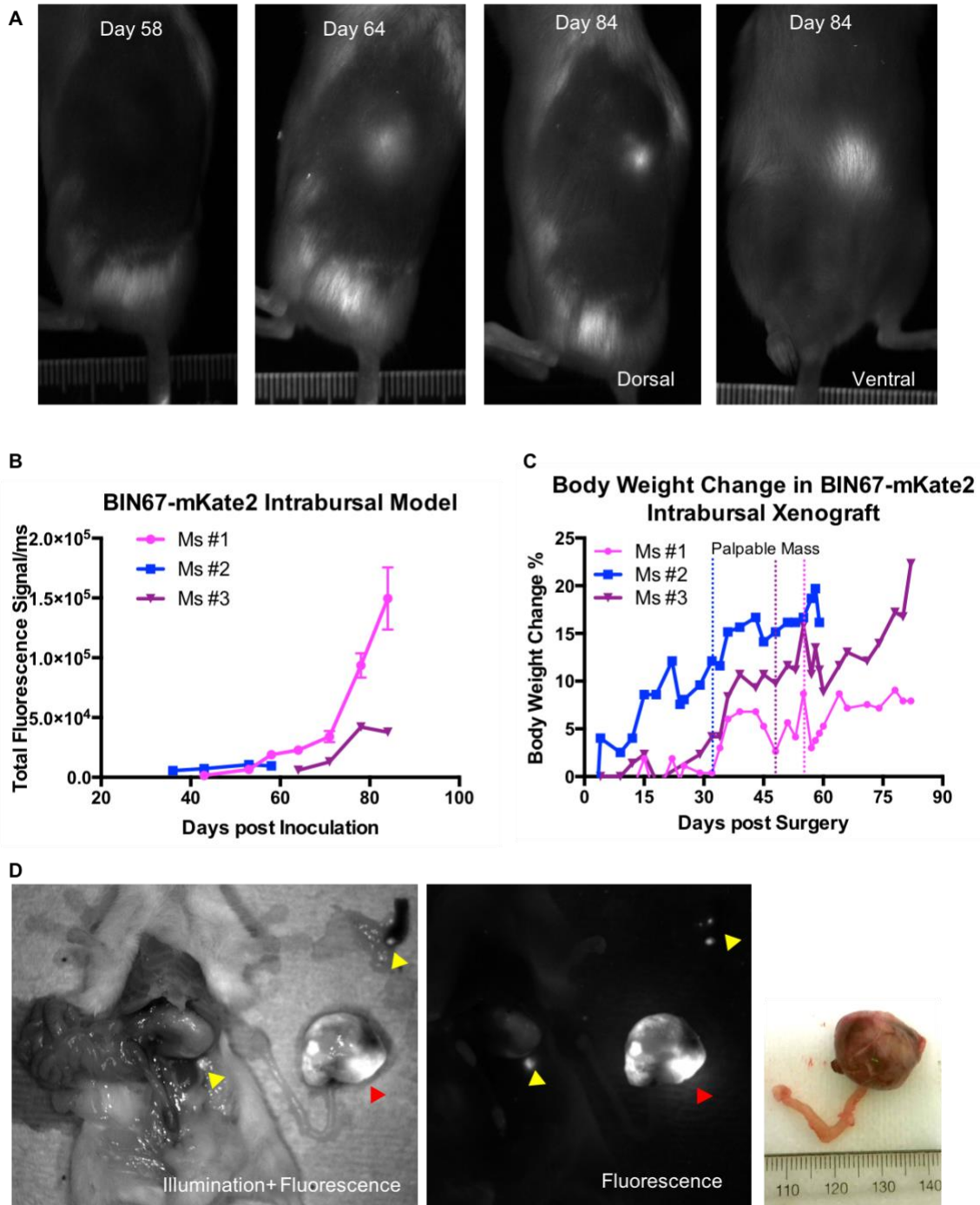


**Figure 3.7 BIN67-mKate2 intrabursal xenograft model development.**

$5 \times 10^5$  cells of BIN67-mKate2 were injected into the right ovary of female NRG. (A) Fluorescent signal of mouse #3. (B) Fluorescent signal was monitored once a week. (C) Animals were weighted two times a week. (D) Metastasis (Yellow asterisk) was observed in the intrabursal model. Primary tumor indicated by red asterisk.

### 3.2.5 Tissue attenuation in intrabursal model

As signals obtained from intrabursal model had much lower signal than that in subcutaneous model, fluorescence signals were compared between *in vivo* and *ex vivo* measurement of intrabursal tumors to investigate whether the surrounding tissue would absorb some of the fluorescence signal. The *in vivo* signal of COV434-mKate2 intrabursal tumors was 10-fold less than the *ex vivo* signal (p-value = 0.0125) and 45-fold less than the subcutaneous tumors at comparable sizes (p-value = 0.098) (Figure 3.8 A). In SCCOHT1-mKate2 model, *in vivo* signal was 5-fold less than *ex vivo* signal (p-value = 0.509) and 17-fold less than subcutaneous tumors at comparable sizes (p-value = 0.083) (Figure 3.8 B). *In vivo* signal was 3-fold less than *ex vivo* signal in BIN67-mKate2 model (p-value=0.468), and 6-fold less than subcutaneous tumors (p-value=0.002). The difference between *in vivo* and *ex vivo* signals implies that tissues surrounding the tumor could absorb the emission signal during imaging section. The difference in signal strength between *ex vivo* intrabursal model and subcutaneous model could be caused by the necrosis or other issues, which will be discussed further in the following section.

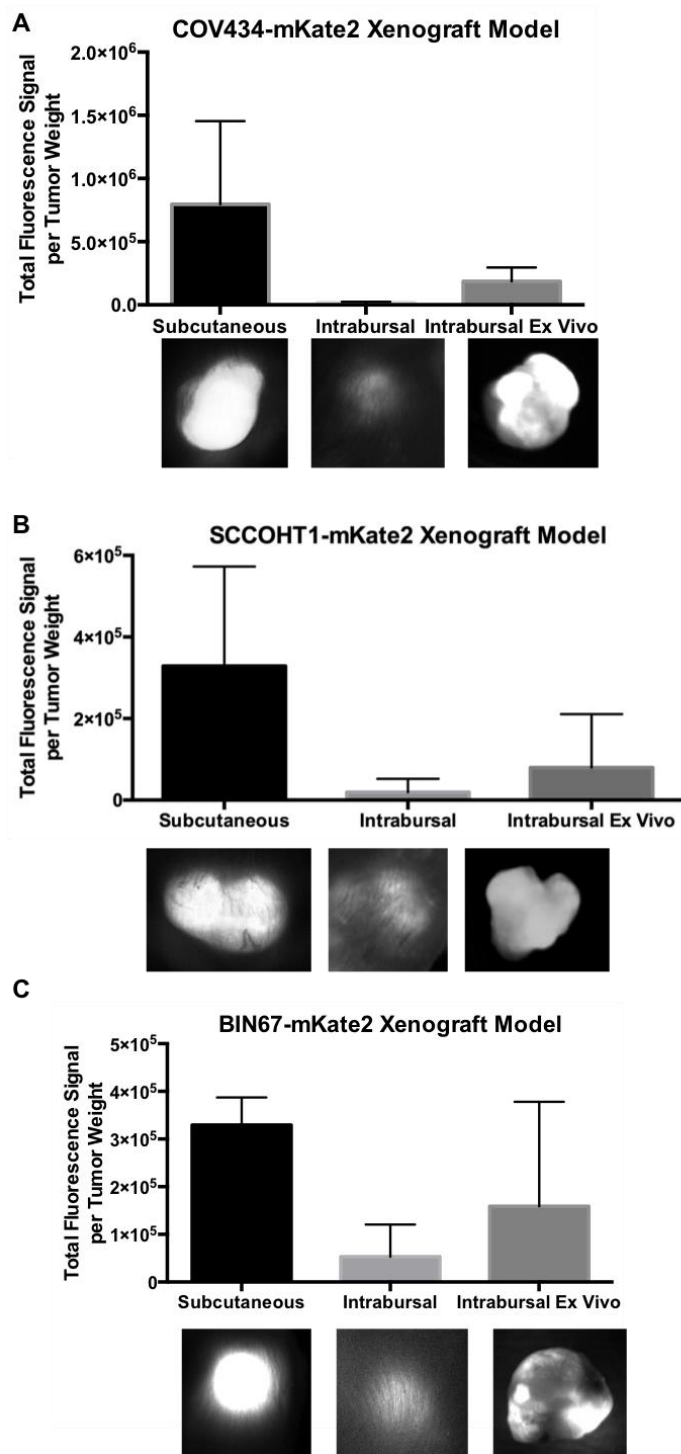


**Figure 3.8 Tissue attenuation in the fluorescence model.**

Fluorescence signals were normalized to tumor weight. Fluorescence signals were compared between subcutaneous model and intrabursal model in (A) COV434-mKate2, (B) SCCOHT1-mKate2 and (C) BIN67-mKate2.

### **3.2.6 Histological analysis between subcutaneous and intrabursal COV434-mKate2 xenograft model**

Tumors from each of the xenograft model development studies were formalin-fixed, paraffin-embedded and H&E stained. Tumors with similar tumor weight were selected for comparison. In COV434-mKate2 model, both subcutaneous (Figure 3.9 A) and intrabursal (Figure 3.9 E) model developed tumor with sheets of mixed population of small cells with hyperchromatic nuclei and large cells (Figure 3.9 B, C, F, G), which is the typical histologic features for SCCOHT. There was more necrosis as well as angiogenesis observed in the intrabursal model (40%) than subcutaneous model (20%) (Figure 3.9 C, F). Interestingly, multiple follicle-like structures were observed closer to the peritoneal lining of tumor in the intrabursal tumor stains, as indicated by the black arrow in Figure 3.9 G. Absence of BRG1 (SMARCA4) staining further confirmed the successful subcutaneous and intrabursal SCCOHT tumor development from COV434-mKate2 cells (Figure 3.9 D, I).

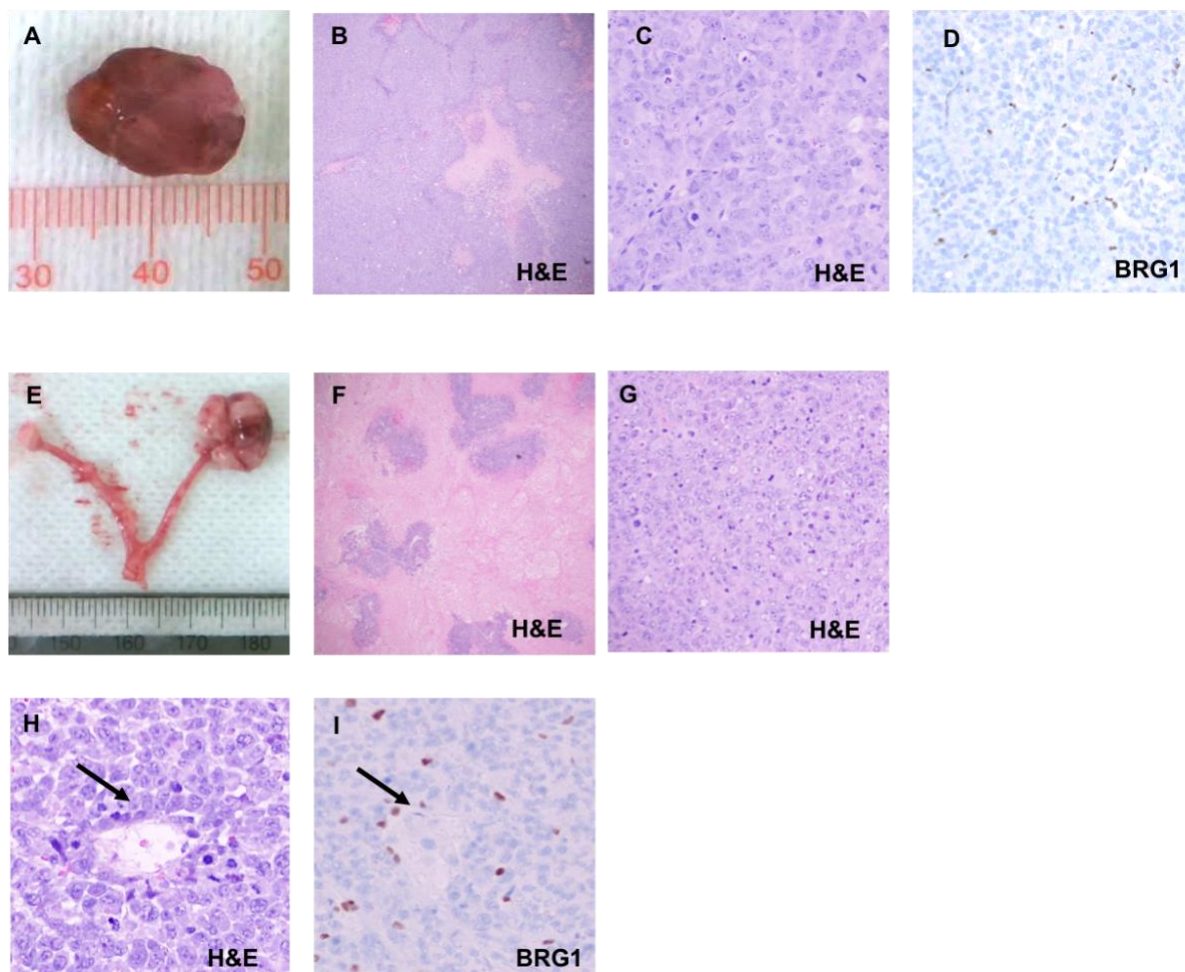


**Figure 3.9 Histological analysis in the COV434-mKate2 xenograft model.**

Tumors were fixed in formalin and embedded in paraffin at the end of the study and stained for H&E. Comparison between (A, B, C, D) subcutaneous model and (E, F, G, I) intrabursal model for COV434-mKate2 cells. Black arrow (G&H) shows a follicle-like structure. Original magnification: B and F x5; C, D and G x20; H and I x40.

Similar pathology was observed in SCCOHT1-mKate2 xenograft model. Both subcutaneous (Figure 3.10 A) and intrabursal tumor (Figure 3.10 E, I) contained high mitotic index, large cell variants and necrosis (Figure 3.10 B, F, J). Besides, subcutaneous tumor contains some rhabdoid signet ring cells (Figure 3.10 C) and intrabursal model present with microcapillary structure (Figure 3.10 F). Follicle like structures were also only present in the intrabursal tumor (Figure 3.10 G).

Interestingly, non-fluorescent intrabursal tumor were positive for BRG1 (SMARCA4) in the intrabursal model (Figure 3.10 E, F, G, H), whereas for fluorescent intrabursal tumor (Figure 3.10 I, J, K, L, M), half of the tumor was positive for BRG1 (Figure 3.10 L) and the other half was negative for BRG1 (Figure 3.10 M). For BRG1 positive non-fluorescent tumor (Figure 3.10 H) and the part of fluorescent tumor (Figure 3.10 L), its histological appearance featured similarities with contains some high-grade serous carcinoma, which typically present with branching papillary fronds, as shown in H&E staining in Figure 3.10 E). For BRG1 negative part of tumor (Figure 3.10 M), its morphology appears just as SCCOHT, sheets of high mitotic cells with presence of large cell variant.

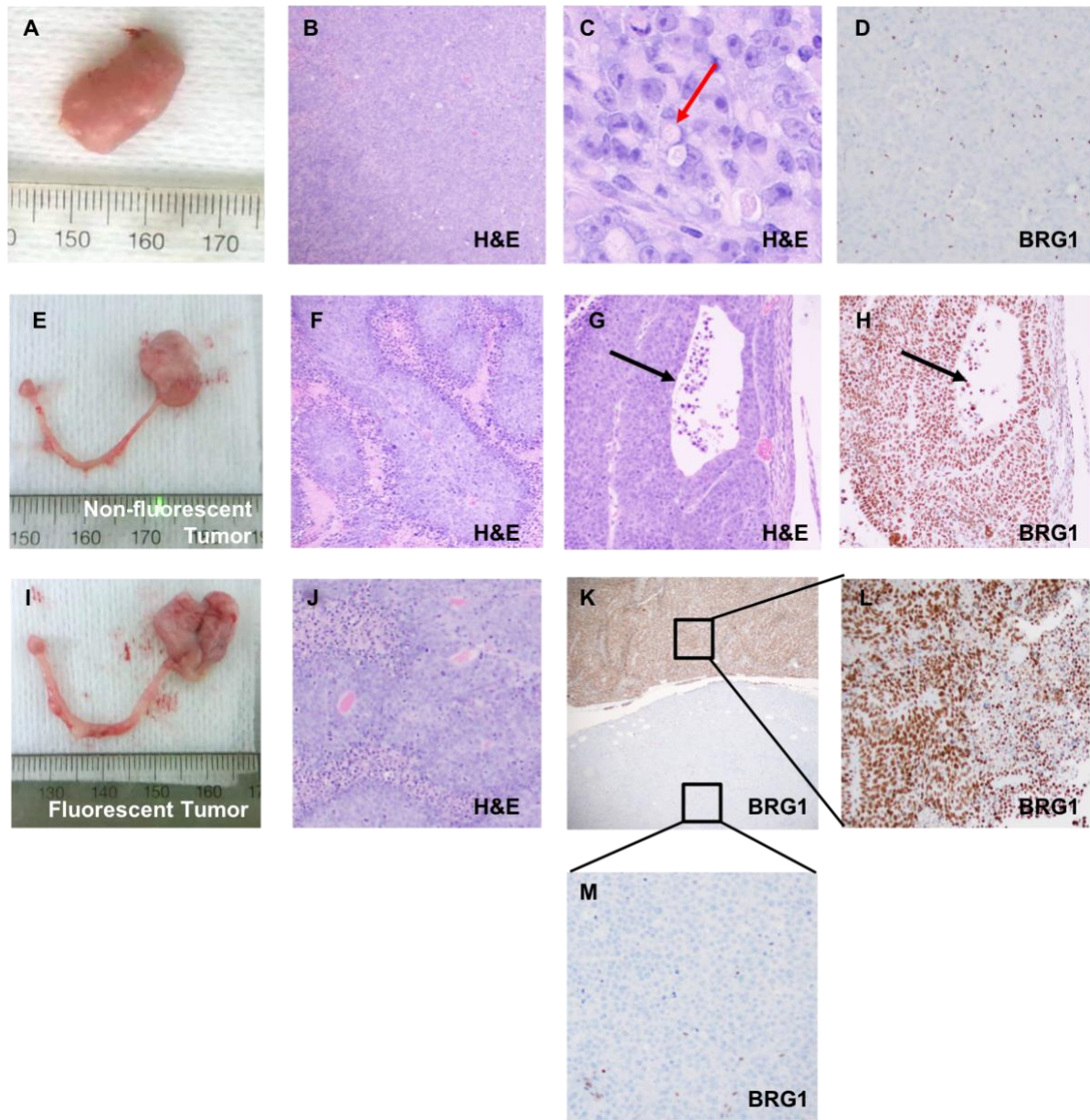


**Figure 3.10 Histological analysis in the SCCOHT1-mKate2 xenograft model.**

Tumors were fixed in formalin and embedded in paraffin at the end of the study and stained for H&E and IHC. Comparison between subcutaneous model (A, B, C, D) and intrabursal model in SCCOHT1-mKate2 xenograft from non-fluorescent tumor (E, F, G, H), and fluorescent tumor (I, J, K, L). Red arrow shows signet ring cell (C) and black arrow shows follicle-like structures (G&H). Original magnification: B, F and J x5; G and H x20; C, D, K and L x40.

In BIN67-mKate2 xenograft model, both subcutaneous (Figure 3.11 A) and intrabursal (Figure 3.11 E) tumors present typical SCCOHT pathology, such as high-grade nuclei feature, high mitotic index (Figure 3.11 B, F). Follicle like structures were also present in both subcutaneous and intrabursal model (Figure 3.11 C, G) and was negative for BRG1 (SMARCA4) stains (Figure 3.11 D, H). Unlike the other two cell line model, BIN67-mKate2 model had intratumoral adipose infiltration (Figure 3.11 C, E) in both subcutaneous and intrabursal tumors.

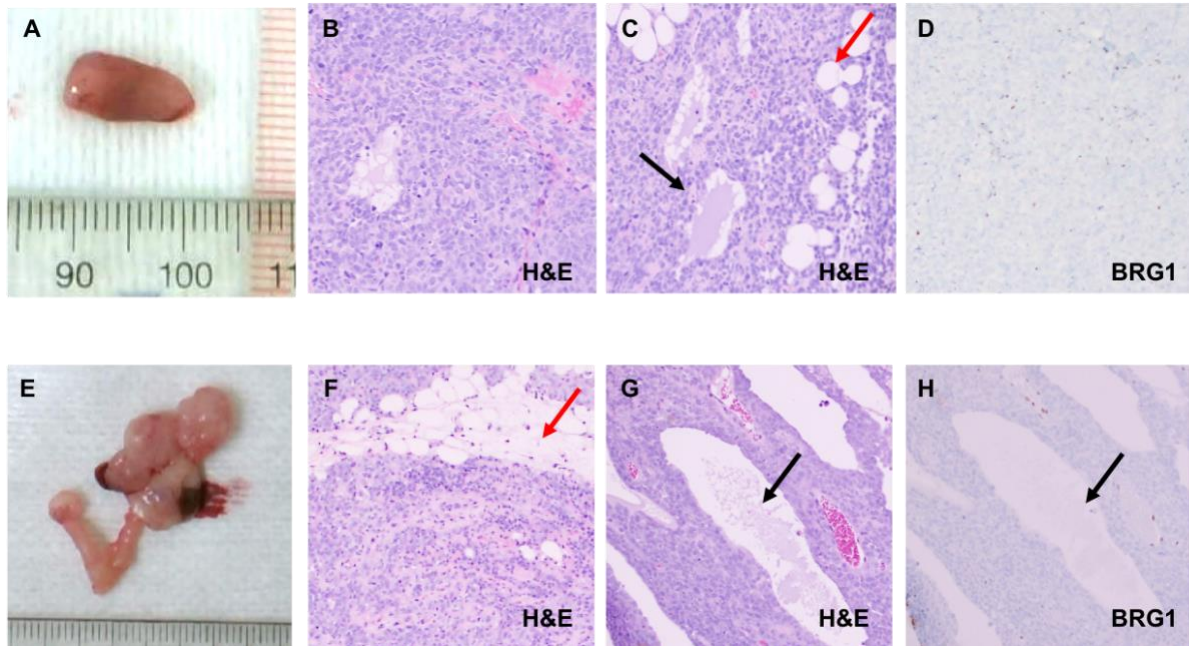


**Figure 3.11 Histological analysis in the BIN67-mKate2 xenograft model.**

Tumors were fixed in formalin and embedded in paraffin at the end of the study and stained for H&E and IHC. Comparison between (A, B, C, D) subcutaneous model and (E, F, G, H) intrabursal model for BIN67-mKate2 cells. Red arrows show adipose tissue (C&F) and black arrows indicate follicle-like structure (C, G, H). Original magnification: B, C, D and F x20; G and H, x40.

### 3.3 Discussion

As SCCOHT is a form of cancer with an extremely poor prognosis, there is an urgent need for developing targeted effective treatment options. Currently, all the SCCOHT preclinical studies are using subcutaneous xenograft models to predict the outcome for potential therapeutics. However, these models contain many drawbacks in terms of representation for SCCOHT. In this study, I have successfully established three mKate2-labelled SCCOHT cell lines. This far-red fluorescent protein, mKate2, has very neglectable effect *in vitro*, where all three SCCOHT cells with mKate2 expression show no significant difference in cell biological behavior, including morphology, cell proliferation and drug response, compared with parental cells.

The ability to form subcutaneous tumor for three SCCOHT cell lines was confirmed. Among these, fluorescent SCCOHT1 and COV434 subcutaneous tumors are developed within 3 weeks of inoculation and provided a total of two to three weeks of tumor progression window for testing the efficacy of anti-cancer drug candidates. In contrast, BIN67-mKate2 cells develop subcutaneous tumors 40 days post inoculation. The successful development of intrabursal models for SCCOHT1, BIN67 and COV434 cells confirms their tumor formation ability orthotopically. Unlike the subcutaneous xenograft model, ascites and abdominal tension were present in most of the intrabursal cases. In addition, metastasis was found for some mice bearing BIN67 intrabursal tumors. The histological analysis further indicates a more reliable representation of SCCOHT in the intrabursal model than subcutaneous model. Clinical features, such as follicle-like structure and angiogenesis are observed in all three intrabursal tumors.

Interestingly, SCCOHT1 subcutaneous tumor exhibited some rhabdoid like cells, which are not observed in any other models. And only tumors from BIN67 subcutaneous and intrabursal model present with intratumoral adipose infiltration.

Fluorescence signals from the subcutaneous model directly correlates with tumor volume, implying fluorescence signals from subcutaneous mKate2-labelled SCCOHT cells are reliable for future studies. COV434-mKate2 intrabursal model has further confirmed the stability of mKate2 signal and its potential application. With the aid of fluorescent signals, we can have better visualize the shape of the tumor as well as detect the presence of tumor earlier. As subcutaneous models can easily access the tumor volume, mice are always randomized when tumor volume reaches 100mm<sup>3</sup> prior to efficacy testing to avoid possible bias in tumor progression. However, the caliper measurements for small tumors are very subjective, especially when tumor is not round-shaped. Fluorescent signal, on the other hand, can correctly capture the tumor volume, which allows a more objective randomization in subcutaneous model.

The variation of fluorescence signals from BIN67 intrabursal model is likely due to the position of measuring the signal. As indicated in Figure 3.7 A, dorsal and ventral measurement for same mouse showed different signal intensity. The loss of signal could be caused by tissue attenuation. As mentioned earlier in this chapter, tissue attenuation was observed in all three models. Here, I assumed the tumor would grow towards dorsal side of the mouse. When tumor grew towards ventral side, some of the signals would be attenuated by the tissues surrounding it, leading to a drop in the signal.

Interestingly, in two of the intrabursal SCCOHT1 cases, signals are completely lost. Huge variation in signals are observed in this model, and tumor development are not as consistent as the other two cell lines. This implies a better fluorescence protein might be considered and conditions for intrabursal injections should be optimized.

IHC for BRG1 (SMARCA4) are performed to further confirm the identity of the tumors.

Unlike the other two cell lines, intrabursal SCCOHT1 tumors showed expression of SMARAC4. The expression of BRG1 is observed in the two non-fluorescent tumors, and half of the fluorescent tumor, which correlates with the loss of fluorescence signal. With BRG1 presence, fluorescence signals are absent. This could be caused by the following reasons. First, the cells injected intrabursally can be co-contaminated with other cell lines, as various cells are passaged at the same time. Cross-contaminated could happen during maintaining cell lines. As a result, after injected into mice, these non-SCCOHT1 cell could out-compete the growth of SCCOHT1 cell, and lead to loss of signals as well as expression of BRG1. This could also explain some features of high-grade serous ovarian cancer are present in SCCOHT1 intrabursal tumor.

Secondly, it could be caused by fusion of human DNA into mice DNA. Several groups have reported primary human tumor implantation can induce mouse tumor growth. Goldenberge and Pavia have observed two distant population of ovarian cancer, one of which have been proven to be murine, during tumor propagation in nude mice (126). However, this is not observed when passaging non-tumor human cells in mouse. Their findings imply the human cancer cells can induce malignancy in the host healthy cells. Later, Goldenberge *et al* used microarrays to show that human genes

remain functional in human-hamster hybrid tumors, and human tumors can merge their DNA with the host genome (127). In our case, the DNA from SCCOHT1 have emerged with recipient mouse genome and induce tumorigenesis in the nearby healthy mouse ovarian cells. This could be confirmed by single cell sequencing or to check the chromosome number in metaphase to differentiate the mouse cells from human cells.

To summarize, as shown in Table 3.1, the intrabursal xenograft model represents SCCOHT better than subcutaneous xenograft model. The challenging tumor monitoring for intrabursal model can be overcome by utilizing fluorescent bioimaging system. The fluorescent signal can be used as an early detection method as well as defining the location and shape of the tumor. To avoid the anesthetic complications caused by bioimaging, clinical monitoring of the mice, such as body weight changes, could be a reliable day-to-day method of the tumor development in the later stage of progression.

**Table 3.1 Summary of clinical and histological observation among different models.**

	Tension in abdominal	Ascites	Metastasis	Follicle-like structure	Necrosis	Hemorrhage	High mitotic index	SMARCA4 IHC
<b>Clinic</b>	Yes	Yes	Yes	Yes	Yes	Yes	Yes	95% Negative
<b>SC</b>	No	No	No	Only in BIN67	Yes	Little	Yes	Negative
<b>IB</b>	Yes	Yes	Yes	Yes	Yes	Yes	Yes	Negative*

# Chapter 4: Pharmaceutical inhibition of PRC2 complex in SCCOHT

## 4.1 Rationale and Specific Aims

The rare and deadly small cell carcinoma of the ovary, hypercalcemic type (SCCOHT) is the most common undifferentiated form of ovarian cancer in women under 40 years old (128). The prognosis of SCCOHT patients is poor even when diagnosed at early stages with the 5-year survival rate being 55% in patients with stage I disease (129). The high mortality associated with SCCOHT is largely due to its poor response to conventional chemotherapy and/or radiotherapy. No guidelines for optimal treatment are currently available, and there is an urgent need to develop biology-informed targeted therapeutics for SCCOHT.

In 2014, several labs around the world, including our lab, identified germline and somatic deleterious mutations in *SMARCA4* gene, which encodes BRG1, one of the two mutually exclusive ATPases of the SWI/SNF complex, in over 90% of the cases that leads to loss of SMARCA4 protein (27-30). No other recurrent genetic mutations were discovered, suggesting that SCCOHT would be a monogenic disease. Subsequent study from our lab and others found that SMARCA4-deficient SCCOHTs also lack the expression of SMARCA2 (32), the alternative ATPase of the SWI/SNF complex, indicating that SCCOHT is a SWI/SNF-deficient disease devoid of both ATPases of the SWI/SNF complex. The SWI/SNF complex utilizes energy from ATP hydrolysis to control gene accessibility through nucleosome mobilization, whereas polycomb

repressive complex 2 (PRC2) post-translationally modifies N-terminal of histone H3 K27 residue, which act as a binding site for polycomb repressive complex 1 (PRC1) to monoubiquitylate histone 2A on Lys 119 and initiate a block to transcription as well as create a compacted chromatin (130). As SWI/SNF complex and the PRC2 oppose each other to regulate gene expression in various cancer types, including SWI/SNF-defective cancers such as SMARCB1-deficient malignant rhabdoid tumors (MRTs), ARID1A-deficient ovarian clear cell carcinomas, SMARCA4-deficient lung cancers, and PBRM1-deficient renal cancers (64, 92, 131), I aimed to address whether targeting the activity of PRC2 is a feasible strategy for treating SMARCA4/SMARCA2-defective SCCOHT.

The objective of this chapter is to determine the therapeutic potential of targeting PRC2 in SCCOHT cells *in vitro* and evaluate the *in vivo* efficacy using the SCCOHT fluorescent xenograft models established in Chapter 3. The specific aims include:

Aim1. Determine whether SCCOHT cells are sensitive to PRC2 subunit depletion

Aim2. Evaluate the effect of EED inhibitor to SCCOHT cell lines and EZH2i-resistant cell lines

Aim 3. To determine the toxicity of EED226 in NRG mice

Aim 4. To investigate the efficacy of EED226 in a SCCOHT xenograft model.

## 4.2 Result

### 4.2.1 SCCOHT cells are sensitive to depletion of EZH2

The antagonism between the SWI/SNF complex and PRC2 implies the important role of PRC2 in SCCOHT tumorigenesis. To exploit whether SCCOHT relies on EZH2, the catalytic subunit of PRC2, for proliferation, we employed two specific shRNAs to deplete the expression of EZH2. As shown in Figure 4.1 A, both EZH2 shRNAs depleted EZH2 efficiently 72 hours post virus infection. The global trimethylation levels of histone H3 lysine 27 (H3K27me<sub>3</sub>), the target of PRC2, were also significantly decreased implying the loss of EZH2 activity (Figure 4.1 A). Knockdown of EZH2 significantly inhibited the proliferation of SCCOHT cells (BIN67, SCCOHT1 and COV434), with SCCOHT1 cells being the most affected. Taken together, knockdown of EZH2 subunit of PRC2 affects the growth of SCCOHT cell lines.

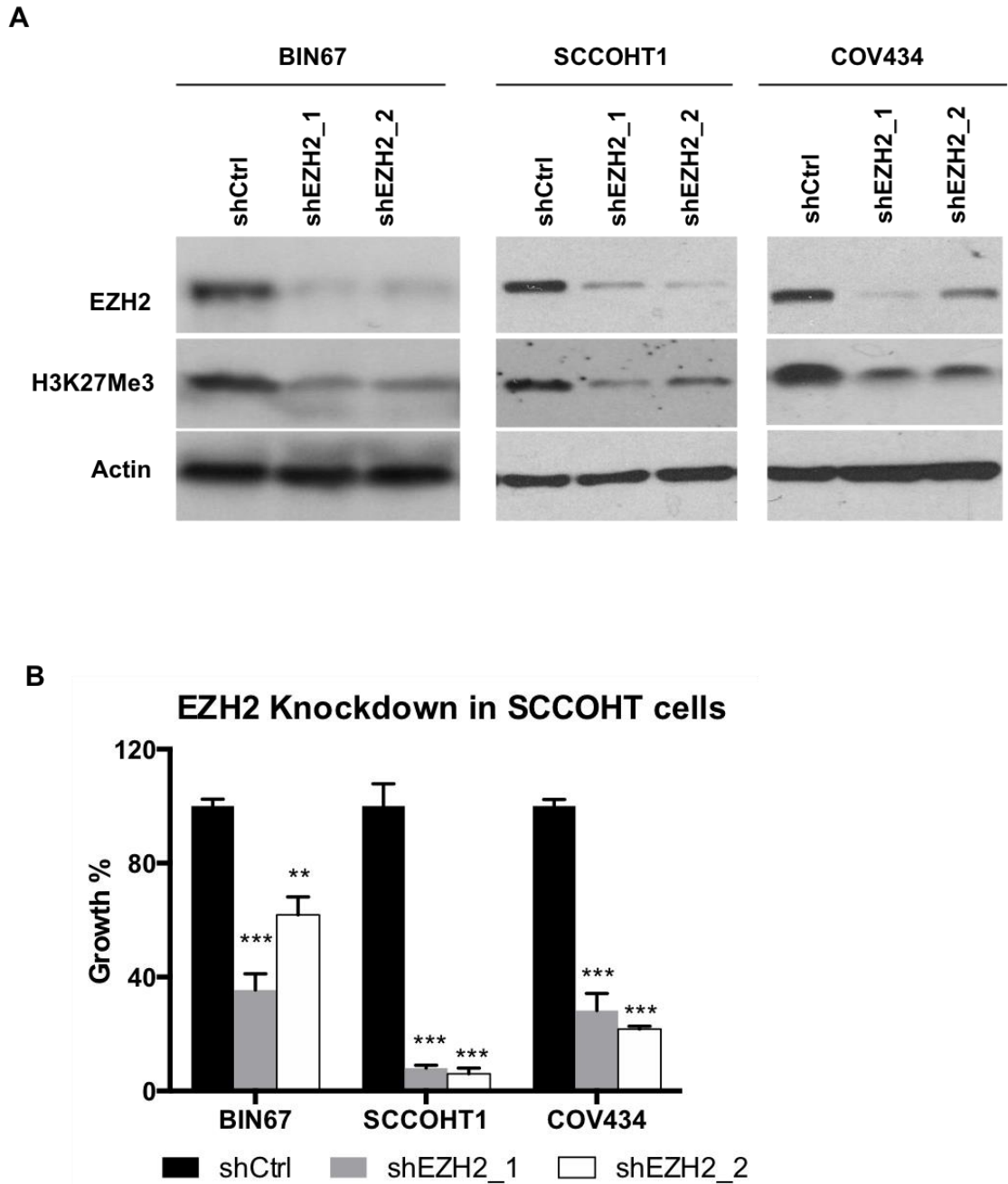


**Figure 4.1 SCCOHT cells are sensitive to EZH2 depletion.**

Cells were infected with lentivirus expression either control (shCtrl) or EZH2 shRNA. After 48-hour puromycin selection, cells were (A) reseeded in 24-well plates for 6 days and quantitated by crystal violet staining assay, and (B) harvested for western blot analysis.

## **4.2.2 SCCOHT cells are sensitive to inhibition of PRC2 catalytic activity**

### **4.2.2.1 SCCOHT cells are sensitive to pharmaceutical inhibition of EZH2**

Next, I determined whether catalytic inhibition of EZH2 had any effects on growth of SCCOHT cells. GSK126, a selective inhibitor of EZH2 that is currently being tested in clinical trials, was employed for *in vitro* studies, as it was already in clinical trials.

GSK126 acts as a competitor with S-adenosyl-L-methionine (SAM), a co-substrate for PRC2, for binding to SET domain of EZH2 to de-activate its catalytic activity (63).

GSK126 potently suppressed histone H3K27me3 level (Figure 4.2 A). In 9-day drug response assays, all SCCOHT cell lines were more sensitive towards GSK126 than the other ovarian cancer cells tested (Figure 4.2 B). Among the three SCCOHT cell lines, the IC<sub>50</sub> for SCCOHT1 cells were five- or ten-fold more sensitive than BIN67 and COV434 in response to GSK126, respectively. When comparing IC<sub>50</sub> among all the cell lines tested, SCCOHT had significantly lower IC<sub>50</sub> than the various epithelial ovarian cancer cells.

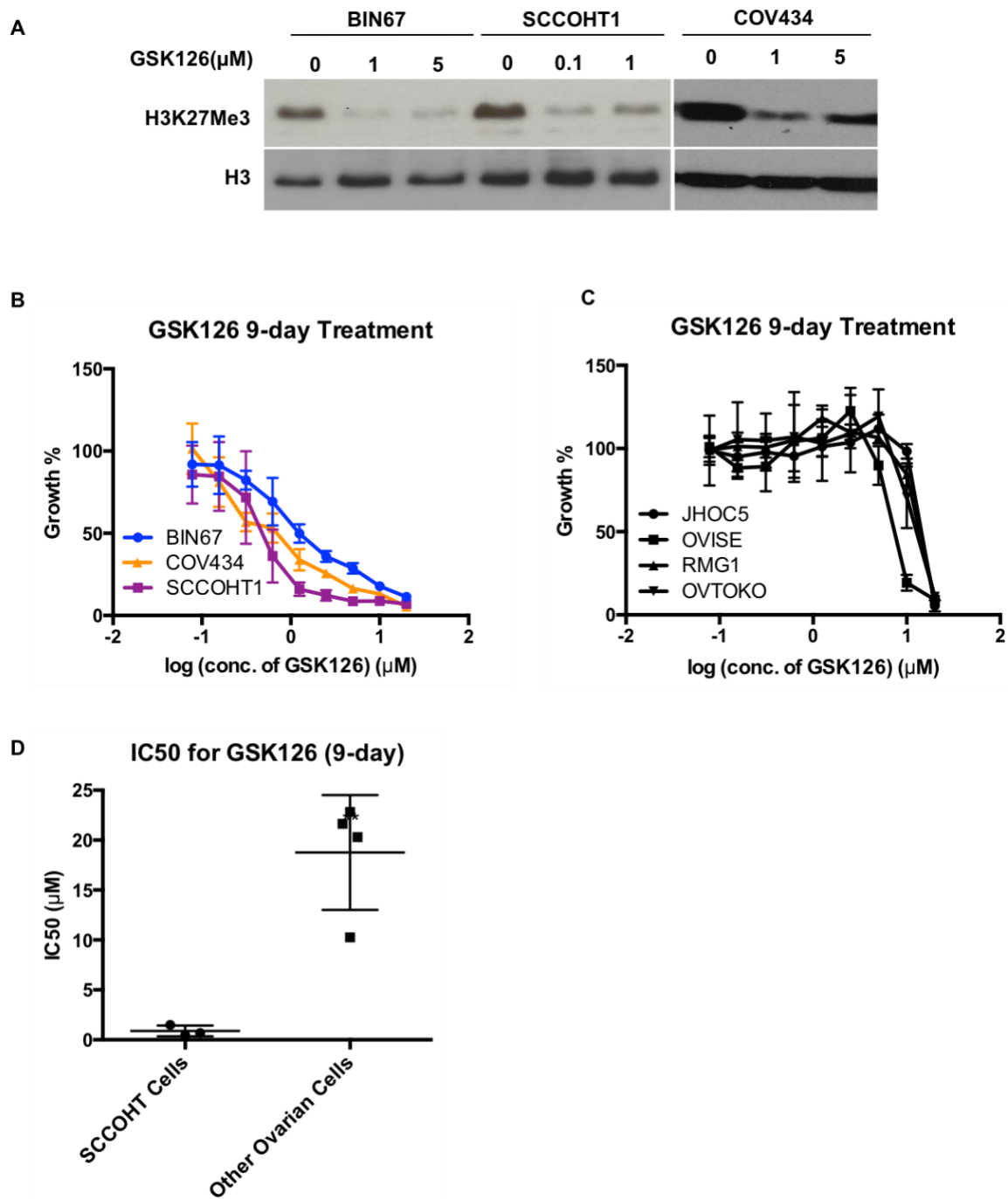


**Figure 4.2 SCCOHT cells are sensitive to pharmaceutical inhibition of EZH2.**

A) Cells were seeded and treated with GSK126 for 3 day and harvested for western blot analysis. (B) Cells were seeded in 96-well plates and treated with various concentration of GSK126, by serial dilution. (C, D) Cells were fixed and stained with crystal violet at the end of 6<sup>th</sup> day of treatment for quantitation.

#### 4.2.2.2 **SCCOHT cells are sensitive to pharmaceutical inhibition of EED subunit**

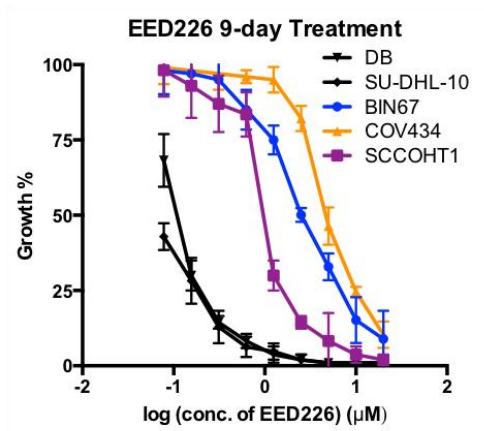
Besides targeting the catalytic subunit, recent studies have demonstrated that the activity of PRC2 can be effectively suppressed through allosteric targeting of its EED subunit. Two groups, Qi *et al* and He *et al*, have independently developed two EED inhibitors, EED226 and A-395, in early 2017 (82, 83). Both inhibitors bind to EED in the H3K27me3-binding pocket to induce conformational changes, and ultimately leads to suppression of PRC2 catalytic activity. I picked EED226 for both *in vitro* and *in vivo* testing, as it is commercially available.

In 9-day assays, SCCOHT cells displayed great sensitivity to EED226 (Sellekchem) with  $IC_{50}$  being 2.74  $\mu$ M, 1.00  $\mu$ M, 4.60  $\mu$ M for BIN67, SCCOHT1 and COV434, respectively, while none of the other ovarian cancer cells tested responded to EED226 treatment (Figure 4.3 A, B). Although other ovarian cancer cell lines are not responsive to EED226, the global histone H3K27me3 levels were reduced upon EED226 treatment (Figure 4.3 C). Two lymphoma cell lines with active EZH2 mutations, DB and SU-DHL-10, were included in the 9-day assay as positive controls. DB, which was potently suppressed by EED226 in Qi's study in a 14-day assay (83), was robustly suppressed by EED226 with  $IC_{50}$  being 0.090  $\mu$ M (Figure 4.3 A). Similar response was observed in the other lymphoma cell line, SU-DHL-10 ( $IC_{50}$  = 0.056  $\mu$ M) (Figure 4.3 A). Furthermore, EED226 from a different vendor (MedChem), which was later used for *in vivo* studies, displayed comparable effects on both growth suppression and H3K27me3

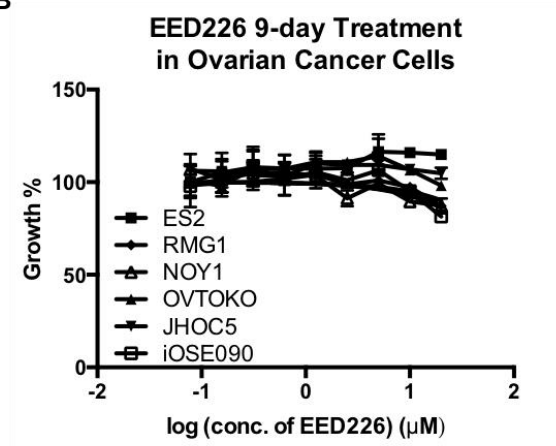
in SCCOHT cells as that from Sellekchem (Figure 4.3 D), indicating that EED226 from these two different sources shares equivalent potency.

To determine whether SWI/SNF-defective cells are generally sensitive to EED inhibition, a panel of SWI/SNF-defective cell lines, including two rhabdoid cell lines (A204 and G401), four lung cancer cell lines (A549, H23, H522 and H1703) and one sarcoma cell line (VA-ES-BJ), were tested for their response to EED226 (Figure 4.3 E). Two SMARCB1-deficient rhabdoid cells lines, G401 and A204, and one SMARCB1-deficient lung cancer cell lines, H1703, were sensitive to EED226, with IC<sub>50</sub> of 1.27 μM, 2.1 μM and 4.41 μM respectively. The remaining SWI/SNF-defective cell lines were unresponsive to EED226 in the concentration range tested. Despite sensitivity, cells treated with EED226 at 3 μM had inhibition of PRC2 catalytic activity, as shown by decrease in global histone H3K27me3 (Figure 4.3 C, G). Overall, SCCOHT had a significantly lower IC<sub>50</sub> for EED inhibition than most of the SWI/SNF-defective cell lines and other ovarian cancer cells tested (Figure 4.3 H).

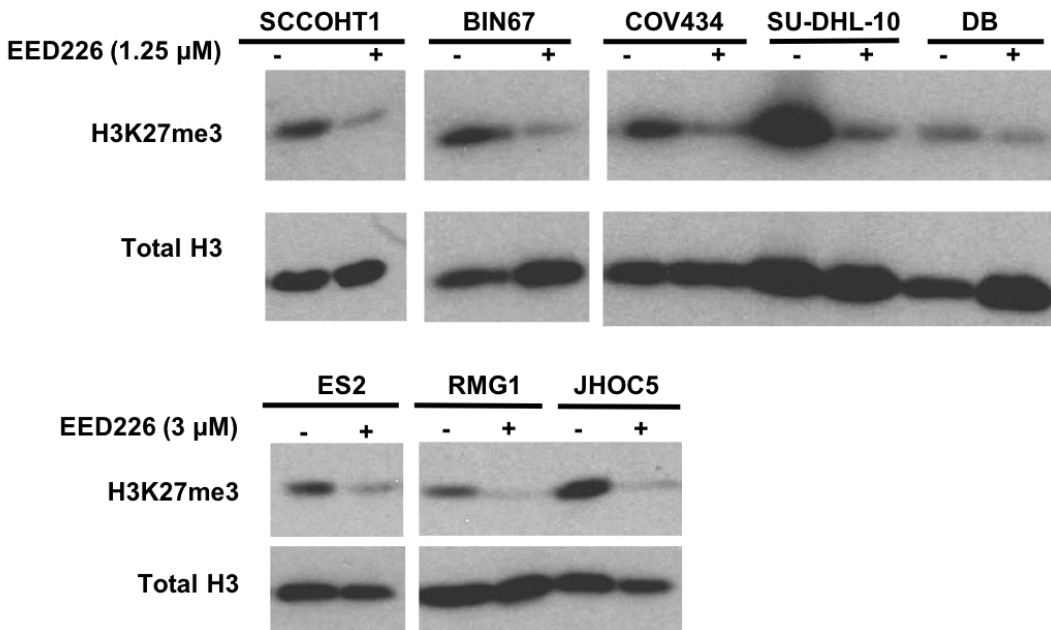
A



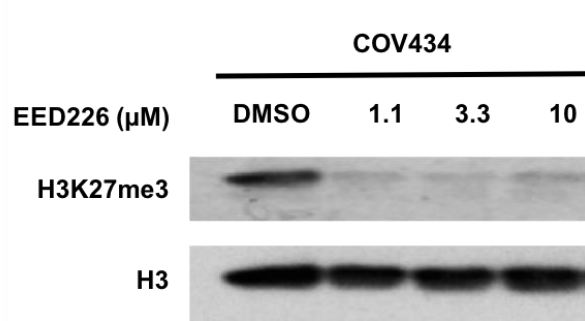
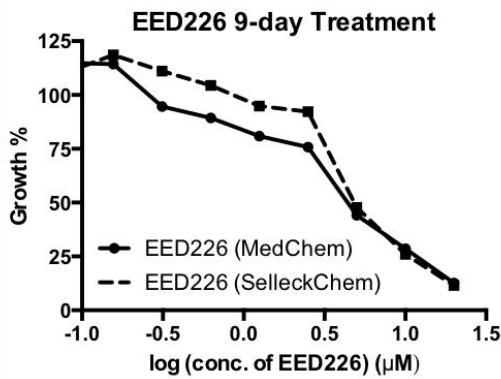
B



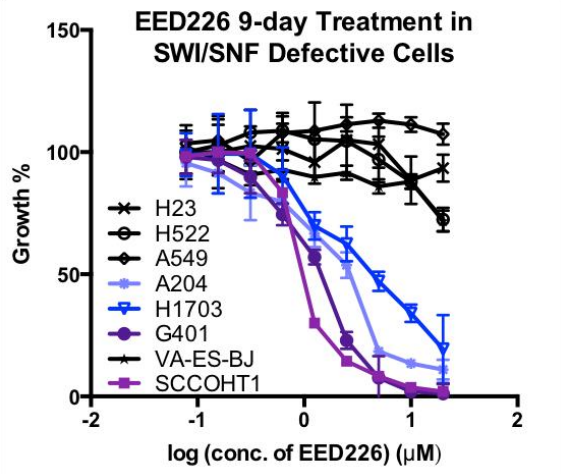
C



D



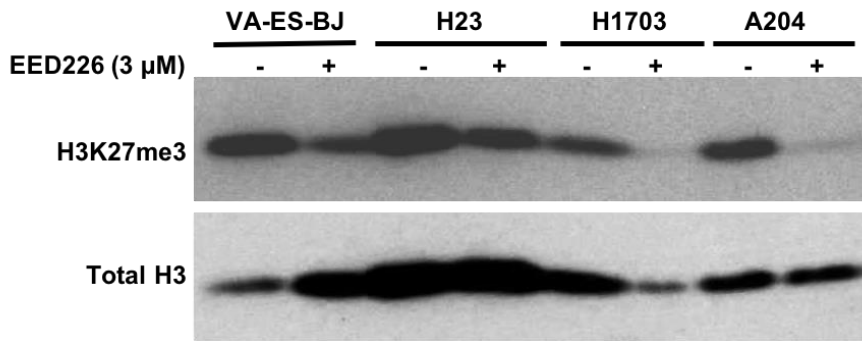
E



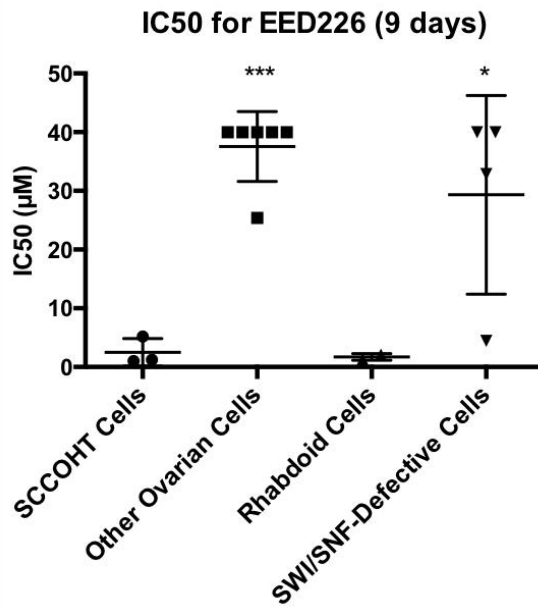
F

Cell Line	Tumor Type	Mutation
A204	Rhabdoid	SMARCB1
G401	Rhabdoid	SMARCB1
A549	Lung	SMARCA4
H23	Lung	SMARCA4
H522	Lung	SMARCA4 SMARCA2
H1703	Lung	SMARCA4
VA-ES-BJ	Sarcoma	SMARCB1

G



H



I

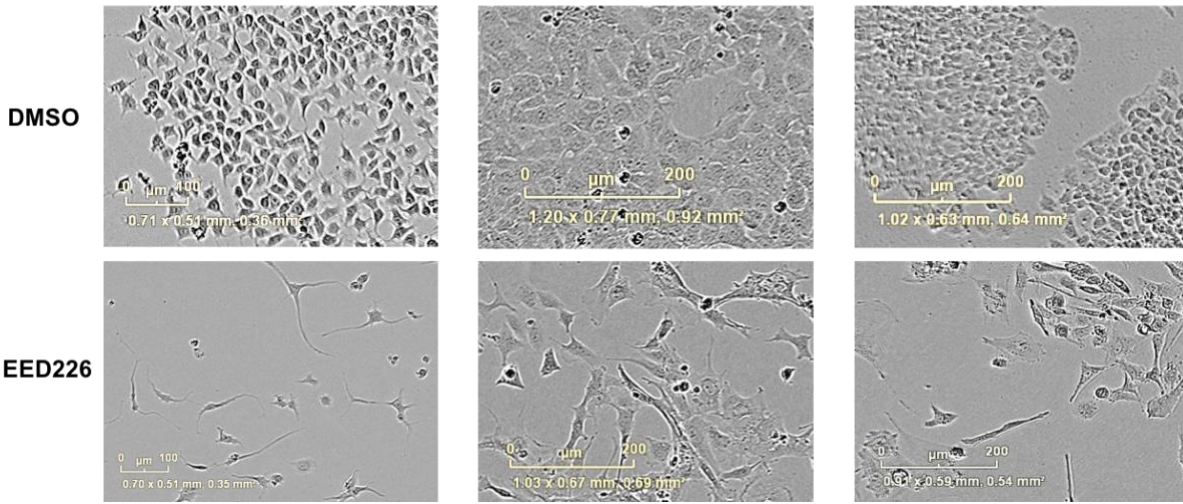


**Figure 4.3 SCCOHT cells are sensitive to EED inhibition.**

Cells were seeded in 96-well plates and treated with various concentration of EED226, by serial dilution, and monitored by Incucyte in SCCOHT cells (A), other ovarian cancer cells (B), and SWI/SNF defective cells (E, F). Summary of  $IC_{50}$  for all the cells tested (H). Cells were treated with EED226 for 3 days, and harvested for western blot analysis (C, D, G). Photos of EED226 treated SCCOHT cells (I).

#### 4.2.2.3 Sensitivity of GSK126-resistant cells to EED226

Several EZH2 inhibitors are being tested in the multiple clinical trials (80, 81, 84, 87). Encouraging signs of efficacy have emerged in the clinic. One of the clinical challenges of effective chemotherapies is acquired treatment resistance. To test whether GSK126 resistant cells are still sensitive to EED226, I tested the response to EED226 in COV434<sup>EGR</sup> cell line, a GSK126 resistant cell line derived from COV434 through prolonged exposure to GSK126 in our lab (Wang et al, unpublished data). COV434<sup>EGR</sup> cells are resistant to the treatment of 10  $\mu$ M GSK126, but were not sensitive to EED226, with IC<sub>50</sub> at 14.62  $\mu$ M (Figure 4.4 B). Its histone H3K27me3 level was also decreased upon 3-day exposure to EED226 treatment (Figure 4.4 C).

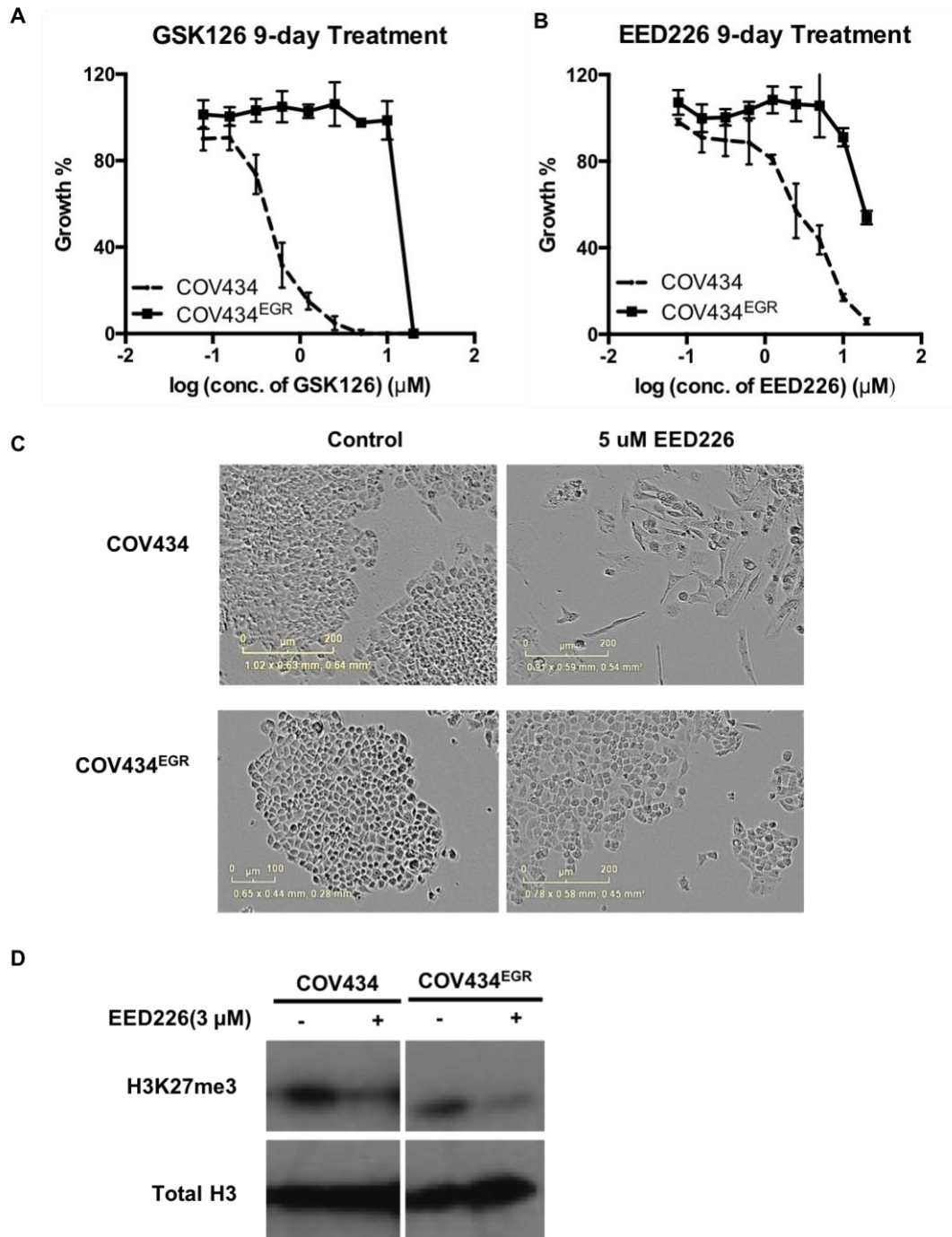


**Figure 4.4 Sensitivity of GSK126- resistant cells to EED226.**

(A, B, C) Cells were seeded in 96-well plates and treated with various concentration of GSK126 or EED226, by serial dilution for 6 or 9 days respectively. Cells were fixed at the end of the 6<sup>th</sup> or 9<sup>th</sup> day treatment and stained with crystal violet for cell survival. (D) Cells were treated with EED226 for 3 days and harvested for western blot analysis.

### 4.2.3 *In vivo* efficacy of EED226 on SCCOHT xenograft tumors

#### 4.2.3.1 40mg/kg EED226 (PO BID) had minimal toxicity effect in tumor-free NRG mice

Before testing the anti-tumor effect of EED226, a safe dosage range was determined to ensure the ethics of animal studies. According to Qi's publication, 4 mg/kg of EED226 delayed the tumor growth after 21 days of dosing and reached stasis after 30 days of dosing in a Karpas422 xenograft model. Based on this finding, I tested two dosage 10 mg/kg and 40 mg/kg in our tumor-free female NRG mice, with dosing schedule of twice daily for two and half consecutive weeks with one day break between each week (PO BID M-Sat). As shown in Figure 4.5, 40 mg/kg EED226 twice daily dosing orally for 18 days has minimal effects on mice, as indicated by the limited effects on body weight and absence of adverse effects such as reduced activities or food consumption.

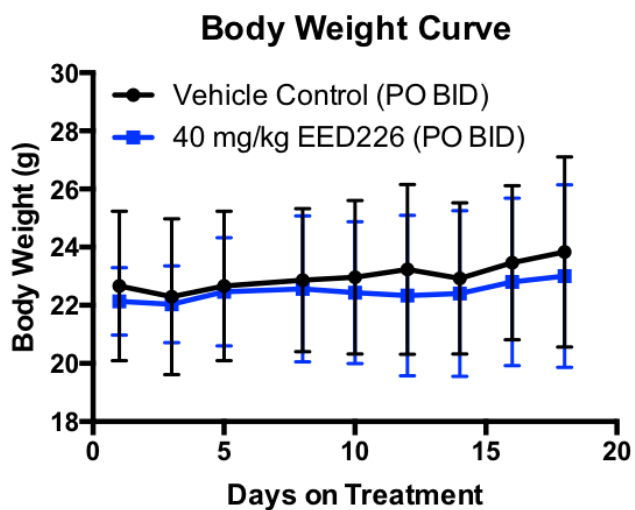
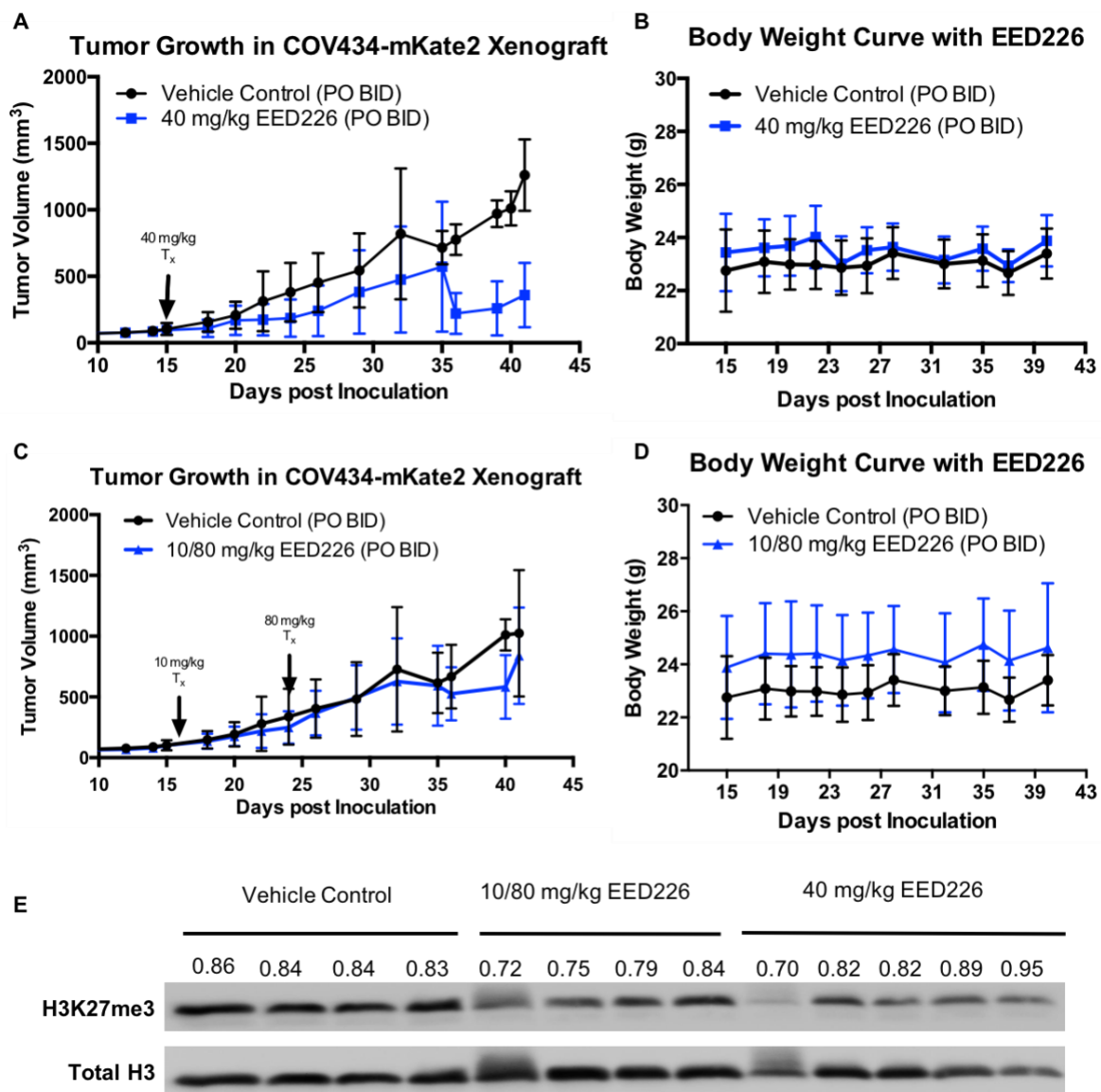


Figure 4.5 EED226 had mild effect in tumor-free NRG mice.

Effect of 40 mg/kg EED226 on body weight of tumor-free NRG animals (n=8; mean $\pm$ SD).

#### **4.2.3.2 80 mg/kg EED226 (PO BID) had minimal toxicity effect and very mild anti-tumor effect in the COV434-mKate2 subcutaneous xenograft model**

Based on the toxicity studies, I conducted the efficacy study for EED226 with two treatment arms: 10 mg/kg and 40 mg/kg. After one-week dosing (PO BID M-Sat), the tumor progression in 40 mg/kg group did not slow down, so I increased the 10 mg/kg to 80 mg/kg and use this group as a toxicity testing group in tumor-bearing mice. Following by another three weeks of dosing (PO BID M-Sun), none of the treated group show any significant delay in tumor progression (Figure 4.6 A, C). Tumor-bearing animals treated with 80 mg/kg showed no significant decrease of body weight (Figure 4.6 D). The histone H3K27me3 level was also checked in both treated groups. Even the 80 mg/kg EED226 group showed very mild effect on the drug target, histone H3K27me3 (Figure 4.6 E), implying that the treatment at this dosage was not sufficient to suppress EZH2 activity allosterically in COV434 cell-derived xenograft tumors.



**Figure 4.6 EED226 had mild effect in the COV434-mKate2 subcutaneous xenograft model.**

(A, C) Growth curve of subcutaneous COV434-mKate2 xenograft tumors in mice treated with EED226 through oral administration (PO) twice daily (BID) six days a week for three weeks (n=8; mean±SD). (B, D) Effect of twice daily oral administration EED226 on body weight of tumor-bearing NRG animals. (E) Inhibition of H3K27me3 in EED226-treated tumor.

#### **4.2.3.3 200 mg/kg EED226 inhibited SCCOHT1-mKate2 xenograft tumor growth**

As SCCOHT-1 cells were more sensitive to EED226 *in vitro*, with the IC<sub>50</sub> 5-fold lower than COV434 cells, SCCOHT1-mKate2 cells-derived subcutaneous xenografts were then used for a pilot study to test the toxicity and anti-tumor effect at the same time. One treatment arm, 200 mg/kg EED226, was included in this pilot study, and each arm had 3 mice. Two and half weeks of twice daily continuous dosing (PO BID M-Sun) of EED226 at 200 mg/kg significantly slowed down the growth of xenografted tumors (Figure 4.7 A) and had very mild effect on mice body weight (Figure 4.7 B), but mice appeared in pain in both the control and the treatment group. After mice were terminated, necropsy was performed, but no sign of abnormality was observed, implying the pain was likely due to the twice daily dosing rather than the drug or vehicle itself.

Fluorescence signal was also captured once a week during the study. Fluorescence signal was captured six days post treatment (22 days post inoculation) and before the end of the study. Signals for treated group was only significantly lowered than the control group on day 22 but not at the end of study. The average tumor weight dropped by ~70% in 200 mg/kg EED226 group compared with the vehicle control group at the end of two weeks (Figure 4.7 D). Western blotting analysis of tumor lysates demonstrated that the histone H3K27me3 level was significantly decreased in tumors harvested from EED226 treated mice, implying 200 mg/kg EED226 can effectively hit the target in xenograft model (Figure 4.7 E).

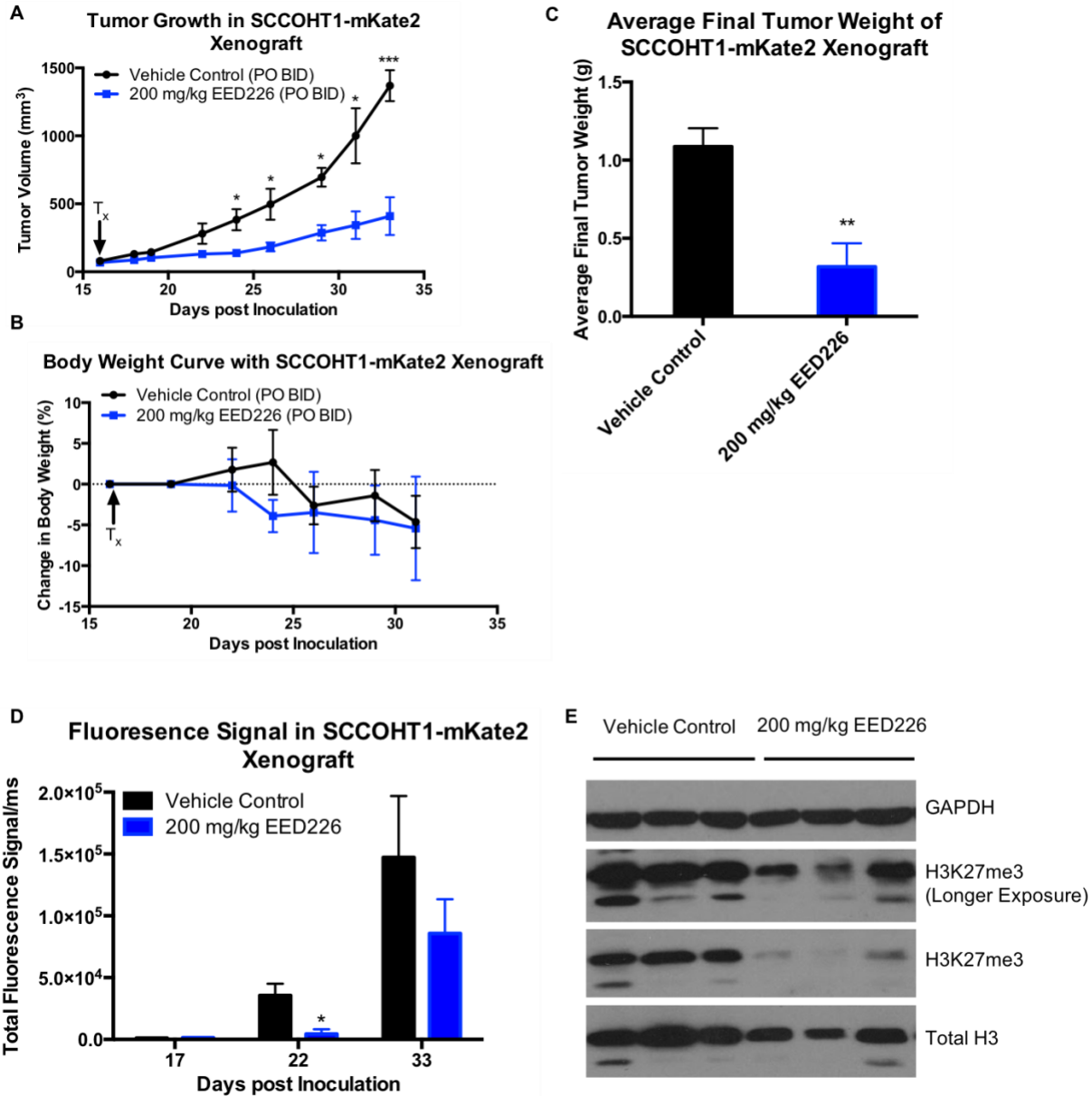


**Figure 4.7 EED226 had some effect in SCCOHT1-mKate2 subcutaneous xenograft model.**

(A) Growth curve of subcutaneous SCCOHT1-mKate2 xenograft tumors in mice treated with EED226 through oral administration (PO) twice daily (BID) for two and half weeks (n=3; mean±SD). (B) Effect of twice daily oral administration EED226 on body weight of tumor-bearing NRG animals. (C) Fluorescence signal was measured once a week throughout the treatment course. (D) Tumors were weighed and harvested at the end of two-week study. (E) Level of global histone H3K27me3 was measured in EED226-treated tumor by Western Blot.

### 4.3 Discussion

Transformation to cancer cells requires acquisition of characteristic hallmarks, such as survival and proliferation, even under counteracting signals(132). These events require changes to the fine-tuned balance of the normal cell homeostasis, which can lead to deregulation of oncogenes and tumor suppressor through cellular signaling network. Epigenetic alterations have been widely studied and implicated in oncogenesis. For instance, it is known that overexpression of EZH2, the catalytic subunit of PRC2, can lead to a repressed epigenetic state that has been observed in several types of cancer (78, 79). In contrast, other cancer types show genetic loss of EZH2 (75-77). Collectively, disturbing the balance of homeostasis, in a given cellular context, in either direction can lead to oncogenesis. Many studies have shown PRC2 and SWI/SNF complexes can serve antagonistic roles in tumorigenesis. In this chapter, I have shown that SWI/SNF-deficient SCCOHT cells are more sensitive to allosteric inhibition (i.e. EED226) and catalytic inhibitor (*i.e.* GSK126) of PRC2 than the other ovarian cancer cells. I have also demonstrated that 200 mg/kg EED226 can delay tumor progression in SCCOHT1 xenograft model, with mild effect on body weight or activity level. This study, together with our previous finding that both GSK126 and EPZ-6438, another catalytic inhibitor of EZH2 were effective in suppressing SCCOHT xenograft tumor growth, implies that SMARCA4/SMARCA2 dual deficient SCCOHT depends on catalytic activity of EZH2 to drive epigenetic modification and oncogenic transformation and pharmaceutical inhibition of EZH2 catalytic activity may serve as a putative therapeutic option for treating SCCOHT patients (123).

To better understand the dependency of PRC2 in SWI/SNF defective SCCOHT, I investigated the role of epigenetic activity of PRC2 in a cell line model. Our lab has previously shown that ablation of EZH2 in epithelial ovarian cancer cells, including ARID1A-deficient OVISE, slowed down their proliferation (123), yet catalytic inhibition of EZH2 had minimal effect on their proliferation (Figure 4.2 B), which is supported by our studies using another EZH2 catalytic inhibitor, EPZ-6438 (123). This difference is not due to the differential effects of catalytic inhibition of PRC2 because inhibition of either EZH2 or EED subunit led to dramatic decrease in histone H3K27me3 in all cell lines. These data suggest that depletion of EZH2 suppresses growth of both SCCOHT and other ovarian cancer cells, but inhibition of the methyltransferase activity of PRC2, either catalytically or allosterically, are effective specifically to SCCOHT cells.

Several studies have reported the antagonism between SWI/SNF complex and PRC2, after first observation in *Drosophila* (54). A panel of different SWI/SNF-defective cell lines were tested for EED226 sensitivity. The growth of two rhabdoid tumor cell lines, G401 and A204 that lose the expression SMARCB1, core component of SWI/SNF complex, were robustly suppressed by EED inhibition with a comparable IC<sub>50</sub> with SCCOHT cell lines. G401 were also responded similarly towards EZH2 inhibitor, EPZ-6438 (123). The morphological similarities, comparable dependence on PRC2 activity, and common genomic features (i.e. SWI/SNF deficiency and extremely low mutation burden) support that MRT and SCCOHT may share similar cell of origin (42). Accordingly, when SCCOHT cells were exposed to either EZH2 inhibitor or EED inhibitor, cells displayed neuron-like morphology (Figure 4.3 I), but this morphology changes were not observed when treating SCCOHT cells with cytotoxic reagents, such

as cisplatin, etoposide, and paclitaxel (123). A similar morphology change has also been reported by Knutson *et al* (133) when treating with EPZ-6438. Signet ring cells, the typical feature of MRT, were also observed in the tumors from the SCCOHT xenograft model discussed in Chapter 3. More studies need to be performed to explore the cell of origin for SCCOHT, but it might arise from very similar cell type as MRT.

In contrast, most other SWI/SNF-defective cell lines tested were non-responsive. Unlike SCCOHT cells, H522 cells, a lung cancer cell line with dual loss of SMARCA4 and SMARCA2, did not respond to EED226 in a 9-day drug assay. Similar drug response trend was also observed when treating with SWI/SNF-defective cell lines with EZH2 inhibitor, EPZ-6438 (123). Besides cell lines with deficiency in the core subunit, SMARCB1 or the ATPase component (SMARCA4 or SMARCA2), two ARID1A-defective ovarian cancer cell lines (OVTOKO and OVISE) showed no responses towards both EED and EZH2 inhibitors. Unlike monogenic SCCOHT, SWI/SNF-defective lung cancer cells and ARID1A-deficient ovarian cancer cells have many other mutations, such as EGFR, KRAS, and BRCA that acts together to drive oncogenesis. A different disease mechanism makes these cell lines less dependent on PRC2 activity, despite similar perturbation leading to defective SWI/SNF as SCCOHT.

In the pilot *in vivo* efficacy studies, I evaluated the efficacy of EED226 at doses between 40-200 mg/kg BID daily. Unlike in Qi's paper, where the growth of lymphoma xenograft tumor was strongly suppressed to 4mg/kg EED226 (83), only at a dose of 200mg/kg EED226 was able to significantly repress the growth of SCCOHT1 xenograft. This difference may reflect the differential sensitivity of SCCOHT cells and lymphoma

cells that usually carry active EZH2 activating mutations. In fact, the IC<sub>50</sub>s of EED226 in the lymphoma cell lines used in Qi study were at least 10-fold lower than those of SCCOHT1 cells.

In addition to the reduced tumor size, the fluorescence signal in the SCCOHT1 xenograft was reduced by EED226 treatment in both time points (6 days post treatment and end of study). However, the reduction was significant only at the day 6 post treatment, but not on the last day of the study. This could be caused by large tumor volume in the treated group at the end of the study, which contained large area of necrosis leading to loss of fluorescence signal. Although we cannot solely rely on fluorescent signals to monitor the tumor growth, it can be utilized as a useful tool for early detection of tumor and monitor the dimensions of the tumor to eliminate bias measurement by using caliper.

To better predict the clinic outcome for chemotherapies, researchers have established different models to predict the potential drug resistance (134). Most EZH2 inhibitors in clinical trials now are similar-structured and target SET domain of EZH2. Baker *et al* (134) and Gibaja *et al* (135) have illustrated one single point mutation can confer drug resistance to EZH2 inhibitors, implying the high likelihood of developing drug resistance in clinic. Targeting the methyltransferase activity is still feasible, but beyond binding competition at the SET domain should be considered. EED inhibitor, EED226, binds to the binding pocket and ultimately inhibits H3K27 methylation. Qi *et al* has reported that WSU-DLCL2, a lymphoma cell line with activating EZH2 mutation, can acquire resistance to EZH2 inhibitor EPZ-6438 at 10 $\mu$ M through point mutations of

EZH2 at Y641F (83). This EPZ-6438-resistant cell line remained as sensitive as the parental cell line to EED226 (83). Here, although EED226 can effectively suppress H3K27Me3 in both COV434 and COV434-EGR cells, a GSK126 resistant cell line that was developed by our lab through stepwise exposure to GSK126, were resistant to up to 10 $\mu$ M GSK126, COV434-EGR cells were much less responsive to EED226 than the parental cell line (IC<sub>50</sub> vs IC<sub>50</sub>). This observation together with the unpublished data from our lab showing that GSK126 can still suppress H3K27Me3 globally in COV434-EGR cells (Wang *et al*, unpublished) suggest that COV434 gain resistance towards GSK126 with a different mechanism than lymphoma cell lines with activating mutations. This needs to be further validated using clinical SCCOHT samples that are treated with EZH2 inhibitors. However, *in vitro* establishment of the resistance cells may not be representation of the clinic. *In vivo* selection for drug resistance by chronic treatment can be used to develop tumor with drug resistance. Cells derived from these resistant tumors are better mimicking the clinical outcome as these cells derive from an environment with the presence of biological process such as angiogenesis and hypoxia. Several reports suggest this *in vivo* then *in vitro* selection is more reliable than the *in vitro* selection alone (136-138).

Taken together, our findings suggest that inactivation of SMARCA4 in SCCOHT may rewire their cellular signaling network to be dependent on the histone methyltransferase activity of EZH2 in transcriptional repression for tumorigenesis.

## Chapter 5: Conclusion and Future Directions

### 5.1 Summary of Research

As SCCOHT patients are still being treated with the standard therapy that is tailored for the high grade serous ovarian cancer with very low survival rates, a more targeted therapeutically approach should be developed. One of the challenges impeding researchers from developing potential treatments is the discrepancies between clinical outcomes and preclinical efficacy studies using subcutaneous xenograft models, the most common animal models in testing drug efficacies in cancers including SCCOHT. Therefore, better preclinical mouse models could expedite clinical improvement. Intrabursal models are considered to be a better model for ovarian cancer as they provide primary site as well as appropriate microenvironment for ovarian tumor formation.

In order to develop intrabursal models of SCCOHT with more effective tumor monitoring, I have established three fluorescent SCCOHT cell lines. When they were inoculated into mice, all three cell lines formed subcutaneous tumors and intrabursal tumors. The fluorescence signals of subcutaneous tumors directly correlated with tumor volumes, while those of intrabursal tumors did not represent tumor, suggesting that fluorescence microscope can be used to detect intrabursal tumor development, but the signal strength cannot be used to measure tumor volume faithfully. The histological analysis, on the other hand, further indicated that intrabursal models more closely resembled clinical presentations of SCCOHT than subcutaneous models. Follicle-like structures, typical features of SCCOHT clinical samples, and massive angiogenesis are

observed in all three intrabursal models. Collectively, successful intrabursal xenograft establishment for SCCOHT provides a better model for further studies.

I have also shown targeting PRC2 complex in SWI/SNF-defective SCCOHT might be specific (Chapter 4). The allosteric inhibition of PRC2 through knockdown of EZH2 can effectively suppress the proliferation of SCCOHT cells. Besides, both EZH2 inhibitor, GSK126, and EED inhibitor, EED226 effectively suppresses SCCOHT cell growth *in vitro*. Treatment of 200 mg/kg EED226 BID for two weeks significantly slowed down the tumor progression, measured by both tumor volume and fluorescent signals, in SCCOHT1-mKate2 subcutaneous xenograft model. Thus, targeting PRC2 complex is a promising approach for treating SCCOHT.

## **5.2 Limitation and Future Directions**

In Chapter 3, subcutaneous xenograft model was successfully established. Its fluorescence signals correlate with tumor volume. However, two of the three mice with SCCOHT1-mKate2 intrabursal injection did not have fluorescence signal, but with tumor progression. IHC staining identified BRG1 (SMARCA4) expression in all tumor cells from the two mice without fluorescence signal and roughly half of the tumor from the mice with fluorescence. Possible explanations given in the previous chapter include horizontal gene transfer from mouse cells or contamination of other ovarian cancer cells during culture of SCCOHT1-mKate2 cells. This could be confirmed by further analysis such as investigating the chromosome of tumors to see if it was originated from mouse or human or STR analysis of cultured tumor cells to test the presence of other cell lines.

Single cell sequencing can also be performed on both fluorescent and non-fluorescent population to verify if the tumor population consists of only SCCOHT1 cells.

With the successful establishment of SCCOHT intrabursal model, others can utilize intrabursal models to answer some unsolved questions. For example, most SCCOHT cases are unilateral, usually present in the right ovary, despite the presence of metastasis. With the aid of intrabursal model and bioimaging system, mechanism behind this unilateral presence may be studied. For example, another fluorescent-labelled (eg. YFP or GFP) SCCOHT cells can be injected into the tumor-free ovary of the animal with an existing mKate2-labelled intrabursal tumor. Absence of tumorigenesis from the new labelled cells can further demonstrate the unilateral character of SCCOHT, and studies can be designed to investigate the biology behind this.

In Chapter 4, EED226 was picked from the EED inhibitor category. Other EED inhibitors, such as A395 or MAK683 (modified version of EED226) could also be included in the *in vitro* testing to determine if inhibition of EED is specific to SCCOHT cells only. Oral dosing twice daily at 200 mg/kg is not plausible as animals get stressed and might lead to potential effects towards the study. A better formulation of EED226 should be determined to avoid frequent dosing and can eliminate the side effects or dosing error caused by frequent dosing in preclinical. Besides, the current efficacy study was performed on subcutaneous model. As intrabursal model is a better model to mimic SCCOHT tumor progression than the subcutaneous model, an EED226 efficacy study

in intrabursal model can be conducted, and the outcome might better predict what will happen in clinic.

EED226 has shown selective sensitivity towards SCCOHT cells among the other ovarian cancer cells and other SWI/SNF defective cells, but the underlying mechanism have not been revealed yet. Besides the reliance of the catalytic activity of EZH2 in SWI/SNF-deficient cells, Kim *et al* have shown that the SWI/SNF mutant cancers also depended on the non-catalytic activity of EZH2 (131), which supports PRC2 integrity. Targeting the binding pocket of EED can potentially disrupt the integrity of PRC2 and sensitize the SCCOHT cells to EED226. Future studies are therefore required to determine whether EED226 have impact on integrity of PRC2 complex.

As mentioned in Chapter 4, many patients develop drug resistance easily. Treating patients with only one type of chemotherapy drug is not sufficient. Combinational therapy should also be considered. Our lab has previously reported the synergistic effect of treating SCCOHT with EZH2 inhibitor (EPZ-6438) in combination with HDAC inhibitor (quisinostat) (124). We found SMARCA4 re-expression and HDAC inhibition co-regulate a group of genes that are required for cell fate decision (124). Synergistic effect between EED inhibitors and HDAC inhibitors as well as other inhibitors should also be checked, and as well as the potential mechanism.

Besides, potential mechanism to gain drug resistance can be predicted. We have established GSK126 resistant SCCOHT cells through stepwise exposure to GSK126, and its sensitivity towards EED inhibition decreased, suggesting that the acquired resistance to GSK126 in SCCOHT cells is different from lymphoma cells, which

accumulated mutations in SET domain of EZH2 upon acquiring resistance to GSK126 (83). However, our observation needs to be validated with clinical samples.

To summarize, I have development the fluorescence-labelled xenograft models (subcutaneous and intrabursal) for SCCOHT with intrabursal models closely mimicking the clinical pathological characteristics. Inhibition of PRC2 activity through targeting either catalytic domain of EZH2 or the EED binding pocket can be used as potential therapeutics for SCCOHT.

## Bibliography

1. Canada S. Leading causes of death, total population, by age group: Statistics Canada; 2018 [updated 07/29/2018. Available from: <https://www150.statcan.gc.ca/t1/tbl1/en/tv.action?pid=1310039401>.
2. Sciences NAO. Ovarian Cancers: Evolving Paradigms in Research and Care: National Academies Press (US); 2016.
3. Karnezis AN, Cho KR, Gilks B, Pearce CL, Huntsman DG. The disparate origins of ovarian cancers: pathogenesis and prevention strategies. *Nature Reviews*. 2017;17:65-74.
4. America Co. Ovarian cancer symptoms 2018 [updated 06/28/2018. Available from: <https://www.cancercenter.com/ovarian-cancer/symptoms/>.
5. America Co. Ovarian cancer stages 2017 [updated 03/17/2017. Available from: <https://www.cancercenter.com/ovarian-cancer/symptoms/>.
6. McGuire WP, Hoskins WJ, Brady MF, Kucera PR, Partridge EE, Look KY, et al. Cyclophosphamide and cisplatin versus paclitaxel and cisplatin: a phase III randomized trial in patients with suboptimal stage III/IV ovarian cancer (from the Gynecologic Oncology Group). *Semin Oncol*. 1996;23(5 Suppl 12):40-7.
7. Witjes JA, Comperat E, Cowan NC, De Santis M, Gakis G, Le Bret T, et al. EAU guidelines on muscle-invasive and metastatic bladder cancer: summary of the 2013 guidelines. *Eur Urol*. 2014;65(4):778-92.
8. Wu YL, Zhou C, Liang CK, Wu G, Liu X, Zhong Z, et al. First-line erlotinib versus gemcitabine/cisplatin in patients with advanced EGFR mutation-positive non-small-cell lung cancer: analyses from the phase III, randomized, open-label, ENSURE study. *Ann Oncol*. 2015;26(9):1883-9.
9. Helm CW, States JC. Enhancing the efficacy of cisplatin in ovarian cancer treatment - could arsenic have a role. *J Ovarian Res*. 2009;2:2.
10. Dasari S, Tchounwou PB. Cisplatin in cancer therapy: molecular mechanisms of action. *Eur J Pharmacol*. 2014;740:364-78.
11. Sugiyama T, Kamura T, Kigawa J, Terakawa N, Kikuchi Y, Kita T, et al. Clinical characteristics of clear cell carcinoma of the ovary: a distinct histologic type with poor prognosis and resistance to platinum-based chemotherapy. *Cancer*. 2000;88(11):2584-9.
12. Hess V, A'Hern R, Nasiri N, King DM, Blake PR, Barton DP, et al. Mucinous epithelial ovarian cancer: a separate entity requiring specific treatment. *J Clin Oncol*. 2004;22(6):1040-4.
13. Hamanishi J, Mandai M, Konishi I. Immune checkpoint inhibition in ovarian cancer. *Int Immunol*. 2016;28(7):339-48.

14. Longoria TC, Eskander RN. Immune checkpoint inhibition: therapeutic implications in epithelial ovarian cancer. *Recent Pat Anticancer Drug Discov.* 2015;10(2):133-44.
15. Farmer H, McCabe N, Lord CJ, Tutt AN, Johnson DA, Richardson TB, et al. Targeting the DNA repair defect in BRCA mutant cells as a therapeutic strategy. *Nature.* 2005;434(7035):917-21.
16. Scully RE. *Tumors of the Ovary and Maldeveloped Gonads: Armed Forces Institutes of Pathology;* 1979.
17. Dickersin GR, Kline IW, Scully RE. Small cell carcinoma of the ovary with hypercalcemia: a report of eleven cases. *Cancer.* 1982;49(1):188-97.
18. Estel R, Hackethal A, Kalder M, Munstedt K. Small cell carcinoma of the ovary of the hypercalcaemic type: an analysis of clinical and prognostic aspects of a rare disease on the basis of cases published in the literature. *Arch Gynecol Obstet.* 2011;284(5):1277-82.
19. Florell SR, Bruggers CS, Matlak M, Young RH, Lowichik A. Ovarian small cell carcinoma of the hypercalcemic type in a 14 month old: the youngest reported case. *Med Pediatr Oncol.* 1999;32(4):304-7.
20. Korivi BR, Javadi S, Faria S, Sagebiel T, Garg N, Patnana M, et al. Small Cell Carcinoma of the Ovary, Hypercalcemic Type: Clinical and Imaging Review. *Curr Probl Diagn Radiol.* 2017.
21. Young RH, Oliva E, Scully RE. Small cell carcinoma of the ovary, hypercalcemic type. A clinicopathological analysis of 150 cases. *Am J Surg Pathol.* 1994;18(11):1102-16.
22. Matias-Guiu X, Prat J, Young RH, Capen CC, Rosol TJ, Delellis RA, et al. Human parathyroid hormone-related protein in ovarian small cell carcinoma. An immunohistochemical study. *Cancer.* 1994;73(7):1878-81.
23. Callegaro-Filho D, Gershenson DM, Nick AM, Munsell MF, Ramirez PT, Eifel PJ, et al. Small cell carcinoma of the ovary-hypercalcemic type (SCCOHT): A review of 47 cases. *Gynecol Oncol.* 2016;140(1):53-7.
24. Kascak P, Zamecnik M, Bystricky B. Small Cell Carcinoma of the Ovary (Hypercalcemic Type): Malignant Rhabdoid Tumor. *Case Rep Oncol.* 2016;9(2):305-11.
25. Abeler V, Kjorstad KE, Nesland JM. Small cell carcinoma of the ovary. A report of six cases. *Int J Gynecol Pathol.* 1988;7(4):315-29.
26. Staff H. Significant Information About the Normal Size of Ovaries 2018 [updated 03/12/2018].
27. Kupryjanczyk J, Dansonka-Mieszkowska A, Moes-Sosnowska J, Plisiecka-Halasa J, Szafron L, Podgorska A, et al. Ovarian small cell carcinoma of hypercalcemic type - evidence of germline origin and SMARCA4 gene inactivation. a pilot study. *Pol J Pathol.* 2013;64(4):238-46.

28. Jelinic P, Mueller JJ, Olvera N, Dao F, Scott SN, Shah R, et al. Recurrent SMARCA4 mutations in small cell carcinoma of the ovary. *Nat Genet.* 2014;46(5):424-6.
29. Witkowski L, Carrot-Zhang J, Albrecht S, Fahiminiya S, Hamel N, Tomiak E, et al. Germline and somatic SMARCA4 mutations characterize small cell carcinoma of the ovary, hypercalcemic type. *Nat Genet.* 2014;46(5):438-43.
30. Ramos P, Karnezis AN, Craig DW, Sekulic A, Russell ML, Hendricks WP, et al. Small cell carcinoma of the ovary, hypercalcemic type, displays frequent inactivating germline and somatic mutations in SMARCA4. *Nat Genet.* 2014;46(5):427-9.
31. Ramos P, Karnezis AN, Hendricks WP, Wang Y, Tembe W, Zismann VL, et al. Loss of the tumor suppressor SMARCA4 in small cell carcinoma of the ovary, hypercalcemic type (SCCOHT). *Rare Dis.* 2014;2(1):e967148.
32. Karnezis AN, Wang Y, Ramos P, Hendricks WP, Oliva E, D'Angelo E, et al. Dual loss of the SWI/SNF complex ATPases SMARCA4/BRG1 and SMARCA2/BRM is highly sensitive and specific for small cell carcinoma of the ovary, hypercalcaemic type. *J Pathol.* 2016;238(3):389-400.
33. Kurman RJ, Carcangiu, M.L., Herrington, C.S., Young, R.H. WHO Classification of Tumours of Female Reproductive Organs. 2014;6:307.
34. Riopel MA, Perlman EJ, Seidman JD, Kurman RJ, Sherman ME. Inhibin and epithelial membrane antigen immunohistochemistry assist in the diagnosis of sex cord-stromal tumors and provide clues to the histogenesis of hypercalcemic small cell carcinomas. *Int J Gynecol Pathol.* 1998;17(1):46-53.
35. McCluggage WG, Oliva E, Connolly LE, McBride HA, Young RH. An immunohistochemical analysis of ovarian small cell carcinoma of hypercalcemic type. *Int J Gynecol Pathol.* 2004;23(4):330-6.
36. Forster C, Ostertag H, Schmitt J, Roessner A. Small cell carcinoma of the ovary, hypercalcemic type. A case report with immunohistochemical, ultrastructural and cytophotometric analysis and review of the literature. *Gen Diagn Pathol.* 1997;142(5-6):365-70.
37. Lamovec J, Bracko M, Cerar O. Familial occurrence of small-cell carcinoma of the ovary. *Arch Pathol Lab Med.* 1995;119(6):523-7.
38. Amar AM, Tomlinson G, Green DM, Breslow NE, de Alarcon PA. Clinical presentation of rhabdoid tumors of the kidney. *J Pediatr Hematol Oncol.* 2001;23(2):105-8.
39. Versteeg I, Sevenet N, Lange J, Rousseau-Merck MF, Ambros P, Handgretinger R, et al. Truncating mutations of hSNF5/INI1 in aggressive paediatric cancer. *Nature.* 1998;394(6689):203-6.
40. Biegel JA, Zhou JY, Rorke LB, Stenstrom C, Wainwright LM, Fogelgren B. Germline and acquired mutations of INI1 in atypical teratoid and rhabdoid tumors. *Cancer Res.* 1999;59(1):74-9.

41. Hasselblatt M, Nagel I, Oyen F, Bartelheim K, Russell RB, Schuller U, et al. SMARCA4-mutated atypical teratoid/rhabdoid tumors are associated with inherited germline alterations and poor prognosis. *Acta Neuropathol.* 2014;128(3):453-6.
42. Fahiminiya S, Witkowski L, Nadaf J, Carrot-Zhang J, Goudie C, Hasselblatt M, et al. Molecular analyses reveal close similarities between small cell carcinoma of the ovary, hypercalcemic type and atypical teratoid/rhabdoid tumor. *Oncotarget.* 2016;7(2):1732-40.
43. Foulkes WD, Clarke BA, Hasselblatt M, Majewski J, Albrecht S, McCluggage WG. No small surprise - small cell carcinoma of the ovary, hypercalcaemic type, is a malignant rhabdoid tumour. *J Pathol.* 2014;233(3):209-14.
44. Gamwell LF, Gambaro K, Merzotis M, Crane C, Arcand SL, Bourada V, et al. Small cell ovarian carcinoma: genomic stability and responsiveness to therapeutics. *Orphanet Journal of Rare Diseases.* 2013;8(33).
45. Qin Q, Ajewole VB, Sheu TG, Donohue R, Singh M. Successful treatment of a stage IIIC small-cell carcinoma of the ovary hypercalcemic subtype using multi-modality therapeutic approach. *Ecancermedicalsecience.* 2018;12(832).
46. Senekjian EK, Weiser PA, Talerman A, Herbst AL. Vinblastine, cisplatin, cyclophosphamide, bleomycin, doxorubicin, and etoposide in the treatment of small cell carcinoma of the ovary. *Cancer.* 1989;64:1183-7.
47. Kanwar VS, Heath J, Krasner CN, Pearce JM. Advanced small cell carcinoma of the ovary in a seventeen-year-old female, successfully treated with surgery and multi-agent chemotherapy. *Pediatric Blood & Cancer.* 2008;50:1060-2.
48. Pautier P, Ribrag V, Duvillard P, Rey A, Elghissassi I, Sillet-Bach I, et al. Results of a prospective dose-intensive regimen in 27 patients with small cell carcinoma of the ovary of the hypercalcemic type. *Ann Oncol.* 2007;18(12):1985-9.
49. Hornung R, Fink D, Dobler-Girdziunaite D, Stallmach T, Haller U, Walt H. Photodynamic therapy for the hypercalcemic type of the small cell carcinoma of the ovary in a mouse xenograft model. *Gynecol Oncol.* 1999;75(3):447-52.
50. Yemin Wang PR, Anthony N, Karnezis, Jeffrey M. Trent and David G. Huntsman, editor Abstract 5381: Therapeutic potential of HDAC inhibitors in small cell carcinoma of the ovary, hypercalcemic type (SCCOHT). *AACR 106th Annual Meeting 2015; 2015; Philadelphia, PA.*
51. Stern M, Jensen R, Herskowitz I. Five SWI genes are required for expression of the HO gene in yeast. *J Mol Biol.* 1984;178(4):853-68.
52. Neigeborn L, Carlson M. Genes affecting the regulation of SUC2 gene expression by glucose repression in *Saccharomyces cerevisiae*. *Genetics.* 1984;108(4):845-58.
53. Lu C, Allis CD. SWI/SNF complex in cancer. *Nat Genet.* 2017;49(2):178-9.

54. Kadoch C, Copeland RA, Keilhack H. PRC2 and SWI/SNF Chromatin Remodeling Complexes in Health and Disease. *Biochemistry*. 2016;55(11):1600-14.
55. Wang W, Cote J, Xue Y, Zhou S, Khavari PA, Biggar SR, et al. Purification and biochemical heterogeneity of the mammalian SWI-SNF complex. *EMBO J*. 1996;15(19):5370-82.
56. Wu JI, Lessard J, Crabtree GR. Understanding the words of chromatin regulation. *Cell*. 2009;136(2):200-6.
57. Tang L, Nogales E, Ciferri C. Structure and function of SWI/SNF chromatin remodeling complexes and mechanistic implications for transcription. *Prog Biophys Mol Biol*. 2010;102(2-3):122-8.
58. Wilson BG, Roberts CW. SWI/SNF nucleosome remodellers and cancer. *Nat Rev Cancer*. 2011;11(7):481-92.
59. Chi TH, Wan M, Zhao K, Taniuchi I, Chen L, Littman DR, et al. Reciprocal regulation of CD4/CD8 expression by SWI/SNF-like BAF complexes. *Nature*. 2002;418(6894):195-9.
60. Ho L, Jothi R, Ronan JL, Cui K, Zhao K, Crabtree GR. An embryonic stem cell chromatin remodeling complex, esBAF, is an essential component of the core pluripotency transcriptional network. *Proc Natl Acad Sci U S A*. 2009;106(13):5187-91.
61. Kadoch C, Hargreaves DC, Hodges C, Elias L, Ho L, Ranish J, et al. Proteomic and bioinformatic analysis of mammalian SWI/SNF complexes identifies extensive roles in human malignancy. *Nat Genet*. 2013;45(6):592-601.
62. Shain AH, Pollack JR. The spectrum of SWI/SNF mutations, ubiquitous in human cancers. *PLoS One*. 2013;8(1):e55119.
63. Hoffman GR, Rahal R, Buxton F, Xiang K, McAllister G, Frias E, et al. Functional epigenetics approach identifies BRM/SMARCA2 as a critical synthetic lethal target in BRG1-deficient cancers. *Proc Natl Acad Sci U S A*. 2014;111(8):3128-33.
64. Bitler BG, Aird KM, Garipov A, Li H, Amatangelo M, Kossenkov AV, et al. Synthetic lethality by targeting EZH2 methyltransferase activity in ARID1A-mutated cancers. *Nat Med*. 2015;21(3):231-8.
65. Helming KC, Wang X, Wilson BG, Vazquez F, Haswell JR, Manchester HE, et al. ARID1B is a specific vulnerability in ARID1A-mutant cancers. *Nat Med*. 2014;20(3):251-4.
66. Miller RE, Brough R, Bajrami I, Williamson CT, McDade S, Campbell J, et al. Synthetic Lethal Targeting of ARID1A-Mutant Ovarian Clear Cell Tumors with Dasatinib. *Mol Cancer Ther*. 2016;15(7):1472-84.
67. Cao R, Wang L, Wang H, Xia L, Erdjument-Bromage H, Tempst P, et al. Role of histone H3 lysine 27 methylation in Polycomb-group silencing. *Science*. 2002;298(5595):1039-43.

68. Wang L, Brown JL, Cao R, Zhang Y, Kassis JA, Jones RS. Hierarchical recruitment of polycomb group silencing complexes. *Mol Cell*. 2004;14(5):637-46.
69. Di Croce L, Helin K. Transcriptional regulation by Polycomb group proteins. *Nat Struct Mol Biol*. 2013;20(10):1147-55.
70. Simon JA, Kingston RE. Occupying chromatin: Polycomb mechanisms for getting to genomic targets, stopping transcriptional traffic, and staying put. *Mol Cell*. 2013;49(5):808-24.
71. Cao R, Zhang Y. SUZ12 is required for both the histone methyltransferase activity and the silencing function of the EED-EZH2 complex. *Mol Cell*. 2004;15(1):57-67.
72. Chan-Penebre E, Kuplast KG, Majer CR, Boriack-Sjodin PA, Wigle TJ, Johnston LD, et al. A selective inhibitor of PRMT5 with in vivo and in vitro potency in MCL models. *Nat Chem Biol*. 2015;11(6):432-7.
73. Margueron R, Justin N, Ohno K, Sharpe ML, Son J, Drury WJ, 3rd, et al. Role of the polycomb protein EED in the propagation of repressive histone marks. *Nature*. 2009;461(7265):762-7.
74. Schmitges FW, Prusty AB, Faty M, Stutzer A, Lingaraju GM, Aiwezian J, et al. Histone methylation by PRC2 is inhibited by active chromatin marks. *Mol Cell*. 2011;42(3):330-41.
75. Kim KH, Roberts CW. Targeting EZH2 in cancer. *Nat Med*. 2016;22(2):128-34.
76. Chang CJ, Hung MC. The role of EZH2 in tumour progression. *Br J Cancer*. 2012;106(2):243-7.
77. Chase A, Cross NC. Aberrations of EZH2 in cancer. *Clin Cancer Res*. 2011;17(9):2613-8.
78. Kleer CG, Cao Q, Varambally S, Shen R, Ota I, Tomlins SA, et al. EZH2 is a marker of aggressive breast cancer and promotes neoplastic transformation of breast epithelial cells. *Proc Natl Acad Sci U S A*. 2003;100(20):11606-11.
79. Varambally S, Dhanasekaran SM, Zhou M, Barrette TR, Kumar-Sinha C, Sanda MG, et al. The polycomb group protein EZH2 is involved in progression of prostate cancer. *Nature*. 2002;419(6907):624-9.
80. Medicine USNLo. A Study to Investigate the Safety, Pharmacokinetics, Pharmacodynamics and Clinical Activity of GSK2816126 in Subjects With Relapsed/Refractory Diffuse Large B Cell Lymphoma, Transformed Follicular Lymphoma, Other Non-Hodgkin's Lymphomas, Solid Tumors and Multiple Myeloma: NIH; 2018 [updated 06/04/2018. Available from: <https://clinicaltrials.gov/ct2/show/NCT02082977>.
81. Medicine USNLo. A Phase II, Multicenter Study of the EZH2 Inhibitor Tazemetostat in Adult Subjects With IN11-Negative Tumors or Relapsed/Refractory

Synovial Sarcoma: NIH; 2018 [updated 05/21/2018. Available from:  
<https://clinicaltrials.gov/ct2/show/NCT02601950?term=EPZ6438&rank=8>.

82. He Y, Selvaraju S, Curtin ML, Jakob CG, Zhu H, Comess KM, et al. The EED protein-protein interaction inhibitor A-395 inactivates the PRC2 complex. *Nat Chem Biol*. 2017;13(4):389-95.

83. Qi W, Zhao K, Gu J, Huang Y, Wang Y, Zhang H, et al. An allosteric PRC2 inhibitor targeting the H3K27me3 binding pocket of EED. *Nat Chem Biol*. 2017;13(4):381-8.

84. Medicine USNLo. Safety and Efficacy of MAK683 in Adult Patients With Advanced Malignancies: NIH; 2018 [updated 6/9/2018. Available from:  
<https://clinicaltrials.gov/ct2/show/NCT02900651>.

85. Amatangelo MD, Garipov A, Li H, Conejo-Garcia JR, Speicher DW, Zhang R. Three-dimensional culture sensitizes epithelial ovarian cancer cells to EZH2 methyltransferase inhibition. *Cell Cycle*. 2013;12(13):2113-9.

86. Vaswani RG, Gehling VS, Dakin LA, Cook AS, Nasveschuk CG, Duplessis M, et al. Identification of (R)-N-((4-Methoxy-6-methyl-2-oxo-1,2-dihydropyridin-3-yl)methyl)-2-methyl-1-(1-(1-(2,2,2-trifluoroethyl)piperidin-4-yl)ethyl)-1H-indole-3-carboxamide (CPI-1205), a Potent and Selective Inhibitor of Histone Methyltransferase EZH2, Suitable for Phase I Clinical Trials for B-Cell Lymphomas. *J Med Chem*. 2016;59(21):9928-41.

87. Medicine USNLo. A Study Evaluating CPI-1205 in Patients With B-Cell Lymphomas: NIH; 2018 [updated 03/05/2018. Available from:  
<https://clinicaltrials.gov/ct2/show/NCT02395601?term=EZH2&rank=6>.

88. Wilson BG, Helming KC, Wang X, Kim Y, Vazquez F, Jagani Z, et al. Residual complexes containing SMARCA2 (BRM) underlie the oncogenic drive of SMARCA4 (BRG1) mutation. *Mol Cell Biol*. 2014;34(6):1136-44.

89. Oike T, Ogiwara H, Tominaga Y, Ito K, Ando O, Tsuta K, et al. A synthetic lethality-based strategy to treat cancers harboring a genetic deficiency in the chromatin remodeling factor BRG1. *Cancer Res*. 2013;73(17):5508-18.

90. Sausen M, Leary RJ, Jones S, Wu J, Reynolds CP, Liu X, et al. Integrated genomic analyses identify ARID1A and ARID1B alterations in the childhood cancer neuroblastoma. *Nat Genet*. 2013;45(1):12-7.

91. Stanton BZ, Hodges C, Calarco JP, Braun SMG, Ku WL, Kadoch C, et al. SMARCA4 ATPase mutations disrupt direct eviction of PRC1 from chromatin. *Nature Genetics*. 2017;49(2):282-8.

92. Wilson BG, Wang X, Shen X, McKenna ES, Lemieux ME, Cho YJ, et al. Epigenetic antagonism between polycomb and SWI/SNF complexes during oncogenic transformation. *Cancer Cell*. 2010;18(4):316-28.

93. Lengyel E, Burdette JE, Kenny HA, Matei D, Pilrose J, Haluska P, et al. Epithelial ovarian cancer experimental models. *Oncogene*. 2014;33(28):3619-33.

94. Willis-Owen SA, Flint J. The genetic basis of emotional behaviour in mice. *Eur J Hum Genet.* 2006;14(6):721-8.
95. Laboratory TJ. CHOOSING AN IMMUNODEFICIENT MOUSE MODEL: The Jackson Laboratory; 2018 [Available from: <https://www.jax.org/news-and-insights/2006/march/choosing-an-immunodeficient-mouse-model#>].
96. Friedlander ML, Russell P, Taylor IW, Tattersall MH. Ovarian tumour xenografts in the study of the biology of human epithelial ovarian cancer. *Br J Cancer.* 1985;51(3):319-33.
97. Day CP, Merlino G, Van Dyke T. Preclinical mouse cancer models: a maze of opportunities and challenges. *Cell.* 2015;163(1):39-53.
98. Fu X, Hoffman RM. Human ovarian carcinoma metastatic models constructed in nude mice by orthotopic transplantation of histologically-intact patient specimens. *Anticancer Res.* 1993;13(2):283-6.
99. Kiguchi K, Kubota T, Aoki D, Udagawa Y, Yamanouchi S, Saga M, et al. A patient-like orthotopic implantation nude mouse model of highly metastatic human ovarian cancer. *Clin Exp Metastasis.* 1998;16(8):751-6.
100. Shaw TJ, Senterman MK, Dawson K, Crane CA, Vanderhyden BC. Characterization of intraperitoneal, orthotopic, and metastatic xenograft models of human ovarian cancer. *Mol Ther.* 2004;10(6):1032-42.
101. Puaux AL, Ong LC, Jin Y, Teh I, Hong M, Chow PK, et al. A comparison of imaging techniques to monitor tumor growth and cancer progression in living animals. *Int J Mol Imaging.* 2011;2011:321538.
102. Hasegawa S, Yang M, Chishima T, Miyagi Y, Shimada H, Moossa AR, et al. In vivo tumor delivery of the green fluorescent protein gene to report future occurrence of metastasis. *Cancer Gene Ther.* 2000;7(10):1336-40.
103. Choy G, O'Connor S, Diehn FE, Costouros N, Alexander HR, Choyke P, et al. Comparison of noninvasive fluorescent and bioluminescent small animal optical imaging. *Biotechniques.* 2003;35(5):1022-6, 8-30.
104. Chaudhuri TR, Mountz JM, Rogers BE, Partridge EE, Zinn KR. Light-based imaging of green fluorescent protein-positive ovarian cancer xenografts during therapy. *Gynecol Oncol.* 2001;82(3):581-9.
105. Tempany CM, Zou KH, Silverman SG, Brown DL, Kurtz AB, McNeil BJ. Staging of advanced ovarian cancer: comparison of imaging modalities--report from the Radiological Diagnostic Oncology Group. *Radiology.* 2000;215(3):761-7.
106. Hildebrandt IJ, Su H, Weber WA. Anesthesia and other considerations for in vivo imaging of small animals. *ILAR J.* 2008;49(1):17-26.
107. Chalfie M, Tu Y, Euskirchen G, Ward WW, Prasher DC. Green fluorescent protein as a marker for gene expression. *Science.* 1994;263(5148):802-5.

108. Chudakov DM, Lukyanov S, Lukyanov KA. Fluorescent proteins as a toolkit for in vivo imaging. *Trends Biotechnol.* 2005;23(12):605-13.
109. Shaner NC, Campbell RE, Steinbach PA, Giepmans BN, Palmer AE, Tsien RY. Improved monomeric red, orange and yellow fluorescent proteins derived from *Discosoma* sp. red fluorescent protein. *Nat Biotechnol.* 2004;22(12):1567-72.
110. Heppert JK, Dickinson DJ, Pani AM, Higgins CD, Steward A, Ahringer J, et al. Comparative assessment of fluorescent proteins for in vivo imaging in an animal model system. *Mol Biol Cell.* 2016;27(22):3385-94.
111. Shcherbo D, Murphy CS, Ermakova GV, Solovieva EA, Chepurnykh TV, Shcheglov AS, et al. Far-red fluorescent tags for protein imaging in living tissues. *Biochem J.* 2009;418(3):567-74.
112. Upchurch KS, Parker LM, Scully RE, Krane SM. Differential cyclic AMP responses to calcitonin among human ovarian carcinoma cell lines: A calcitonin-responsive line derived from a rare tumor type. *Journal of Bone and Mineral Research.* 1986;1(3):299-304.
113. Otte A, Göhring G, Steinemann D, Schlegelberger B, Groos S, Länger F, et al. A tumor-derived population (SCCOHT-1) as cellular model for a small cell ovarian carcinoma of the hypercalcemic type. *International Journal of Oncology.* 2012;41(2):765-75.
114. Zhang H, Vollmer M, Geyter MD, Litzistorf Y, Ladewig A, Dürrenberger M, et al. Characterization of an immortalized human granulosa cell line (COV434). *Molecular Human Reproduction.* 2000;6(2):146-53.
115. Suzuki S, Terauchi M, Umezumi T, Kajiyama H, Shibata K, Nawa A, et al. Identification and characterization of cancer stem cells in ovarian yolk sac tumors. *Cancer Science.* 2010;101(10):2179-85.
116. Feoktistova M, Geserick P, Leverkus M. Crystal Violet Assay for Determining Viability of Cultured Cells. *Cold Spring Harbor protocols* 2016;4:343-6.
117. Hoffman RM. Orthotopic metastatic mouse models for anticancer drug discovery and evaluation: a bridge to the clinic. *Invest New Drugs.* 1999;17(4):343-59.
118. Murata T, Mekada E, Hoffman RM. Reconstitution of a metastatic-resistant tumor microenvironment with cancer-associated fibroblasts enables metastasis. *Cell Cycle.* 2017;16(6):533-5.
119. Du Q, Jiang L, Wang XQ, Pan W, She FF, Chen YL. Establishment of and comparison between orthotopic xenograft and subcutaneous xenograft models of gallbladder carcinoma. *Asian Pacific journal of cancer prevention : APJCP.* 2014;15(8):3747-52.
120. Metastatic prostate cancer. *Prostate Cancer: Diagnosis and Treatment* 2014.
121. Talmadge JE, Singh RK, Fidler IJ, Raz A. Murine models to evaluate novel and conventional therapeutic strategies for cancer. *Am J Pathol.* 2007;170(3):793-804.

122. Shemiakina, II, Ermakova GV, Cranfill PJ, Baird MA, Evans RA, Souslova EA, et al. A monomeric red fluorescent protein with low cytotoxicity. *Nat Commun.* 2012;3:1204.
123. Wang Y, Chen SY, Karnezis AN, Colborne S, Santos ND, Lang JD, et al. The histone methyltransferase EZH2 is a therapeutic target in small cell carcinoma of the ovary, hypercalcaemic type. *J Pathol.* 2017;242(3):371-83.
124. Wang Y, Chen SY, Colborne S, Lambert G, Shin CY, Santos ND, et al. Histone deacetylase inhibitors synergizes with catalytic inhibitors of EZH2 to exhibit anti-tumor activity in small cell carcinoma of the ovary, hypercalcemic type. 2018.
125. Otte A, Rauprich F, von der Ohe J, Yang Y, Kommos F, Feuerhake F, et al. c-Met inhibitors attenuate tumor growth of small cell hypercalcemic ovarian carcinoma (SCCOHT) populations. *Oncotarget.* 2015;6(31):31640-58.
126. Goldenberg D, Pavia R. In vivo horizontal oncogenesis by a human tumor in nude mice  
. *Proceedings of the National Academy of Sciences.* 1982;79:2389-92.
127. Goldenberg DM, Rooney RJ, Loo M, Liu D, Chang C-H. In-Vivo Fusion of Human Cancer and Hamster Stromal Cells Permanently Transduces and Transcribes Human DNA. *PLoS One.* 2014;9(9):1-11.
128. Witkowski L, Donini N, Byler-Dann R, Knost JA, Albrecht S, Berchuck A, et al. The hereditary nature of small cell carcinoma of the ovary, hypercalcemic type: two new familial cases. *Fam Cancer.* 2017;16(3):395-9.
129. Witkowski L, Goudie C, Ramos P, Boshari T, Brunet JS, Karnezis AN, et al. The influence of clinical and genetic factors on patient outcome in small cell carcinoma of the ovary, hypercalcemic type. *Gynecol Oncol.* 2016;141(3):454-60.
130. Grau DJ, Chapman BA, Garlick JD, Borowsky M, Francis NJ, Kingston RE. Compaction of chromatin by diverse Polycomb group proteins requires localized regions of high charge. *Genes Dev.* 2011;25(20):2210-21.
131. Kim KH, Kim W, Howard TP, Vazquez F, Tsherniak A, Wu JN, et al. SWI/SNF-mutant cancers depend on catalytic and non-catalytic activity of EZH2. *Nat Med.* 2015;21(12):1491-6.
132. Hanahan D, Weinberg RA. Hallmarks of Cancer: The Next Generation. *Cell.* 2011;144:646-74.
133. Knutson SK, Warholic NM, Wigle TJ, Klaus CR, Allain CJ, Raimondi A, et al. Durable tumour regression in genetically altered malignant rhabdoid tumours by inhibition of methyltransferase EZH2. *Proceedings of National Academy of Science.* 2013;110(19):7922-7.
134. Baker T, Nerle S, Pritchard J, Zhao B, Rivera VM, Garner A, et al. Acquisition of a single EZH2 D1 domain mutation confers acquired resistance to EZH2-targeted inhibitors. *Oncotarget.* 2015;6(32):32646-55.

135. Gibaja V, Shen F, Harari J, Korn J, Ruddy D, Saenz-Vash V, et al. Development of secondary mutations in wild-type and mutant EZH2 alleles cooperates to confer resistance to EZH2 inhibitors. *Oncogene*. 2016;35(5):558-66.
136. Arunasree KM, Roy KR, Anilkumar K, Aparna A, Reddy GV, Reddanna P. Imatinib-resistant K562 cells are more sensitive to celecoxib, a selective COX-2 inhibitor: role of COX-2 and MDR-1. *Leuk Res*. 2008;32(6):855-64.
137. Marfe G, Di Stefano C, Gambacurta A, Ottone T, Martini V, Abruzzese E, et al. Sphingosine kinase 1 overexpression is regulated by signaling through PI3K, AKT2, and mTOR in imatinib-resistant chronic myeloid leukemia cells. *Exp Hematol*. 2011;39(6):653-65 e6.
138. Liu L, Wang S, Chen R, Wu Y, Zhang B, Huang S, et al. Myc induced miR-144/451 contributes to the acquired imatinib resistance in chronic myelogenous leukemia cell K562. *Biochem Biophys Res Commun*. 2012;425(2):368-73.